

Considerations for an Integrated Detector Design at FCC-ee: A Human-AI Exploration

Charles Young

SLAC National Accelerator Laboratory

June 9, 2026

Abstract

This report explores detector design considerations for the Future Circular Collider in its electron-positron mode (FCC-ee) through an extended dialogue between a physicist and an AI assistant. Starting from initial “prejudice” detector concepts proposed by the AI assistant without explicit physicist input, each subsystem is examined in detail, with the AI’s assumptions challenged and revised through the exchange. The discussion covers the full detector from beam pipe to luminosity monitor, with particular attention to the interplay between subsystem choices and the practical considerations — calibration, stability, and operational simplicity — that are essential for a fifteen-year precision physics program. The narrative documents how the integrated detector design evolved substantially from the starting point to revised “prejudice” detector concepts of the AI assistant. The focus of this report is on the process to illustrate both the potential and the limitations of human-AI collaboration in experimental physics design, and the physics capabilities of any of the “prejudice” detector concepts remain to be explored.

Contents

1	Introduction	4
1.1	The FCC-ee Program	4
1.2	Physics Goals and Detector Requirements	5
1.3	Existing Detector Concepts	6
1.4	Approach: Human-AI Collaborative Design Exploration	7
2	Initial Detector Concepts	9
2.1	Criteria for an Integrated Detector	9
2.1.1	Physics Performance Across All Energy Points	9
2.1.2	Systematic Robustness and Long-Term Stability	10
2.1.3	Particle Flow vs. Intrinsic Calorimetric Resolution	10
2.1.4	Hermeticity and Acceptance	10
2.1.5	Technical Maturity and Risk	10
2.1.6	Cost and Schedule	11
2.2	The Case for Two Complementary Detectors	11
2.3	CL1a: The Initial Primary Detector	11
2.3.1	Vertex Detector	12
2.3.2	Inner Silicon Tracker	12
2.3.3	Main Tracker: Drift Chamber	13
2.3.4	Outer Silicon Wrapper	13
2.3.5	Electromagnetic Calorimeter: Noble Liquid	13
2.3.6	Hadronic Calorimeter: Scintillator-Steel Tiles	14
2.3.7	Solenoid	14
2.3.8	Muon System	14
2.3.9	Luminosity Monitor	14
2.4	CL1b: The Initial Complementary Detector	15
3	Subsystem Examination and Evolution	17
3.1	Beam Pipe and Vertex Region	17
3.1.1	Beam Pipe: Material Budget Dominance	17
3.1.2	The Idea of a Sensor Inside the Beam Pipe	18
3.1.3	Unified Vertex and Inner Silicon Tracker	19
3.2	Main Tracker	21
3.2.1	Drift Chamber: Mechanical Design	21
3.2.2	Drift Chamber: Cluster Counting	24

3.2.3	Conventional End Plate Drift Chamber	28
3.2.4	Straw Tube Alternative	30
3.2.5	Time Projection Chamber	31
3.2.6	Drift Chamber vs. TPC: Comparative Assessment	33
3.3	Outer Silicon Wrapper	35
3.3.1	Three Functions in Priority Order	35
3.3.2	LGAD Technology Options	36
3.3.3	Material Budget	38
3.3.4	Start Time for Time-of-Flight	38
3.3.5	Summary of Changes from CL1a	40
3.4	Electromagnetic Calorimeter	40
3.4.1	The Cryostat Problem	41
3.4.2	Crystal Calorimetry Reconsidered	43
3.4.3	SiPM Readout and Dynamic Range	47
3.4.4	Crystal ECAL and Particle Flow Compatibility	50
3.4.5	Summary of ECAL Evolution	52
3.5	Solenoid	53
3.5.1	Field Strength and Accelerator Coupling	53
3.5.2	Solenoid Placement: Inside the HCAL	55
3.5.3	Field Uniformity	57
3.5.4	Summary of Solenoid Evolution	57
3.6	Hadron Calorimeter	58
3.6.1	The Problem and the Particle Flow Solution	58
3.6.2	Scintillator-Steel Tile Calorimeter	59
3.6.3	Dual-Readout Fiber Calorimeter	60
3.6.4	Combining High Granularity and Dual Readout	61
3.6.5	Quantitative Impact on Jet Energy Resolution	63
3.6.6	The HCAL as Flux Return	64
3.6.7	Technology Assessment	64
3.6.8	Summary of HCAL Discussion	65
3.7	Muon System	66
3.7.1	Requirements at FCC-ee	66
3.7.2	Technology Choice: Scintillator Bars	68
3.7.3	Integration with Return Yoke	70
3.7.4	Summary of Muon System Evolution	70
3.8	Luminosity Monitor	71
3.8.1	The Measurement Method	71
3.8.2	Position and Stability Requirements	72
3.8.3	Thermal and Mechanical Stability	73
3.8.4	Monitoring the Acceptance	74
3.8.5	Operational Strategy for Relative Luminosity	75
3.8.6	Detector Design	76
3.8.7	Integration with the Machine-Detector Interface	76
3.8.8	Summary of Luminosity Monitor Discussion	77

4	The Revised Integrated Detector	78
4.1	CL2a: Detector Layout	78
4.1.1	Longitudinal Layout	81
4.2	CL2a: Technology Summary	81
4.3	CL2a: Performance Targets	83
4.4	Interplay Between Subsystem Choices	83
4.5	CL2b: The Revised Complementary Detector	84
4.6	Summary of Changes from Initial to Revised Concepts	86
4.7	Unresolved Questions and R&D Priorities	86
5	Reflections on Human-AI Collaboration	89
5.1	What the AI Brought to the Discussion	89
5.1.1	Rapid Survey of Technology Options	89
5.1.2	Quantitative Estimates on Demand	89
5.1.3	Systematic Comparison Frameworks	90
5.1.4	Willingness to Revise Positions	90
5.1.5	Documentation and Synthesis	90
5.2	What Required Human Guidance	91
5.2.1	Practical Experience and Engineering Judgment	91
5.2.2	Asking the Right Question	91
5.2.3	Recognizing Inappropriate Technology Choices	92
5.2.4	System-Level Thinking	92
5.3	Observations on AI Reasoning Patterns	92
5.3.1	Knowledge Without Connections	93
5.3.2	Exploration Bounded by the Questioner	93
5.3.3	Tendency Toward Deference	93
5.3.4	Recency and Visibility Bias	94
5.4	Limitations of the Approach	94
5.4.1	Knowledge Cutoff	94
5.4.2	Approximate Quantitative Estimates	94
5.4.3	Technology Enthusiasm Bias	95
5.4.4	Limited Access to Unpublished Knowledge	95
5.4.5	No Independent Validation	95
5.5	Assessment	95
6	Summary	97
	Declaration of Generative AI in the Research Process	100

Chapter 1

Introduction

1.1 The FCC-ee Program

The Future Circular Collider in its electron-positron mode (FCC-ee)¹⁻³ is a proposed circular e^+e^- collider to be housed in a new ~ 91 km tunnel in the Geneva region at CERN. It is designed to operate at four principal center-of-mass energy points, each targeting a distinct set of precision measurements:

Table 1.1: The four principal operating energy points of FCC-ee and their primary physics goals. Approximate integrated luminosities and event yields correspond to the baseline run plan as described in the FCC-ee Conceptual Design Report¹.

\sqrt{s} (GeV)	Program	Key measurements	Approximate yield
91	Z pole	Electroweak precision, flavor physics, R_b , α_s , N_ν	10^{12} Z bosons
160	WW threshold	m_W from threshold scan, W branching ratios	10^8 W pairs
240	ZH production	Higgs couplings, σ_{ZH} , Higgs recoil mass	10^6 ZH events
350	$t\bar{t}$ threshold	Top mass, EW couplings, top Yukawa	10^6 $t\bar{t}$

The breadth of this program is both its greatest strength and its most significant challenge for detector design. At the Z pole, the experiment is overwhelmingly statistics-rich — with 10^{12} Z bosons, many measurements of electroweak observables and flavor physics processes will be limited by systematic uncertainties rather than statistics, placing extraordinary demands on detector stability, calibration, and acceptance control. At the ZH threshold, the Higgs recoil mass measurement requires excellent tracking momentum resolution. At the $t\bar{t}$ threshold, the reconstruction of six-jet final states demands good jet energy resolution at

the highest particle energies accessible at FCC-ee. Energy scans to determine masses and line widths require unprecedented precision in *relative* luminosity measurements. No single measurement drives the detector design; rather, the detector must deliver competitive performance across this full spectrum.

FCC-ee benefits from a comparatively benign radiation environment relative to hadron colliders. This has profound implications for detector technology choices: it liberates the designer from the radiation hardness requirements that dominate technology selection at the LHC, and opens the door to technologies that prioritize *precision over survivability*. As will be seen throughout this report, this observation recurs in nearly every subsystem discussion.

1.2 Physics Goals and Detector Requirements

The mapping from physics measurements to detector requirements is not one-to-one. Different energy points stress different aspects of the detector, and in some cases the requirements are in tension. Table 1.2 summarizes the principal connections.

Table 1.2: Key physics measurements at each energy point and the detector capabilities they primarily require.

Energy point	Key measurement	Driving detector requirement
Z pole	EW precision ($m_W, \sin^2 \theta_W$)	Absolute luminosity (10^{-4}) Relative luminosity (10^{-5}) acceptance control
	R_b, R_c	b/c tagging, vertexing
	Flavor physics	Vertex resolution, PID
	α_s	Jet energy resolution
WW threshold	m_W from threshold scan	Tracking momentum resolution, lepton identification
ZH	Higgs recoil mass	momentum resolution $\sigma(p_T)/p_T$ for $Z \rightarrow \mu\mu$
	Higgs couplings ($H \rightarrow b\bar{b}, c\bar{c}, \gamma\gamma$)	Jet energy resolution, b/c tagging, photon resolution
$t\bar{t}$	Top mass, couplings	Jet energy resolution at highest energies, b -tagging, forward coverage

Several cross-cutting themes emerge from this mapping:

- **Vertexing and heavy-flavor tagging** are essential across all energy points, from R_b at the Z pole to Higgs coupling measurements at 240 GeV and top physics at 350 GeV.

This places a premium on minimizing the material budget of the vertex detector and beam pipe.

- **Tracking momentum resolution** is critical for the Higgs recoil measurement ($Z \rightarrow \mu^+ \mu^-$ recoil mass), which requires $\sigma(p_T)/p_T^2 \lesssim 2 \times 10^{-5} \text{ GeV}^{-1}$. This demands a large tracking volume, strong magnetic field, many precise measurement points, and low material budget so measurement performance is not compromised by multiple scattering.
- **Jet energy resolution** matters at every energy point but becomes most demanding at the $t\bar{t}$ threshold where jet energies reach 100–175 GeV and the particle flow approach becomes susceptible to shower overlap.
- **Systematic control and long-term stability** dominate at the Z pole. With 10^{12} Z bosons, statistical uncertainties on most observables are negligible; the experiment is limited by how well systematics — calibration, acceptance, luminosity — are controlled. Technologies that offer intrinsic uniformity and stability deserve particular attention.
- **Particle identification** ($\pi/K/p$ separation) enhances the flavor physics program at the Z pole and improves jet flavor tagging at all energies. This capability is not always given high priority in detector concept studies but can significantly extend the physics reach.
- **Luminosity measurement** at the 10^{-4} level (absolute) and 10^{-5} level (relative) is essential for the Z lineshape scan and threshold measurements. This is a metrology challenge as much as a detector challenge.

1.3 Existing Detector Concepts

Several detector concepts have been put forward for FCC-ee. Four ¹ have been formally submitted as Expressions of Interest ⁴:

IDEA (Innovative Detector for an Electron-positron Accelerator) ⁵ features a large low-mass drift chamber as its central tracker, providing both momentum measurement and particle identification through cluster counting (dN/dx), complemented by silicon vertex detector and outer tracking layer. It proposes a dual-readout fiber calorimeter for combined electromagnetic and hadronic energy measurement, exploiting the ratio of scintillation to Čerenkov light to correct for event-by-event fluctuations in the electromagnetic fraction of hadronic showers. A thin, low-mass superconducting solenoid and a preshower detector complement the calorimeter system.

CLD (CLic Detector adapted for FCC-ee) ⁶ is based on detector concepts developed for the Compact Linear Collider (CLIC) and adapted to FCC-ee conditions. It features an all-silicon tracker, a silicon-tungsten electromagnetic calorimeter with high transverse and longitudinal granularity optimized for particle flow, and a scintillator-steel hadronic calorimeter with similar granularity. The overall design philosophy is driven by the particle flow paradigm, in which individual particles in jets are reconstructed using the combination of tracking and highly segmented calorimetry.

¹This report is based on the AI's understanding of them at the time of the investigation and does not necessarily represent their current status.

ALLEGRO (A Lepton coLlidEr detector with Granular Read-Out)⁷ explores a noble liquid electromagnetic calorimeter (liquid argon or liquid krypton with lead or tungsten absorbers), combined with fine-granularity readout electrodes for particle flow capability. It shares many elements with CLD for the tracking and hadronic calorimeter systems, with the electromagnetic calorimeter being the primary distinguishing feature.

ILD-FCCee⁸ is an adaptation of the International Large Detector (ILD) concept originally developed for the International Linear Collider (ILC)⁹. Its distinguishing feature is the use of a Time Projection Chamber (TPC) as the main tracker, providing three-dimensional space points with many measurements per track and only gaseous material in the tracking volume. The TPC is complemented by silicon inner and outer tracking layers. The calorimeter system follows the particle flow approach with a silicon-tungsten electromagnetic calorimeter and a scintillator-steel hadronic calorimeter.

These four concepts share many common elements — notably MAPS-based vertex detectors and a superconducting solenoid — while differing in their choices for the central tracker, electromagnetic calorimeter, and hadronic calorimeter. They are explicitly designated as “concepts” rather than final designs, and it is expected that the eventual FCC-ee detector(s) will draw elements from multiple concepts.

It is worth noting that similar detector studies are underway for the Circular Electron-Positron Collider (CEPC)^{10;11} proposed in China. CEPC and FCC-ee share remarkably similar accelerator designs, performance parameters, and physics goals — both are circular e^+e^- colliders designed to operate as Z, W, Higgs, and top factories at comparable luminosities. The CEPC reference detector concept features a TPC main tracker, a silicon-tungsten electromagnetic calorimeter based on the particle flow approach, and a scintillator-steel hadronic calorimeter, with extensive studies of TPC performance, ion back-flow management, and particle flow optimization at Higgs factory conditions¹². Given the close correspondence between the two machines, the CEPC detector studies are directly relevant to FCC-ee and vice versa. The CEPC reference detector can be considered, in all but name, a fifth concept for an e^+e^- Higgs factory detector.

This report takes the approach of examining each subsystem independently rather than adopting any single concept, constructing an integrated design based on the merits of the available technology options. Where relevant, the strengths and limitations of choices made by the existing concepts are discussed.

1.4 Approach: Human-AI Collaborative Design Exploration

This report documents an extended exploration of FCC-ee detector design conducted through a dialogue between a physicist with experience in collider detector design and an AI assistant (Claude, developed by Anthropic). The methodology was as follows:

- i) The AI was asked to propose initial detector concepts for FCC-ee, including a rationale for each subsystem choice and criteria for the integrated design.
- ii) Each subsystem was then examined in detail through iterative dialogue. The physicist posed questions, challenged assumptions, and introduced practical considerations based

on experience. The AI responded with analysis, revised its positions where the arguments warranted, and maintained its positions where it judged the original reasoning sound.

- iii) Through this process, the integrated detector concept evolved substantially from its starting point, with changes in several major subsystem choices.

The intent is twofold. First, the resulting detector concepts and the technical analysis underlying them are of interest in their own right, contributing to the ongoing discussion within the FCC-ee detector community. However, the level of study and scrutiny is so far minimal, and these concepts should not be compared at face value with the existing FCC-ee detector concepts. Second, the process itself — the strengths and limitations of human-AI collaboration for complex physics detector design — is worth documenting as the field begins to explore such tools.

The report is structured to reflect this process. Chapter 2 presents the initial detector concepts as proposed by the AI, including the criteria and reasoning behind each choice. Chapter 3 walks through the subsystem-by-subsystem examination, documenting how and why the design evolved. Chapter 4 presents the final integrated detector concept as proposed by the AI. Chapter 5 reflects on the collaborative process itself, and Chapter 6 summarizes the conclusions.

It should be noted that the quantitative estimates throughout this report are intended to be illustrative rather than definitive. They are based on analytical calculations, scaling arguments, and published performance data, not on dedicated Monte Carlo simulations of the specific detector geometry proposed here. A number of the conclusions reached in this study would benefit from validation through full simulation, and these are identified as R&D priorities where appropriate.

The AI assistant used in this study was Claude, developed by Anthropic, accessed through the Anthropic web interface (model identifier `claude-opus-4`). A large part of the dialogue was conducted in a single extended conversation, allowing the AI to maintain context across all subsystem discussions. The dialogue took place in April 2026.

The interaction was conducted in a direct dialogue (chatbot) mode in which the AI operated solely from its training data and from information explicitly provided by the physicist in the text of the conversation or through file uploads. Notably, when the physicist provided URLs to external resources, the AI could not access or read those resources — only information directly pasted or uploaded into the conversation was available. The AI did not have access to web search, database queries, or any external information retrieval during the dialogue. This is a significant limitation: for a rapidly evolving field, the AI’s training data inevitably misses recent developments, and the burden of supplying current information falls entirely on the human contributor. More capable configurations exist in which the AI can retrieve and read documents from the web in real time; such tool-augmented modes would likely improve the efficiency and completeness of a study of this kind.

Chapter 2

Initial Detector Concepts

This chapter presents the initial detector concepts as proposed by the AI at the outset of the study, before the detailed subsystem examination described in Chapter 3. The criteria, reasoning, and specific technology choices reflect the AI's starting positions, with no guidance from the physicist. Several of these positions were subsequently revised through the collaborative discussion, leading to the updated concepts presented in Chapter 4.

Naming convention. The detector concepts developed in this report are labeled as follows:

- **CL1a** — the initial primary detector concept (this chapter);
- **CL1b** — the initial complementary detector concept (this chapter);
- **CL2a** — the revised primary detector concept, after the subsystem examination of Chapter 3 (presented in Chapter 4);
- **CL2b** — the revised complementary detector concept (presented in Chapter 4).

2.1 Criteria for an Integrated Detector

Before specifying technology choices, it is useful to articulate the criteria that should guide the overall detector design. The following were identified as the principal considerations, roughly in order of priority.

2.1.1 Physics Performance Across All Energy Points

The FCC-ee program spans a factor of nearly four in center-of-mass energy, from 91 to 350 GeV, as well as significant differences in event rate. The detector cannot be optimized for a single energy point. As discussed in Section 1.2, the Z pole program demands vertexing, particle identification, high beam crossing rate, and systematic control; the ZH program demands tracking momentum resolution and jet energy resolution; and the $t\bar{t}$ program demands jet resolution at the highest energies. A detector optimized purely for the Higgs recoil measurement at 240 GeV might not be optimal for the Z pole flavor physics program, and vice versa. The integrated design must make thoughtful compromises.

2.1.2 Systematic Robustness and Long-Term Stability

For a facility expected to operate for fifteen or more years and to produce measurements at the permille level or below, systematic control is paramount. This criterion favors technologies that offer:

- **Intrinsic uniformity** — detector response that is uniform by construction, rather than requiring extensive calibration to achieve uniformity.
- **Stability over time** — technologies that do not degrade, or degrade predictably, over years of operation.
- **Redundancy** — the ability to cross-check critical measurements using independent subsystems or methods.
- **Insensitivity to environmental conditions** — minimal dependence on temperature, pressure, humidity, and other external parameters.

2.1.3 Particle Flow vs. Intrinsic Calorimetric Resolution

Two fundamentally different philosophies exist for measuring jet energies at e^+e^- colliders:

Particle flow reconstructs every particle in the event individually. Charged particles ($\sim 65\%$ of jet energy) are measured by the tracker with excellent resolution ($\sigma/E \sim 10^{-4}$ – 10^{-3}). Photons ($\sim 25\%$ of jet energy) are measured by the electromagnetic calorimeter. Only neutral hadrons ($\sim 10\%$ of jet energy) rely on the hadronic calorimeter. This approach requires high-granularity calorimetry for pattern recognition and a strong magnetic field to separate charged and neutral particles.

Calorimetric approaches, such as dual-readout, measure jet energy primarily from the calorimeter with event-by-event corrections for the different response of the calorimeter to the varying electromagnetic fraction of hadronic showers. This is less dependent on tracking perfection and can provide robust jet energy measurement even when particle flow breaks down.

The optimal strategy may involve elements of both approaches, and the choice of electromagnetic calorimeter technology has significant implications for which approach is more effective.

2.1.4 Hermeticity and Acceptance

Missing energy signatures (e.g., $H \rightarrow \text{invisible}$, $Z \rightarrow \nu\bar{\nu}$) require near- 4π coverage with minimal cracks and dead material. The transition region between barrel and endcap deserves particular attention, as does the forward region where beam pipe and machine-detector interface elements create unavoidable gaps.

2.1.5 Technical Maturity and Risk

Some technologies are well-proven at collider scale while others remain at the prototype stage. A prudent design balances ambition with risk. The FCC-ee timeline, with first collisions

anticipated in the mid-2040s, provides a finite window for R&D, and technologies requiring extensive development may not be viable.

2.1.6 Cost and Schedule

Detector cost for a flagship facility is typically in the 1000M CHF range. Technology choices have significant cost implications. Calorimeters are often the most expensive subsystem due to material cost and cryogenic infrastructure in the case of noble liquid calorimetry. Magnets are also expensive and their costs are driven by field strength and volume.

2.2 The Case for Two Complementary Detectors

The current FCC-ee plan foresees four interaction points and detectors. This presents a strategic opportunity that goes beyond simple redundancy.

If the two detectors are designed with *maximally different* technology choices, they provide:

- i) **Independent systematic checks.** Every major physics measurement is performed twice, with different detector technologies and different systematic uncertainties. Agreement between the two results provides powerful validation; disagreement reveals problems that might otherwise go undetected.
- ii) **Complementary performance.** Different technologies excel in different regimes. A particle-flow-optimized detector may outperform at lower jet energies, while a dual-readout calorimeter may be superior at higher energies. Together, the two detectors offer excellent coverage over the full performance space.
- iii) **Risk mitigation.** If a novel technology encounters unforeseen limitations in operation, the other detector with its different technology provides a fallback for the physics program.
- iv) **Healthy competition.** The history of collider physics shows that having two experiments analyzing the same data leads to more careful work and better results from both.

The decisions for the two detectors should therefore be made jointly, with the goal of maximizing complementarity rather than duplicating the same design. In what follows, the AI proposed two initial detector concepts — CL1a and CL1b — designed with this principle in mind.

2.3 CL1a: The Initial Primary Detector

Concept CL1a was constructed by selecting, for each subsystem, the technology judged by the AI assistant to offer the best overall performance across the full FCC-ee program, with emphasis on systematic robustness and long-term stability. The initial choices and their rationale are summarized below and in Table 2.1.

Table 2.1: CL1a: initial primary detector concept as proposed at the start of the study. Entries marked with † were subsequently revised through the collaborative discussion (Chapter 3), leading to the updated concept CL2a (Chapter 4).

Subsystem	Technology	Key feature
Beam pipe	Beryllium, locally thinned	Minimal material
Vertex detector	MAPS, 65 nm CMOS, curved shells	$\sim 0.02\%$ X_0 /layer
Inner silicon†	Additional MAPS layers	Bridge to main tracker
Main tracker	Drift chamber (He-based gas)	Low material, dN/dx PID
Outer silicon†	Si strips + LGAD	Momentum + TOF
ECAL†	Noble liquid (LAr) + Pb/W absorber	Uniformity, stability
HCAL	Scintillator-steel tiles	PFA granularity
Solenoid†	2 T, outside HCAL	Uninterrupted calorimetry
Muon system†	μ -RWELL	Position resolution
Luminometer	Si-W calorimeter	Precision acceptance

2.3.1 Vertex Detector

The vertex detector was envisioned as an array of ultra-thin Monolithic Active Pixel Sensors (MAPS) in 65 nm CMOS technology, building on the ALICE ITS3 development¹³. The key design choices were:

- Silicon thickness of 20–30 μm per layer, thinned from standard wafer thickness.
- Curved, (partially) self-supporting cylindrical shells, exploiting the geometric rigidity of the curved shape to minimize support material.
- Air cooling, enabled by the low power density of 65 nm MAPS ($\sim 20\text{--}50$ mW/cm²), eliminating coolant pipes and associated material from the active volume.
- First layer as close as possible to the interaction point ($R \approx 12\text{--}13$ mm), with subsequent layers extending to $R \approx 30\text{--}35$ mm.

The target material budget was $\sim 0.02\text{--}0.03\%$ X_0 per layer, or less than 0.1% X_0 for the three innermost layers combined. At FCC-ee energies, where multiple scattering dominates the impact parameter resolution for tracks below ~ 10 GeV, the material budget of the vertex detector is arguably as important a design parameter as its hit resolution.

2.3.2 Inner Silicon Tracker

In CL1a, a set of additional MAPS layers at intermediate radii ($R \approx 80\text{--}300$ mm) was proposed as a distinct subsystem bridging the gap between the vertex detector and the main

tracker. These layers would provide precision space points for pattern recognition seeding and momentum resolution, using the same MAPS technology as the vertex detector but with relaxed pixel pitch ($\sim 20\text{--}25\ \mu\text{m}$). The separation of this into a distinct subsystem was subsequently reconsidered (Section 3.1.3).

2.3.3 Main Tracker: Drift Chamber

A large drift chamber was chosen as the central tracker, similar in concept to the IDEA proposal. The principal arguments were:

- **Low material budget.** A helium-based gas mixture (He: iC_4H_{10} 90:10) contributes negligibly to the material budget ($\sim 0.03\%$ X_0 radially). The wires add $\sim 0.1\text{--}0.2\%$ X_0 .
- **Many measurements per track.** With $\sim 100+$ layers, each track receives many independent position measurements, providing robust pattern recognition and good momentum resolution ($\sim 100\ \mu\text{m}$ per point).
- **Particle identification.** Cluster counting (dN/dx) potentially provides better particle identification than traditional dE/dx truncated mean, with a theoretical resolution of $\sim 2\%$ for a 2 m path length.
- **Proven technology.** Drift chambers have been successfully operated at LEP, SLD, BaBar, Belle, KLOE, and MEG, among others, though cluster counting needs further study.

2.3.4 Outer Silicon Wrapper

A silicon layer at the outer tracker radius ($R \approx 2000\ \text{mm}$) was proposed to provide:

- i) A precision $r\text{-}\phi$ space point for momentum resolution (the outermost measurement has the largest lever arm and therefore the greatest impact on curvature determination).
- ii) Longitudinal position measurement for acceptance control.
- iii) Time-of-flight measurement for π/K separation using Low-Gain Avalanche Detectors (LGADs).

In CL1a, this was envisioned as two layers: a fine-pitch strip layer for position and a separate LGAD layer for timing. This was subsequently reconsidered in favor of a single multi-function layer (Section 3.3).

2.3.5 Electromagnetic Calorimeter: Noble Liquid

The initial choice for the electromagnetic calorimeter was a liquid argon sampling calorimeter with lead or tungsten absorber plates, offering:

- Expected energy resolution of $\sim 7\text{--}10\%/\sqrt{E}$.
- Intrinsic uniformity — the liquid medium is homogeneous by construction, providing stable and uniform response without channel-by-channel calibration.

- Proven technology at scale (ATLAS LAr calorimeter, NA48 LKr calorimeter).
- Fine granularity with user-defined geometry readily achievable with modern multi-layer PCB readout electrodes.
- Multiple longitudinal samplings for shower profiling.

This was one of the subsystem choices in CL1a that underwent the most significant revision through the subsequent discussion (Section 3.4).

2.3.6 Hadronic Calorimeter: Scintillator-Steel Tiles

A scintillator-steel sampling calorimeter with high granularity was chosen, optimized for particle flow reconstruction:

- Steel absorber plates (~ 20 mm) interleaved with scintillator tiles (~ 3 mm thick, $\sim 30 \times 30$ mm²).
- Each tile read out by an individual SiPM.
- ~ 50 layers for ~ 6 nuclear interaction lengths (λ_I).
- The design prioritizes spatial granularity for shower imaging over intrinsic energy resolution.

2.3.7 Solenoid

A 2 T superconducting solenoid was proposed, placed outside the hadronic calorimeter to avoid introducing dead material between the electromagnetic and hadronic calorimeters. The field strength of 2 T was chosen as a compromise between tracking performance (which benefits from higher field) and accelerator compatibility (the solenoid field must be compensated in the interaction region optics, and compensation becomes more difficult at lower beam energies). Both the field strength and the placement were subsequently revised (Section 3.5).

2.3.8 Muon System

The muon system was initially proposed as 3–4 stations of micro-Resistive WELL (μ -RWELL) detectors in the iron return yoke, providing ~ 200 μ m position resolution. This choice was subsequently reconsidered (Section 3.7).

2.3.9 Luminosity Monitor

A precision silicon-tungsten sampling calorimeter at small angles ($\theta \approx 60$ – 100 mrad) was proposed for luminosity measurement through Bhabha event counting, targeting 10^{-4} absolute and 10^{-5} relative precision.

2.4 CL1b: The Initial Complementary Detector

Following the principle of maximal complementarity articulated in Section 2.2, concept CL1b was proposed with deliberately different technology choices for the major subsystems. The intent was that each major physics measurement would be performed with two different detector technologies, providing independent systematic cross-checks.

Table 2.2: CL1a and CL1b compared: technology choices selected to maximize complementarity. Shared elements are listed below.

Subsystem	CL1a	CL1b
Main tracker	Drift chamber	Full silicon tracker
ECAL	Noble liquid (LAr)	Si-W (particle flow)
HCAL	Scint.-steel tiles	Dual-readout fibers
<i>Shared elements in CL1a and CL1b:</i>		
Vertex	MAPS, 65 nm CMOS, curved shells	
Solenoid	Superconducting, ~ 2 T	
Muon system	μ -RWELL in return yoke	
Luminometer	Si-W calorimeter	

The key complementary choices in CL1b were:

- **Tracker:** A full silicon tracker provides excellent spatial resolution at discrete layers but with more material than a gaseous tracker. It offers a fundamentally different systematic profile — silicon tracking is limited by alignment and material knowledge, while drift chamber tracking is limited by calibration of the time-to-distance relationship and wire positions.
- **Electromagnetic calorimeter:** A silicon-tungsten sampling calorimeter with 5×5 mm² pads and ~ 30 longitudinal layers, specifically optimized for the particle flow approach. This provides different shower imaging capability compared to the noble liquid option in CL1a.
- **Hadronic calorimeter:** A dual-readout fiber calorimeter, exploiting the scintillation-to-Čerenkov ratio for event-by-event correction of electromagnetic fraction fluctuations. This attacks the fundamental problem of hadronic calorimetry through a completely different approach than the particle flow strategy of CL1a.

Subsystems where the technology choice is clearer — the vertex detector, solenoid, and luminometer — were kept the same in both concepts. The vertex detector technology (MAPS) is clearly optimal for FCC-ee regardless of other choices. The luminometer design is dictated by the measurement requirements rather than by detector philosophy.

Concepts CL1a and CL1b served as the starting point for the detailed subsystem examination that follows in Chapter 3. As will be seen, several of the technology choices — including some of the most consequential ones — were revised through the subsequent discussion. The resulting concepts, CL2a and CL2b, are presented in Chapter 4. The revisions affected CL1a more significantly than CL1b, reflecting the fact that the detailed examination focused primarily on the technologies chosen for the primary detector.

Chapter 3

Subsystem Examination and Evolution

This chapter documents the detailed examination of each detector subsystem through iterative dialogue between the physicist and the AI. For each subsystem, the AI typically presented an initial technical assessment, the physicist posed questions or challenges drawing on practical experience and physical insight, and the AI revised its analysis in response. Physicist questions are often open-ended to allow the AI to respond; they are occasionally leading when the physicist sees the need. The resulting conclusions reflect this collaborative process. The written account is primarily drafted by the AI, but the intellectual content — particularly the key questions and insights that redirected the analysis — is jointly developed. Where a specific insight originated clearly from one contributor, this is noted in the text.

3.1 Beam Pipe and Vertex Region

3.1.1 Beam Pipe: Material Budget Dominance

The beam pipe is the first material encountered by particles emerging from the interaction point, and its contribution to the material budget sets a floor on the impact parameter resolution that no amount of vertex detector optimization can overcome. A particle originating at the interaction point scatters in the beam pipe wall *before* reaching the first tracking layer, and this scattering cannot be corrected because there is no measurement between the interaction point and the beam pipe.

The beam pipe design for FCC-ee is still under active study. Current expectations are for a liquid-cooled, double-layer structure with a total thickness corresponding to $\sim 0.6\% X_0$ ¹⁴. This is a substantial amount of material — roughly three times the total material budget of the entire six-layer vertex detector described in Section 3.1.3.

The beam pipe inner radius is typically ~ 10 – 12 mm. There is an intimate coupling between the beam pipe design (a machine element), the vertex detector design (an experiment element) and shielding (machine element for the benefit of experimental detector); the machine-detector interface working group treats these as a single optimization problem. Reducing the beam pipe material even modestly would have a direct and significant impact on the vertex detector physics performance, particularly for heavy-flavor tagging at the Z pole where multiple scattering dominates the impact parameter resolution for tracks below ~ 10 GeV.

3.1.2 The Idea of a Sensor Inside the Beam Pipe

Given that the beam pipe dominates the material before the first measurement, the physicist raised a deliberately provocative question: could a sensor layer be placed *inside* the beam pipe, between the interaction point and the beam pipe wall?

Physics motivation

A MAPS layer inside the beam pipe at $R \approx 8\text{--}10$ mm would measure the track position before scattering in the beam pipe wall. With measurements on both sides of the beam pipe, the scattering can be partially measured and corrected, rather than contributing as an irreducible smearing. For impact parameter resolution at low momenta (1–5 GeV), where multiple scattering dominates, this could yield a significant improvement — potentially larger than the 20–40% estimated for a thinner beam pipe, given that the current design has more material to mitigate.

Engineering challenges

The challenges are formidable:

- **Vacuum compatibility.** The sensor would operate in the ultra-high vacuum of the beam pipe ($10^{-9}\text{--}10^{-10}$ Torr). All materials must be UHV-compatible with low out-gassing, ruling out standard PCB substrates and adhesives. The sensor must survive bakeout at 150–200°C.
- **Beam backgrounds.** The region inside the beam pipe is exposed to greater synchrotron radiation from the final-focus quadrupoles, beamstrahlung pairs, and off-momentum particles. A sensor at $R \approx 8\text{--}10$ mm would need to cope with these backgrounds without being overwhelmed.
- **Beam impedance.** Any structure inside the beam pipe affects the beam coupling impedance. With FCC-ee’s high stored beam current (~ 1.4 A at the Z pole), this is a serious concern requiring detailed study.
- **Power and data.** Electrical connections must cross the beam pipe wall through UHV-compatible feedthroughs, constraining the mechanical design.
- **Mechanical constraints.** The sensor area is small (~ 50 cm² at $R = 10$ mm), but alignment to μm precision inside a ~ 20 mm diameter tube is extremely challenging.

Assessment

The sensor-inside-beam-pipe concept is aggressive but not implausible. The FCC-ee environment — little radiation damage and moderate backgrounds compared to hadron colliders, and small sensor area required — makes it more feasible here than at any previous or planned collider. A pragmatic approach would be:

- i) **Baseline:** Minimize beam pipe thickness (0.2–0.3 mm Be) and place the first MAPS layer at the smallest possible radius, essentially touching the outer beam pipe surface. This captures most of the benefit without the vacuum complications.

- ii) **R&D path:** Pursue a dedicated program including UHV compatibility testing of thinned MAPS, beam background simulation, impedance studies, and thermal management in vacuum, with a decision point in the early 2030s.
- iii) **Upgrade option:** Design the beam pipe and vertex detector to be mechanically compatible with a future inner sensor installation, so that if the R&D succeeds, the sensor can be added without redesigning the surrounding systems.

3.1.3 Unified Vertex and Inner Silicon Tracker

The initial separation

In CL1a, the vertex detector (three layers at $R \approx 12\text{--}35$ mm) and the inner silicon tracker (layers at $R \approx 80\text{--}300$ mm) were treated by the AI as separate subsystems. This separation was inherited from LHC detector designs, where the two subsystems genuinely employ different technologies: hybrid pixels at small radii (for radiation hardness and rate capability) and silicon strips at larger radii (for cost-effective coverage of larger areas).

The challenge

The physicist questioned this separation: at FCC-ee, what is the physical basis for distinguishing the vertex detector from the inner silicon tracker?

The question is penetrating because the conditions that motivate the separation at the LHC do not exist at FCC-ee:

- The radiation environment is benign at all radii — there is no threshold radius beyond which a less radiation-hard technology becomes viable.
- The same MAPS technology (65 nm CMOS) works at all radii from 12 mm to 300 mm.
- The power density decreases with radius as hit rates drop off, so air cooling becomes easier, not harder, at larger radii.
- The design philosophy of curved (partially) self-supporting shells with minimal material applies equally at all radii, though the engineering details differ with scale.

Resolution: one unified subsystem

The vertex detector and inner silicon tracker in CL1a are unified into a single subsystem: a set of MAPS layers extending continuously from the beam pipe to the inner wall of the main tracker, using the same base technology throughout. The layer configuration is:

Table 3.1: Unified vertex and inner silicon tracker: layer configuration. All layers use 65 nm CMOS MAPS on curved self-supporting shells.

Layer	Radius (mm)	Pixel pitch (μm)	Thickness (μm)	x/X_0 (%)
1	~ 12	10–15	~ 20	~ 0.02
2	~ 20	10–15	~ 20	~ 0.02
3	~ 35	15	~ 25	~ 0.03
4	~ 90	20	~ 25	~ 0.03
5	~ 160	20–25	~ 30	~ 0.03
6	~ 300	25	~ 30	~ 0.03

The only variation across layers is in pixel pitch (which can be relaxed at larger radii where hit densities are lower and the multiple scattering contribution from inner layers already limits extrapolation precision) and silicon thickness (slightly thicker at larger radii, where the larger physical size of the shells makes handling and assembly more demanding). The specific thicknesses shown in Table 3.1 are illustrative; the actual values will be determined by mechanical prototyping and engineering studies.

The key design features that enable this ultra-low material budget are:

- **Curved (partially) self-supporting shells.** A flat thin membrane is mechanically floppy, but a curved cylindrical shell of the same thickness has significant rigidity against transverse loads. This geometric stiffness, demonstrated by the ALICE ITS3 program¹³, potentially eliminates the need for carbon fiber staves or ladder structures in the active volume.
- **Air cooling.** At power densities of ~ 20 – 50 mW/cm² (achievable in 65 nm CMOS with rolling shutter readout), forced air flow through the gaps between cylindrical shells can remove the dissipated heat. A rough thermal estimate for the innermost layer ($R = 15$ mm, power density 50 mW/cm²) gives a temperature rise of $\sim 17^\circ\text{C}$ with modest air flow (1–2 m/s), which is acceptable in the radiation-benign FCC-ee environment where there is no need to operate at low temperature for leakage current control.

The viability of air cooling eliminates coolant pipes and their associated material from the active volume. This single design choice removes what is typically a major material contribution in vertex detectors at hadron colliders.

- **Integrated signal routing.** Electrical services (power delivery and data readout) are routed via ultra-thin aluminum flex cables, potentially printed directly on the MAPS sensor surface, exiting at the barrel ends. This avoids routing cables through the active tracking volume.

Several aspects require further R&D to validate the design:

- **Air cooling validation.** A realistic prototype with representative power density and geometry should be tested, measuring thermal performance, vibration amplitudes (air flow can excite mechanical resonances in thin shells), and thermal gradients (which cause differential expansion and position shifts).

- **65 nm MAPS at target thickness.** Sensors thinned to 20–30 μm must be characterized for detection efficiency, noise, and long-term stability. While 50 μm has been demonstrated by ALICE ITS3, pushing to 20 μm is more aggressive.
- **Self-supporting shells at larger radii.** The curved shell approach is demonstrated at small radii ($R \sim 18\text{--}30\text{ mm}$). At $R = 300\text{ mm}$ and beyond, multiple wafers are likely necessary to span the length. Whether the self-supporting concept scales to these radii, or whether minimal support structures are needed, requires mechanical prototyping.
- **Beam pipe co-design.** The combined material budget of beam pipe plus first sensor layer should be minimized as a system, in collaboration with the accelerator team.

This unification of vertex and inner silicon into a single subsystem is the first example in this study of a design simplification that emerged from questioning inherited assumptions. The separation was a vestige of LHC thinking that does not survive scrutiny in the FCC-ee context. This change is carried forward into the revised concept CL2a (Chapter 4).

3.2 Main Tracker

The main tracker occupies a large volume in the detector and provides the primary momentum measurement for charged particles. In CL1a, a drift chamber was chosen, similar in concept to the IDEA proposal. The subsequent discussion examined both the drift chamber, straw tubes and the Time Projection Chamber (TPC) alternative in detail, exploring mechanical design, particle identification capability, gas choice, and the practical limitations that separate theoretical performance from achievable performance.

3.2.1 Drift Chamber: Mechanical Design

The IDEA drift chamber concept proposes a large cylindrical chamber with inner radius $\sim 350\text{ mm}$, outer radius $\sim 2000\text{ mm}$, and full length $\sim 4\text{ m}$, containing $\sim 56,000$ wires (sense and field) in a He: $i\text{C}_4\text{H}_{10}$ 90:10 gas mixture. The wires are organized in 112 layers.

The wire tension challenge

The aggregate tension from tens of thousands of wires creates an enormous mechanical load that must be borne by the end structures. The IDEA collaboration estimates a total wire tension load of $\sim 10^5\text{ N}^{15}$, acting axially and pulling the two ends of the chamber toward each other.

In a conventional drift chamber, this load is carried by rigid end plates — flat or slightly domed structures spanning the full annular area of the chamber. For the IDEA geometry ($R_{\text{inner}} \approx 350\text{ mm}$, $R_{\text{outer}} \approx 2000\text{ mm}$), a conventional aluminum end plate thick enough to resist this load without excessive deflection would be $\sim 10\text{--}30\text{ mm}$ thick, contributing $\sim 10\text{--}20\%$ X_0 of material, significantly degrading the measurement for any track passing through the forward region.

Spokes and stays: the IDEA solution

The IDEA collaboration proposes replacing the conventional end plates with a system of *spokes* and *stays*, as illustrated schematically in Figure 3.1.¹

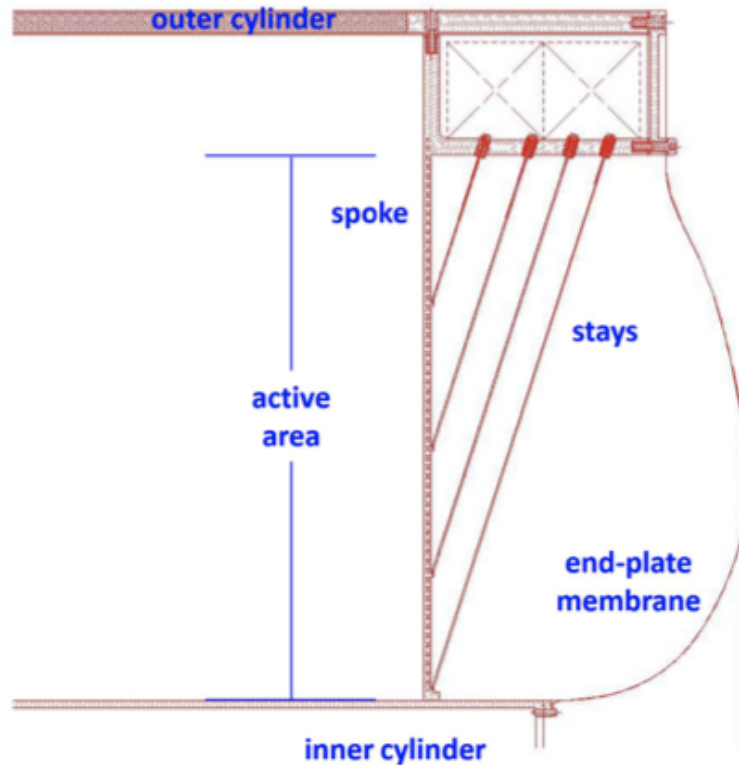


Figure 3.1: Schematic layout of the tension recovery system in the IDEA drift chamber. The stays act as tension members connecting points along the spoke to the outer cylinder, analogous to the cables of a cable-stayed bridge. Figure adapted from Ref. ¹⁶.

The **spokes** are radial structural members at each end of the chamber, running from the inner cylinder to the outer cylinder. They replace the continuous end plate with a discrete set of narrow members (typically 8–16 spokes per end), leaving most of the azimuthal space open.

The **stays** are tension members — essentially thin cables or wires — that fan from attachment points along each spoke outward to the outer cylinder. They function precisely like the cables of a cable-stayed bridge, with the spoke as the deck and the outer cylinder as the anchor. Each spoke has ~ 15 stays, corresponding to attachment points at different radii where groups of wire layers transfer their tension.

An **end-plate membrane** provides gas tightness without carrying structural load. Because it is not structural, it can be made very thin. Care must be taken to minimize diffusion

¹The discussion of the spoke and stay geometry benefited from a schematic drawing from the IDEA collaboration⁵, shared by the physicist during the dialogue.

of helium through this membrane.

Material comparison: spokes vs. end plates

The material advantage of spokes over end plates is substantial. A conventional aluminum end plate spanning the full annular area of the chamber would need to be $\sim 10\text{--}30$ mm thick to resist the wire tension without excessive deflection, contributing $\sim 10\text{--}20\%$ X_0 of material for any track passing through the forward region. In contrast, a set of ~ 12 narrow spokes occupies only a few percent of the azimuthal acceptance, and the azimuth-averaged material is significantly less than a continuous end plate. The detailed mechanical design, including spoke and stay dimensions for the actual wire tension load of $\sim 10^5$ N¹⁵, is being carried out by the IDEA collaboration; the qualitative advantage of the spoke approach over conventional end plates is decisive regardless of the precise dimensions.

Since the total azimuthal obstruction is approximately independent of the number of spokes — fewer thick spokes or more thin spokes give similar total filling fractions — the choice of spoke count can be driven by practical considerations such as manufacturing, wire feedthrough hardware, and assembly.

Longitudinal space and engineering considerations

The stays fan from attachment points along each spoke to the outer cylinder, with the innermost stays spanning the largest radial distance and therefore requiring the most longitudinal space. The stay angle represents a trade-off: steeper angles (more nearly radial) reduce the longitudinal extent but require higher stay tension to cancel the axial wire load; shallower angles are more efficient structurally but consume more space. The detailed optimization of stay geometry, spoke cross-sections, and the resulting force balance is an engineering task that the IDEA collaboration is actively pursuing¹⁵.

The key implication for the overall detector layout is that the stay system consumes significant longitudinal space beyond the active wire volume — perhaps up to several hundred millimeters per end. This space is not available for endcap tracking or calorimetry, and represents a meaningful constraint on the detector layout (Section 4.1.1).

Other well-known engineering challenges — wire gravitational sag, electrostatic deflections, and the time-to-distance calibration — are standard issues in drift chamber design that must be carefully modeled and corrected in reconstruction but do not raise concerns specific to the FCC-ee application.

One consideration that deserves attention in the context of the spoke-and-stay design is **electronics cooling**. In a conventional drift chamber with solid end plates, the end plate serves as a natural heat sink for the front-end electronics mounted on its outer surface, and cooling pipes can be routed along or integrated into the plate structure. With the spoke-and-stay approach, this continuous thermal path is absent. The front-end electronics — particularly if waveform digitization for cluster counting is pursued (Section 3.2.2) — can dissipate substantial power that must be removed from a mechanically sparse structure. Even with conventional dE/dx readout, the electronics cooling must be addressed through dedicated cooling paths integrated into the spoke structure or through separate cooling manifolds in the end region. An alternative approach is to locate electronics away from wire ends to

a location with simpler thermal management. However, the cables needed to transmit signals add to the material budget and can degrade electronic performance. These are solvable engineering problems; their costs and benefits should be examined carefully in the overall design.

3.2.2 Drift Chamber: Cluster Counting

One of the headline capabilities of the IDEA drift chamber is particle identification through cluster counting (dN/dx) — counting the individual primary ionization clusters along a track rather than measuring the total ionization charge (dE/dx). The projected performance is substantially better than conventional dE/dx , but significant challenges have to be overcome for this projection.

The theoretical promise

The projected performance is based on a simple statistical argument. A charged particle traversing the He:iC₄H₁₀ 90:10 gas mixture produces an average of ~ 12 primary ionizations per cm. For a 200 cm path length (representative of a track at moderate polar angle), the total number of primary clusters is:

$$N_{\text{total}} = 12 \times 200 = 2400 \quad (3.1)$$

Assuming Poisson statistics, the resolution on the cluster count is:

$$\frac{\sigma_N}{N} = \frac{1}{\sqrt{N}} = \frac{1}{\sqrt{2400}} \approx 2.0\% \quad (3.2)$$

This 2% resolution, if achieved, would provide excellent π/K separation: 3- σ significance up to 30 GeV in momentum¹⁷.

The subsequent discussion identified several effects that degrade this idealized performance. These are examined in turn below.

Delta ray contamination

Each primary ionization ejects an electron from a gas atom. The energy transferred to this electron follows an approximately $1/E^2$ distribution: most transfers are just above threshold, but occasionally a large energy transfer produces an energetic secondary electron (delta ray).

The consequences for cluster counting depend on the delta ray energy and hence its range:

- **Low-energy secondaries** (the majority of cases): the ejected electron travels only a few microns or less and remains spatially coincident with the primary ionization. The result is a multi-electron cluster rather than multiple separate clusters. At the point of production, this does not increase the cluster count — it simply makes the cluster have higher charge. However, as the multi-electron cluster drifts toward the sense wire, diffusion causes the individual electrons to separate. If the separation exceeds the resolving threshold of the electronics, what was produced as a single cluster may be *detected* as multiple clusters. This effect is discussed further under diffusion (Section 3.2.2).

- **Moderate-energy delta rays** ($\sim 300\text{--}1000$ eV, range $\sim 50\text{--}200$ μm): these travel far enough that their secondary ionization is spatially separated from the primary cluster even before drift. These create genuinely additional clusters that are counted separately, inflating the cluster count. Crucially, if the delta ray remains within the same drift cell as the primary ionization, there is no topological information to distinguish its clusters from genuine primary ionization clusters.
- **High-energy delta rays** ($>$ a few keV): these have ranges of millimeters or more and may cross cell boundaries, where they can potentially be identified topologically as short track stubs at large angles to the primary track. These are in principle removable, though the pattern recognition is challenging for marginal cases.

The physicist identified the concern: for moderate-energy delta rays that remain within the same drift cell, **there is no way to distinguish the extra clusters from genuine primary ionization clusters**. The contamination from moderate-energy delta rays necessarily degrades the dN/dx resolution: the measured cluster count is the sum of the true primary count and the contamination count, and the variance of the sum is the sum of the variances, regardless of the shape of the contamination distribution. The achievable resolution is therefore broader than the $1/\sqrt{N}$ Poisson floor from primary ionization statistics alone.

Diffusion effects

As ionization electrons drift toward the sense wire, they undergo random thermal diffusion. For He:iC₄H₁₀ at typical drift fields, the longitudinal diffusion coefficient is $D_L \approx 100\text{--}200$ $\mu\text{m}/\sqrt{\text{cm}}$, giving a spatial spread of $\sigma_x \approx 60\text{--}130$ μm at the maximum drift distance of ~ 7 mm.

Diffusion causes two competing effects:

Splitting of multi-electron clusters. A primary ionization that produces multiple electrons (e.g., a 3-electron cluster) sees its electrons diffuse independently during drift. At maximum drift distance, the separation between electrons from the same cluster ($\sigma_{\text{sep}} \approx \sqrt{2}\sigma_x \approx 130$ μm) frequently exceeds the resolving threshold. Each electron then appears as a separate arrival at the sense wire, inflating the cluster count. The physicist identified the key point: **once a multi-electron cluster has split, the individual electrons are indistinguishable from genuine single-electron primary clusters**.

Merging of separate clusters. Conversely, electrons from two genuinely separate primary ionizations can diffuse together and arrive at overlapping times, appearing as a single cluster with higher charge and reducing the count.

Both effects are drift-distance-dependent (worse at longer drift), creating systematic position-dependent biases within each cell. Even if the mean effects partially cancel, the variances from splitting and merging add, degrading the resolution beyond the Poisson floor.

Once a multi-electron cluster has split during drift, each fragment is typically a single electron, identical in every measurable respect to a genuine single-electron primary cluster. No amplitude or timing analysis can identify it as a split fragment — **a single electron carries no memory of its origin**.

For the converse problem — merging, where two separate primary clusters arrive at overlapping times and appear as a single pulse — one might hope to use amplitude to flag the merged pair, since two electrons arriving together should produce a larger signal than one. However, the gas amplification process at the sense wire is inherently stochastic: for a single electron, the avalanche size follows a distribution with $\sim 100\%$ relative fluctuation. The distributions for one-electron and two-electron pulses overlap enormously, making reliable discrimination impractical.

Furthermore, the effective gain is not constant along the cluster arrival time series. Positive ions from earlier avalanches create space charge near the wire that reduces the effective field for subsequent avalanches. This space charge effect is position-dependent within each cell, event-dependent, and track-angle-dependent (tilted tracks spread ionization along the wire in z , reducing the space charge concentration). A merged two-electron cluster arriving late in the sequence may have a smaller amplitude than a single electron arriving early, further undermining any amplitude-based discrimination.

Electronics requirements

The mean cluster arrival rate of ~ 50 MHz (corresponding to ~ 20 ns mean spacing) sets the minimum bandwidth for the front-end electronics. Modeling the time separation distribution as approximately exponential with a mean of ~ 20 ns, the required electronics bandwidth depends on the target cluster-pair resolving efficiency:

Table 3.2: Required electronics bandwidth as a function of target cluster-pair resolving efficiency.

Target efficiency	Required δ_t (ns)	Required bandwidth (MHz)
50%	14.5	~ 35
70%	7.5	~ 67
80%	4.7	~ 106
90%	2.2	~ 227
95%	1.1	~ 470

To resolve $\sim 90\%$ of cluster pairs, the front-end electronics must have analog bandwidth of several hundred MHz. The subsequent digitization must sample the waveform above the Nyquist rate, implying sampling rates in the GS/s range. Compared to conventional drift chamber readout (where each wire produces a drift time and an integrated charge per event), cluster counting requires substantially greater electronics resources across multiple dimensions: analog bandwidth must increase from tens of MHz to hundreds of MHz; front-end power per channel increases correspondingly; digitization rates move from the MS/s range to the GS/s range; and the data volume per hit wire increases by one to two orders of magnitude (from a few tens of bits for a time and charge measurement to hundreds or thousands of bits for a sampled waveform or a list of individual cluster times and amplitudes). On-chip cluster finding can reduce the data volume significantly, but at the cost of precluding reprocessing of raw waveforms with improved algorithms later.

These increased requirements cascade into higher total power dissipation, greater data bandwidth, and more complex front-end ASICs, all of which must be weighed against the improvement in particle identification performance that cluster counting provides over conventional dE/dx .

Gas choice optimization

The conventional wisdom for cluster counting is to maximize the primary ionization rate n_{primary} , since the Poisson resolution improves as $1/\sqrt{n_{\text{primary}} \times L}$. This favors heavier gases (argon-based mixtures with $\sim 25/\text{cm}$) over helium-based ($\sim 12/\text{cm}$).

The physicist suggested a counterintuitive alternative: could a gas with *lower* primary ionization actually perform better in practice? The argument is that with fewer clusters per unit time:

- The merging fraction decreases (clusters are more separated).
- The electronics bandwidth requirements relax.

The trade-off is that the Poisson floor worsens (e.g., from 2.0% to 2.5% for a reduction from 12/cm to 8/cm). But if the practical degradations discussed above are large enough, there may be an optimum n_{primary} that minimizes the *actual* resolution rather than the theoretical floor.

Similarly, the physicist noted that a gas with lower drift velocity would spread clusters further apart in the time domain, potentially improving resolvability. However, the benefit depends on the details of the gas mixture: changing the drift field affects both drift velocity and diffusion, and the two do not in general scale in the same way. The improvement from lower drift velocity is most likely to be realized when the electronics resolving time, rather than diffusion, is the dominant limitation on cluster separation. These considerations suggest that the gas optimization for cluster counting deserves a systematic study, using both simulation and empirical measurements, that accounts for all practical effects simultaneously, rather than optimizing solely for maximum n_{primary} .

Realistic performance assessment

Taking the delta ray contamination, diffusion effects, left-right folding², and electronics limitations together, the achievable dN/dx resolution is likely to be worse than the theoretical floor of 2%. The dominant degradations are:

- Delta ray contamination: adds non-Gaussian variance that cannot be removed for same-cell delta rays.
- Diffusion-induced splitting and merging: adds drift-distance-dependent variance beyond Poisson.

²Clusters produced on the two sides of a sense wire share a common drift time, doubling the effective cluster density in the time domain over a naive estimate. This is an example where the physicist had to take decisive action to change the AI's perspective. In this case, the consideration led to greater electronics bandwidth demands.

This worsened resolution may still represent an improvement over conventional dE/dx truncated mean (typically $\sim 5\text{--}6\%$ in drift chambers), though the improvement is **more modest than the factor-of-two-or-more suggested by the idealized calculation**. Particle identification at low momenta (up to a few GeV) is provided by time-of-flight measurement from the outer silicon wrapper (Section 3.3), independent of the drift chamber readout approach. At higher momenta, where the physics interest is greatest, the relevant question is whether the improvement from cluster counting (dN/dx) over conventional dE/dx — after accounting for the practical limitations discussed above — justifies the substantially greater electronics resources and service requirements. This question deserves careful study through detailed simulation with realistic cluster-finding algorithms.

3.2.3 Conventional End Plate Drift Chamber

Before the IDEA spoke-and-stay design, all large drift chambers at e^+e^- colliders — including those at LEP (OPAL), SLC (SLD), and the B-factories (BaBar, Belle) — used conventional end plates to carry the wire tension load. This proven approach deserves consideration for FCC-ee as a lower-risk alternative to the spoke-and-stay system.

What stays the same

In the barrel tracking volume, a conventional end plate drift chamber with He:iC₄H₁₀ gas is essentially identical to the IDEA concept: the same gas, similar wire configurations, similar spatial resolution per layer, and similar material budget from gas and wires ($\sim 0.2\%$ X_0 radially). The helium-based mixture remains the gas of choice for its low material budget and moderate primary ionization rate. The cluster counting capability and its associated challenges (Section 3.2.2) are unaffected by the choice of end structure — the ionization physics is identical.

The end plate trade-off

The key difference is at the chamber ends. A conventional end plate is a continuous structural disc (or annular ring) spanning the full chamber aperture, carrying the aggregate wire tension of $\sim 10^5$ N¹⁵. End plate thickness can be reduced through careful engineering — for example, the SLD drift chamber used a curved end plate geometry in which the membrane tension reduced the bending stress at the junction with the outer cylinder, achieving a thinner plate than a flat design would require. Nevertheless, the end plate material traversed by forward tracks is substantial — typically several 10's percent X_0 or more.

However, the total material in the end region is not dominated by the end plate alone. Front-end electronics boards, power cables, data cables, cooling manifolds, and cable routing collectively contribute material that is likely comparable to the structural plate itself. Much of this service material is present regardless of whether the end structure is a conventional plate or a spoke-and-stay system — the electronics must be housed and cooled in either case.

Advantages over the spoke-and-stay approach

- **Proven engineering.** Conventional end plates have been designed, built, and operated successfully in multiple large drift chambers over decades. The engineering is well-understood with no unresolved R&D questions.
- **Longitudinal space.** The end plate is compact in z — typically a few centimeters of structural material plus the electronics layer immediately behind it. This is substantially less longitudinal space than the ~ 500 – 800 mm consumed by the IDEA stay system (Section 3.2.1), freeing space for endcap detectors.
- **Electronics mounting and cooling.** The end plate provides a natural rigid surface for mounting front-end electronics and a thermal path for cooling. With the spoke-and-stay approach, the absence of a continuous end plate complicates electronics cooling, particularly if high-power waveform digitization for cluster counting is pursued (Section 3.2.2).
- **Lower engineering risk.** No novel mechanical concepts are required. The design can draw directly on the extensive experience base from previous chambers.

Disadvantages

- **Forward region material.** The end plate and associated services represent several 10's percent X_0 of material at small polar angles. This has two consequences. First, if endcap tracking layers (silicon disks) are placed beyond the end plate, the intervening material degrades the combined track fit through multiple scattering. Second, and perhaps more importantly, this material sits directly in front of the endcap electromagnetic calorimeter, degrading photon energy resolution and π^0 reconstruction in the forward region through early shower initiation — an effect analogous to the cryostat dead material discussed for noble liquid barrel calorimeters (Section 3.4.1).
- **Non-uniform material distribution.** The material is concentrated in a narrow z range (the end plate location), creating a sharp transition between the low-material barrel region and the high-material end plate. This complicates the acceptance modeling for precision measurements.

Assessment

The conventional end plate drift chamber is a viable and low-risk option for FCC-ee. Its barrel performance is essentially identical to the IDEA concept, and its engineering is thoroughly proven. The trade-off is additional material in the forward region, partially offset by the recovery of longitudinal space and the practical advantage of a natural electronics mounting and cooling surface.

The choice between conventional end plates and the IDEA spoke-and-stay system depends on how heavily one weights forward-region material (favoring IDEA) versus engineering simplicity and longitudinal compactness (favoring conventional end plates). For the CL2a concept, the spoke-and-stay approach is adopted following the IDEA design philosophy, but

the conventional alternative remains a credible fallback with lower engineering risk. A quantitative comparison — evaluating the impact of end plate material on specific Z-pole physics measurements against the benefit of recovered longitudinal space for endcap detectors — would help clarify this trade-off.

3.2.4 Straw Tube Alternative

Straw tubes offer an alternative implementation of the drift chamber concept in which each sense wire is enclosed in a thin metallized tube that serves as both cathode and cell boundary, replacing the field wires of a conventional drift chamber. This approach has operational advantages: the cylindrical geometry gives a clean $1/r$ electric field with a well-understood time-to-distance relationship; a broken sense wire is contained within its straw and cannot affect neighboring cells; and individual straws can be tested before integration into the full chamber.

However, for the FCC-ee application, straw tubes present several challenges relative to the wire drift chamber:

- **Material budget.** Even with $12\ \mu\text{m}$ wall Mylar tubes (at the frontier of what has been prototyped), the cumulative straw wall material for a radial track traversing ~ 165 layers is $\sim 1.4\%$ X_0 from the tube walls alone — roughly $7\times$ the material of the IDEA drift chamber (gas + wires). With support structures included, the total material is comparable to that of a full silicon tracker ($\sim 1\text{--}2\%$ X_0). This does not meet the momentum resolution target at low momenta, though it is worth noting that silicon tracker concepts such as CLD has a similar material budget.
- **Stereo geometry.** In a wire drift chamber, stereo wires run at a small angle to the beam axis, and the cell boundaries defined by the wire positions naturally adapt along z — the cell size varies smoothly from midplane to endplate. A straw tube has a fixed diameter along its length. Tubes that are close-packed and provide full azimuthal coverage at the end plates overlap and clash for smaller $|z|$, while close-packed tubes that provide full coverage at the midplane develop gaps at the endplates when tilted for stereo. This gap size grows with stereo angle; for typical angles of ~ 50 mrad over a 2 m half-length, the displacement at the endplate (~ 100 mm) is many straw diameters, creating substantial coverage gaps. A possible mitigation is to use mostly axial straws with a few stereo layers at small angles, accepting moderate gaps and reduced z resolution compared to a full-stereo wire chamber.
- **Mechanical support.** A $12\ \mu\text{m}$ Mylar tube cannot withstand the axial tension of its sense wire — the critical buckling load for such a thin-walled cylinder is far too low. The total wire tension load (comparable to that of a conventional drift chamber) must therefore be carried by end plates held apart by compression struts through the active volume. This reintroduces end plate material in the forward region that the IDEA spoke-and-stay design was specifically created to minimize.
- **Fabrication complexity.** Since individual straws cannot support their own sense wire tension, each straw requires an external fixture to bear the wire load during fabrication and testing, until the straw is integrated into the full chamber with end plates providing

the reaction force. This complicates the production process for tens of thousands of straws.

The particle identification capability (dE/dx or dN/dx) is not fundamentally different between straw tubes and a wire drift chamber — the ionization physics, delta ray production, diffusion, and cluster counting challenges discussed in Section 3.2.2 apply equally to both.

The straw tube approach offers real operational advantages in fault isolation and field geometry simplicity, and its material budget, while substantially greater than the IDEA wire chamber, is not greater than that of a silicon tracker. It is not adopted for the CL2a concept, where the IDEA-style wire drift chamber achieves lower material budget and better stereo z coverage, but it could merit consideration for applications where the operational advantages outweigh the material penalty.

3.2.5 Time Projection Chamber

The TPC was considered as an alternative to the drift chamber for the main tracker. The discussion assumed operation at atmospheric pressure with modern MicroPattern Gaseous Detector (MPGD) such as GEM or Micromegas readout, similar to the ALICE TPC upgrade, the ILD-FCCee concept, and the CEPC Reference Detector¹¹.

Advantages of true 3D reconstruction

The TPC's defining feature is that every hit is a true three-dimensional space point. The r - ϕ coordinates come from the pad position on the endcap readout plane, and z comes from the drift time. This provides several concrete advantages over a drift chamber:

- **Pattern recognition.** With 3D points, track finding is a search for helical patterns in a point cloud with no combinatorial ambiguities. There is no left-right ambiguity (present in drift chambers) and no stereo matching required for the z coordinate. This makes pattern recognition more robust in complex event topologies — jets, displaced vertices, kinks, and V^0 s.
- **z resolution.** Every TPC hit provides a z coordinate directly from the drift time, with a resolution of ~ 1 mm. This means every measurement point is a true 3D space point, without requiring the combination of axial and stereo layers needed in a wire drift chamber to obtain z information.
- **Uniform coverage.** The TPC provides measurements throughout its volume with no dead regions from wire support structures, spokes, or stays. The active volume is purely gas.

Gas choice

The long drift distance in a TPC (~ 2 m per half-chamber) makes transverse diffusion a critical design constraint. Physicist pointed out that this requirement is in tension with the preference for a light gas to minimize material budget. Adequate diffusion suppression requires two complementary mechanisms: magnetic field suppression (effective in any gas with

a strong solenoidal magnetic field parallel to the drift direction) and the Ramsauer-Townsend (RT) effect, a quantum mechanical minimum in the electron-atom elastic scattering cross-section that occurs in argon, krypton, and xenon but is absent in helium and neon.

With both mechanisms active in an optimized argon-based mixture at 2 T, transverse diffusion over 2 m of drift is suppressed to the mm level, competitive with the per-point resolution of a drift chamber.

The material budget trade-off

The Ramsauer-Townsend effect creates a tension between diffusion performance and material budget. The best TPC gases for diffusion suppression (argon-based) are significantly heavier than the best gases for material budget (helium-based):

Table 3.3: Material budget comparison for different tracker gas options over a ~ 1.65 m radial path length at atmospheric pressure.

Gas option	Density (mg/cm ³)	x/X_0 (%)
He:iC ₄ H ₁₀ 90:10 (drift chamber)	0.26	0.03
Ne:CO ₂ 90:10 (TPC)	0.88	0.48
Ar:CH ₄ 90:10 (TPC)	1.56	1.5
Ar:CF ₄ 95:5 (TPC)	1.70	1.5

The argon-based TPC gas contributes $\sim 1.5\%$ X_0 radially — a factor of ~ 50 more than the helium-based drift chamber gas. For low-momentum tracks from B and D hadron decays at the Z pole, where multiple scattering limits the impact parameter resolution even after the vertex detector, this is a significant disadvantage.

A helium-based TPC would avoid the material penalty but would not benefit from the RT effect, relying solely on magnetic field suppression for diffusion control. The resulting resolution at maximum drift would be substantially worse than in an argon-based TPC.

The drift chamber sidesteps this dilemma entirely: it uses helium (lightest gas, minimal multiple scattering) and does not need long-range diffusion suppression because the drift distances are short (~ 7 mm per cell). It is worth noting that the TPC gas material ($\sim 1.5\%$ X_0) is comparable to that of a straw tube tracker or a full silicon tracker (Section 3.2.4) — the material penalty is a common feature of all main tracker options other than the helium wire drift chamber.

Ion back-flow management

Ion back-flow (IBF) — the drift of positive ions from the amplification stage back into the TPC drift volume — creates space charge that distorts the electric field and degrades spatial resolution. This was historically the TPC’s most serious operational challenge.

The discussion confirmed that IBF is now considered manageable for FCC-ee conditions through a two-pronged strategy:

Passive suppression: Multi-GEM stacks (as used in the ALICE TPC upgrade¹⁸) achieve IBF ~ 0.5 – 1% through geometric/electrostatic trapping of ions at each GEM stage.

This works continuously without active gating or dead time, compatible with FCC-ee’s continuous readout requirement.

Calibration of residual distortions: The remaining IBF creates slowly-varying space charge distortions that can be measured and corrected using:

- Laser calibration tracks at known positions, providing an absolute distortion map.
- Track-based calibration using reconstructed tracks (which should be smooth helices in a uniform field), providing high-statistics fine-grained corrections¹⁹.

At FCC-ee’s Z-pole event rate (~ 100 kHz), the IBF-induced space charge density is much lower than in ALICE Pb-Pb collisions, where the technique has been successfully demonstrated. The CEPC collaboration has performed detailed studies reaching similar conclusions for Higgs factory conditions¹².

Active gating (opening and closing a wire grid to block ions) is not viable for FCC-ee because it introduces dead time incompatible with continuous readout at the ~ 20 ns bunch spacing.

Rate capability and pile-up

The TPC’s long drift time (~ 80 μ s for 2 m drift at $v_d \approx 2.5$ cm/ μ s) means multiple physics events are simultaneously present in the drift volume. At the Z-pole rate of ~ 100 kHz:

$$N_{\text{pileup}} \approx 10^5 \times 80 \times 10^{-6} \approx 8 \text{ events} \tag{3.3}$$

These eight overlapping events produce ~ 160 tracks spread over $\sim 50,000$ readout pads per row — a manageable occupancy. The tracks can be associated to the correct event using timing information from the vertex detector and outer silicon wrapper, which have nanosecond-level time resolution.

The drift chamber, with its ~ 200 – 350 ns drift time per cell, has essentially zero pile-up at any FCC-ee energy point. This is a practical advantage, though not a decisive one given that TPC pile-up is manageable.

3.2.6 Drift Chamber vs. TPC: Comparative Assessment

Table 3.4 summarizes the comparison.

Both options are viable for FCC-ee, and neither is clearly superior overall. The drift chamber’s advantages in material budget and calibration robustness are counterbalanced by the TPC’s superior 3D reconstruction and z resolution.

The material budget argument favors the drift chamber, particularly for low-momentum tracks at the Z pole where multiple scattering in the tracker volume degrades the momentum resolution.

The z resolution argument favors the TPC, particularly for acceptance determination at the Z pole where $\cos\theta$ -dependent systematics must be controlled at extreme precision.

For the CL2a concept (Chapter 4), the drift chamber is retained as the baseline, primarily for its lower material budget. However, the TPC is recommended as the tracker for the complementary detector CL2b, providing maximal complementarity in tracking technology

Table 3.4: Drift chamber vs. TPC: comparative assessment for FCC-ee.

Property	Drift chamber	TPC
Material (gas)	Excellent ($\sim 0.03\% X_0$)	$\sim 1.5\% X_0$ (Ar-based, RT required)
r - ϕ resolution	$\sim 100 \mu\text{m}$, uniform	$\sim 100 \mu\text{m}$, z-dependent
z information	Requires axial + stereo layer combination $\sim 1 \text{ mm}$	Every hit, $\sim 1 \text{ mm}$
3D reconstruction	2D per layer + stereo	True 3D per hit
Pattern recognition	Left-right ambiguity, stereo matching required	Unambiguous, robust
Pile-up	Negligible	~ 8 events at Z pole
Calibration	Local (per wire/cell)	Global (drift field, space charge)
PID	dE/dx ; dN/dx under study	dE/dx ; dN/dx to be investigated
Maintainability	Front-end boards replaceable; wire repair difficult	Endcap modules replaceable; field cage monolithic
Forward material	Spokes (localized)	Readout endcap (continuous)

and systematic profile. The extensive TPC studies by the CEPC collaboration and the ILD-FCCee concept provide a strong foundation for this choice.

The main tracker technology remains, in our assessment, resolved and would benefit from a direct simulation comparison under FCC-ee conditions, including realistic material budgets, pattern recognition performance in complex events, and the impact of gas material on vertexing performance at the Z pole.

3.3 Outer Silicon Wrapper

The outer silicon wrapper sits at the boundary between the main tracker and the electromagnetic calorimeter, at $R \approx 2000$ mm. In CL1a, it was envisioned as two separate layers with distinct functionalities: silicon strips to determine position for momentum measurement and LGADs for timing. The subsequent discussion refined both the functional requirements and the technology choice.

3.3.1 Three Functions in Priority Order

The physicist proposed a clear priority ordering for the wrapper's functions, which shaped the subsequent technology discussion:

- i) **Precision r - ϕ space point for momentum resolution.** The outermost measurement point has the largest lever arm and therefore the greatest weight in the track curvature determination. A single high-precision r - ϕ point at $R \approx 2000$ mm with $\sigma_{r\phi} \approx 7$ – 10 μm provides a constraint equivalent to many drift chamber points. This alone justifies the wrapper.
- ii) **Longitudinal (z) position for acceptance determination.** At the Z pole with 10^{12} Z bosons, statistical uncertainties are negligible and acceptance edges in $\cos\theta$ must be known at the 10^{-4} level. This requires good z resolution at the outer radius. At $R = 2000$ mm, a z resolution of $\sigma_z \sim 1$ mm gives $\sigma_\theta \sim 0.5$ mrad — adequate but not generous. Better z resolution is desirable.

The physicist noted that since the z -resolution requirement is of order a few hundred microns rather than ~ 10 μm , strip sensors (as discussed below), arranged as a stereo doublet, can provide adequate z measurement regardless of the specific sensor technology. This significantly reduces the channel count compared to a pixel implementation at $R = 2000$ mm.

- iii) **Time-of-flight for particle identification.** With a flight path of ~ 2 m and TOF resolution of ~ 30 ps, π/K separation at 3σ level extends to ~ 3.5 GeV.³ This complements the dE/dx (or dN/dx) measurement from the main tracker, which provides separation at higher momenta. The combination gives continuous π/K coverage over most of the relevant momentum range at the Z pole.

³A useful mnemonic: the time-of-flight difference between a 1 GeV/ c pion and kaon over 2 m is ~ 750 ps. This time difference scales linearly with flight distance and inversely with p^2 .

This priority ordering has a practical consequence: the technology choice should be optimized primarily for the first function (position) and must not compromise it in pursuit of the third (timing).

3.3.2 LGAD Technology Options

The discussion examined several LGAD variants for their ability to serve all three functions simultaneously in a single sensor layer, minimizing the total material.

Conventional LGAD

Standard LGADs have pad sizes of $\sim 1 \times 1 \text{ mm}^2$ or larger, limited by the junction termination structure between pads that creates a dead no-gain region of $\sim 50\text{--}100 \text{ }\mu\text{m}$ width. The position resolution is $\sim 1 \text{ mm}/\sqrt{12} \approx 300 \text{ }\mu\text{m}$ — completely inadequate for the precision $r\text{-}\phi$ measurement. Timing is excellent with $\sim 30 \text{ ps}$ demonstrated, but conventional LGADs cannot serve as the precision space point layer.

AC-LGAD (Resistive Silicon Detectors)

AC-LGADs use a continuous gain layer (no inter-pad dead zones) with a resistive sheet and AC-coupled readout pads. The signal from any point spreads through the resistive layer and is detected by multiple neighboring pads, enabling position reconstruction from the charge sharing pattern.

Demonstrated performance includes position resolution of $\sim 5\text{--}15 \text{ }\mu\text{m}$ (depending on pitch and resistivity) and timing of $\sim 30\text{--}40 \text{ ps}$ — potentially meeting all three functional requirements in a single sensor.

However, the physicist identified a potential vulnerability: the charge sharing mechanism that enables position resolution is compromised when multiple tracks hit the sensor within the signal spreading distance ($\sim 1 \text{ mm}$). The overlapping charge clouds produce a biased or ambiguous position reconstruction.

Studies of machine learning approaches to disentangle overlapping hits indicate that performance can be characterized in three regimes, based on the fundamental signal overlap geometry:

- Well-separated hits (separation $> 1.5 \times$ spreading distance): both positions recovered with near-single-hit resolution.
- Moderately close hits ($\sim 1 \times$ spreading distance): positions recoverable with degraded resolution ($\sigma \sim 20\text{--}50 \text{ }\mu\text{m}$).
- Very close hits ($< 0.5 \times$ spreading distance): genuinely degenerate; even ML cannot reliably separate them.

The physicist noted that while the average track density at $R = 2000 \text{ mm}$ is low, the cases where two tracks are close are precisely the cases where momentum resolution matters most (e.g., the core of a boosted jet). Losing a precision point at the end of a track seriously affects that individual track’s momentum measurement.

The ML disentangling techniques, while promising, are strongly dependent on the specific sensor geometry, require very accurate simulation for training, and have not been validated under real detector conditions with non-uniformities and long-term variations. The assessment is **promising but not yet proven** at the level needed for a precision measurement.

Trench-Isolated LGAD (TI-LGAD)

TI-LGADs use deep narrow trenches between readout elements (filled with insulating material) to provide electrical isolation while maintaining high fill factor (>95%) even for fine pitch. Each readout element has its own independent gain region, so there is no charge sharing between neighboring elements.

Key properties:

- Position resolution determined by pitch: $\sigma \sim \text{pitch}/\sqrt{12}$. For a strip pitch of 50 μm , this gives $\sigma \approx 15 \mu\text{m}$ in r - ϕ .
- Timing ~ 30 – 40 ps, comparable to standard LGADs²⁰.
- **Multi-hit capability is inherently robust** — each readout element is independent, so two hits on adjacent strips are cleanly separated with no charge sharing ambiguity.

Compared to AC-LGADs, the TI-LGAD position resolution is binary (hit or no hit per strip) rather than derived from analog charge sharing. While the achievable resolution is somewhat coarser for the same pitch ($\sim 15 \mu\text{m}$ vs. ~ 5 – $15 \mu\text{m}$ for AC-LGADs), it is fully adequate for the wrapper’s r - ϕ requirement and has the significant advantage of being immune to the multi-hit confusion discussed above.

Technology assessment

For CL2a, the AC-LGAD is preferred as the baseline technology for a single-layer outer wrapper, primarily because:

- The track density at $R = 2000$ mm is low — the fraction of tracks affected by multi-hit confusion is small; however this should be confirmed by detailed physics simulation of the applicable use cases.
- The material savings of a single thin layer (vs. separate strip + LGAD layers) for calorimeter performance.
- Both AC-LGAD technology and the ML disentangling techniques will continue to mature before the FCC-ee construction timeline.

The TI-LGAD is maintained as a backup that could become preferred if the technology matures sufficiently, particularly because it eliminates the multi-hit concern entirely.

Separate strip and LGAD layers (as in the original CL1a) is a conservative path guaranteed to work, at the cost of approximately doubling the wrapper material budget.

3.3.3 Material Budget

The physicist pressed for a realistic accounting of the full wrapper material budget, not just the sensor thickness. This exercise carried out by the AI revealed that the sensor itself is a minor contributor:

Table 3.5: Material budget for the outer silicon wrapper (single AC-LGAD layer), showing optimistic and conservative estimates.

Component	Optimistic x/X_0 (%)	Conservative x/X_0 (%)
LGAD sensor (50 μm Si)	0.053	0.053
Readout ASIC (75 μm Si)	0.080	0.107
Bump bonds / interconnect	0.005	0.015
Mechanical support	0.15	0.40
Power cables	0.05	0.10
Data cables	0.03	0.08
Cooling (air vs. pipes)	0.00	0.25
Total	0.37	1.0

The dominant contributions are the mechanical support structure (which cannot use the self-supporting curved shell approach at $R = 2000$ mm — the structure is too large and gravity matters) and potentially the cooling system (if air cooling proves insufficient for the LGAD power dissipation).

At ~ 0.4 – 1.0% X_0 , the outer wrapper is **10–30 times heavier per layer than the MAPS vertex layers**, even though the sensors are comparably thin. This is driven by the hybrid nature of LGADs (separate ASIC doubling the silicon material), the structural requirements at large radius, and the power delivery and cooling infrastructure.

This material sits directly in front of the ECAL, where every photon from $\pi^0 \rightarrow \gamma\gamma$ must traverse it. The photon conversion probability is ~ 0.3 – 0.8% per photon, which degrades ECAL performance. This consideration **strongly reinforces the case for a single AC-LGAD layer** rather than the two-layer strip + LGAD configuration of CL1a, which would roughly double the material. The physicist noted that the silicon wrapper realized in a detector will need multiple sensor layers compared with this conceptual layout to ensure robustness.

3.3.4 Start Time for Time-of-Flight

The time-of-flight measurement requires both a stop time (at the outer wrapper) and a start time (at the interaction point). The physicist raised the question of whether the nominal bunch crossing time is adequate as the start time, or whether the bunch length introduces a significant spread.

Bunch length and start time spread

The FCC-ee bunch length varies across the energy points, primarily due to the interplay of RF voltage, synchrotron radiation, and beamstrahlung:

Table 3.6: FCC-ee bunch lengths and corresponding start time spreads.

Energy point	σ_z (mm)	σ_t (ps)
Z pole (91 GeV)	3–4	7–9
WW threshold (160 GeV)	3–4	7–9
ZH (240 GeV)	4–5	9–12
$t\bar{t}$ (350 GeV)	5–6	12–14

The start time spread of ~ 10 ps is not negligibly smaller than the LGAD stop-time resolution of ~ 25 – 30 ps. Using the nominal bunch crossing time as the start time would degrade the effective TOF resolution especially at the $t\bar{t}$ threshold. Two approaches to determine the start on an event-by-event were examined.

Method 1: Common vertex time fit

Every track in the event originates from the same collision at a definite time t_0 . The stop time $t_{stop,i}$ is measured for N tracks, each with a known path length L_i and momentum p_i . Their masses are known for identified leptons and the remainder are assumed to be charged pions. These N independent estimates of t_0 can be combined in a fit to determine an overall vertex time. The vertex time fit is combined with bunch timing information for an improved start time, yielding $\sigma_{t_0} \approx 5$ ps for high-multiplicity hadronic events. Table 3.7 summarizes the situation.

Table 3.7: Start time determination: intrinsic collision time spread from bunch length compared with vertex time fit precision. In practice, their optimal combination is used.

Scenario	$\sigma_{t,\text{bunch}}$ (ps)	$\sigma_{t_0,\text{fit}}$ (ps)
Z hadronic (~ 12 tracks)	7–9	~ 7
$Z \rightarrow \tau\tau$ (~ 3 tracks)	7–9	~ 14
$t\bar{t}$ hadronic (~ 20 tracks)	12–14	~ 6

Method 2: Dedicated inner timing layer

A timing-capable sensor layer at small radius ($R \sim 80$ – 100 mm) could provide a per-track start time, eliminating the need for either bunch timing or a vertex time fit. However, the achievable timing resolution for a thin silicon sensor is ~ 25 ps at best, which is significantly worse than the ~ 7 – 9 ps start time already available from the bunch crossing timing. Adding the information from a dedicated inner timing layer does not improve the TOF measurement in any meaningful way. And the physicist noted the physics cost of adding material in the tracking volume (~ 0.1 – 0.3% X_0 for the sensor alone, plus services).

An alternative would be to incorporate timing capability directly into the MAPS vertex detector layers, avoiding a dedicated additional layer. However, this timing capability must significantly out-perform the expectations of AC-LGAD to be meaningful. Furthermore, timing in MAPS requires additional circuitry that increases power dissipation, which in turn increases service material for power delivery and cooling, and generates additional data volume — cascading consequences that undermine the air-cooled, ultra-thin vertex detector design. If future MAPS technology development were to provide adequate timing to improve on the timing from bunch crossing time without these penalties, it would be a welcome addition; at present, however, the cost is not justified by the benefit.

Assessment

The common vertex time fit is recommended as a complement to the bunch time determination. The two estimates are independent and their combination yields $\sigma_{t_0} \approx 5$ ps for high-multiplicity hadronic events. Whether the improvement in start time precision materially impacts π/K separation across the physics program is a question that deserves dedicated study.

3.3.5 Summary of Changes from CL1a

The outer silicon wrapper in CL2a differs from CL1a in two respects:

- i) **Single layer replacing two.** The separate strip + LGAD configuration of CL1a is replaced by a single AC-LGAD layer serving all three functions (position, z , timing). This roughly halves the material budget, from $\sim 1.5\text{--}2\%$ X_0 to $\sim 0.4\text{--}1.0\%$ X_0 , directly benefiting the ECAL performance behind it.
- ii) **Explicit start time strategy.** The common vertex time fit is adopted as the baseline method for TOF start time determination, with a dedicated inner timing layer identified as an upgrade path rather than a baseline requirement. This avoids adding material in the inner tracking volume while preserving the option for the future.

3.4 Electromagnetic Calorimeter

The electromagnetic calorimeter underwent the most dramatic revision of any subsystem in this study. The initial choice in CL1a — a liquid argon sampling calorimeter — was changed to a PbWO_4 crystal calorimeter through a sequence of arguments that illustrate how practical considerations can overturn choices that appear sound in the abstract. The discussion proceeded through several stages of physicist-AI discussion: liquid argon vs. liquid krypton, the cryostat dead material problem, the reassessment of crystals in the FCC-ee context, longitudinal segmentation and dual-readout, SiPM readout challenges, and finally the compatibility of crystals with particle flow reconstruction.

From Liquid Argon to Liquid Krypton

The physicist’s first challenge was straightforward: why liquid argon rather than liquid krypton? Everything else being equal, liquid krypton has higher density (2.41 vs. 1.40 g/cm³), higher dE/dx for minimum ionizing particles (~ 3.4 vs. ~ 2.1 MeV/cm), shorter radiation length (4.7 vs. 14.0 cm), and smaller Molière radius (4.7 vs. 7.2 cm). These translate directly into higher sampling fraction and hence better energy resolution for the same absorber geometry, as summarized in Table 3.8.

The principal argument against krypton is cost. Argon is $\sim 1\%$ of the atmosphere and essentially free; krypton is ~ 1 ppm and must be extracted and purified at significant expense ($\sim \$1000$ – 3000 /liter at research quantities, likely lower at industrial scale). For a full 4π sampling calorimeter requiring ~ 19 m³ of liquid krypton (estimated from a barrel geometry with $22 X_0$ depth at inner radius ~ 2.1 m), the krypton cost alone would be of order $\$20$ – 60 M.

Against this, krypton operates at a higher boiling point (120 K vs. 87 K for argon), making the cryogenics somewhat simpler. Purity requirements are similar for both liquids. The krypton is not consumed and can be recovered.

Table 3.8: Comparison of noble liquid electromagnetic calorimeter configurations and their approximate stochastic energy resolution terms.

Configuration	Stochastic term ($\%/\sqrt{\text{GeV}}$)
LAr + Pb (ATLAS-like)	10–12
LKr + Pb (similar geometry)	7–9
LKr + Pb (optimized)	5–7
LKr homogeneous (NA48-style)	3.5

On physics grounds, liquid krypton is clearly preferred over liquid argon. In response to the physicist’s challenge, the AI acknowledged that the initial choice of argon was insufficiently justified — inherited from the dominance of the ATLAS LAr calorimeter in the literature rather than optimized for FCC-ee. This was the first revision: if a noble liquid calorimeter were to be built, it should use krypton.

3.4.1 The Cryostat Problem

The physicist then posed two questions that proved decisive for the entire ECAL technology choice: how deep is the calorimeter in radiation lengths, and how thick is the cryostat?

Calorimeter depth. Electromagnetic shower containment for photons of order ($E \sim 50$ – 100 GeV) (as produced in Higgs decays at FCC-ee) requires 22–25 radiation lengths for 99% containment. For a sampling calorimeter with 2 mm Pb absorber and 4 mm LKr gaps, the effective radiation length of the sandwich is $X_0^{\text{eff}} \approx 13.6$ mm, giving a total depth of ~ 300 mm for $22 X_0$.

Cryostat thickness. Any noble liquid calorimeter requires a thermally insulated cryostat — a vacuum-insulated cold vessel that every particle must traverse before reaching the active

calorimeter. A realistic inner cryostat wall consists of a warm wall, vacuum insulation and a cold wall with the material budget estimated in Table 3.9. This is a substantial amount of dead material before the first active calorimeter layer.

Table 3.9: Cryostat inner wall material budget. The range reflects material choices (aluminum vs. stainless steel for the cold wall) and structural requirements. Wall thicknesses reflect realistic engineering for a barrel cryostat at $R \sim 2.1$ m, consistent with ATLAS LAr calorimeter experience.

Component	Material	x/X_0
Warm wall	3–5 mm Al	3–6%
Vacuum + MLI	25–30 mm	$\sim 0.6\%$
Cold wall	4–5 mm Al (or 2 mm SS)	4–6% (or 11%)
Total (Al cold wall)		$\sim 10\% X_0$
Total (SS cold wall)		$\sim 15\% X_0$

Impact on calorimeter performance. The cryostat dead material degrades performance through several mechanisms:

Stochastic term. The dead material introduces additional energy loss fluctuations that degrade the stochastic resolution term.⁴ For a cryostat of ~ 10 – $15\% X_0$, the bulk stochastic term degradation is modest. However, the more significant effects are the non-Gaussian tails and constant term contributions discussed below.

Non-Gaussian tails from photon conversions. Photons traversing ~ 10 – $15\% X_0$ of dead material have a conversion probability of ~ 8 – 11% . For the majority of photons that do not convert, the cryostat has little effect on the energy measurement. However, photons that do convert produce e^+e^- pairs that deposit some energy in the cryostat walls and enter the calorimeter with degraded spatial coherence. These events populate non-Gaussian tails of the energy response that are difficult to model and correct — a particular concern for the precision measurements at FCC-ee.

Constant term contribution. Non-uniformity of the cryostat thickness (at joints, welds, feedthroughs), energy-dependent shower initiation probability, and angular dependence of the effective thickness ($t/\sin\theta$) all contribute to the constant term at the ~ 0.2 – 0.5% level. For high-energy photons from Higgs decays ($E \sim 50$ – 120 GeV), where the stochastic term is already small, the constant term may dominate the resolution.

Position and angular resolution. Photons converting in the cryostat produce e^+e^- pairs that are spread by the magnetic field before reaching the calorimeter, degrading the photon position and pointing resolution — precisely the capabilities that the longitudinal segmentation of a noble liquid calorimeter is designed to provide.

⁴A useful rule of thumb for the impact of dead material on the stochastic energy resolution term is to add in quadrature a contribution $\Delta a \approx (0.05\text{--}0.08) \times \sqrt{x/X_0}$ ($\%/\sqrt{\text{GeV}}$), where x/X_0 is the dead material thickness in radiation lengths. For $x/X_0 = 0.1$ (i.e., $10\% X_0$), this gives $\Delta a \approx 2\%$, a modest degradation of the bulk stochastic term (from 7% to $\sim 7.3\%$ for LKr sampling). This parametrization is broadly consistent with the OPAL lead-glass test beam measurements reported in Fabjan and Gianotti²¹.

A presampler (a thin active layer before the calorimeter, as used in ATLAS) can partially correct the mean energy loss in the cryostat walls. For the cryostat thicknesses discussed here ($\sim 0.1\text{--}0.15 X_0$), presampler corrections can recover much of the average energy loss. However, it does not eliminate the event-by-event fluctuations that produce non-Gaussian tails, nor do they address the position resolution degradation from pair spreading in the magnetic field.

The decisive comparison. The cryostat dead material problem is fundamental to any noble liquid calorimeter and cannot be eliminated — a vacuum-insulated cold vessel is required by the physics of cryogenic containment. While a presampler can partially mitigate the average energy loss, the combination of non-Gaussian tails from photon conversions, constant term contributions from thickness variations, and position resolution degradation from pair spreading represents a significant and irreducible performance penalty.

The crystal calorimeter maintains near-intrinsic resolution because virtually no photons interact before reaching the active material. The noble liquid options suffer not only from the intrinsically worse stochastic term of a sampling calorimeter, but from the additional and irreducible penalties of the cryostat — penalties that are particularly damaging for the precision photon measurements central to the FCC-ee physics program.

This was the turning point in the ECAL discussion. The physicist’s questions about cryostat thickness exposed a fundamental limitation that the AI had not raised unprompted. The AI agreed that the argument was sound — if the comparison includes the cryostat (as any realistic design must), the noble liquid approach loses much of its appeal relative to crystals.

Table 3.10: Comparison of electromagnetic calorimeter technologies including the impact of material before the active calorimeter. The crystal calorimeter has only a thin mechanical support structure ($\sim 0.5\% X_0$) before the first active material. “Effective a ” is estimated using the rule of thumb $\Delta a \approx (0.05\text{--}0.08) \times \sqrt{x/X_0}$, added in quadrature to the intrinsic term; this captures only the bulk Gaussian stochastic degradation, not the non-Gaussian tails from photon conversions. “Additional constant term” refers to the contribution from upstream material only, not the total constant term of the calorimeter.

Technology	Intrinsic a (%/√GeV)	Dead material before active	Effective a (%/√GeV)	Conversion probability	Additional constant term
LKr sampling	7	10–15% X_0	7.3–7.4	8–11%	0.2–0.5%
LKr homogeneous	3.5	10–15% X_0	4.1–4.3	8–11%	0.2–0.5%
PbWO ₄ crystal	2.8	$\sim 0.5\% X_0$	~ 2.8	<0.5%	negligible

3.4.2 Crystal Calorimetry Reconsidered

With the cryostat problem established, the case for crystal calorimetry was reassessed. The AI’s initial dismissal of crystals had been based largely on the LHC experience, where radiation-induced transparency loss is the dominant challenge. The physicist pointed out that this experience is not applicable at FCC-ee.

Radiation damage: a non-issue at FCC-ee

The radiation environment at FCC-ee is orders of magnitude more benign than at the LHC:

- LHC: $\sim 1\text{--}10$ Gy/hour in the ECAL barrel, (varying with η), accumulating to tens to hundreds of kGy over the HL-LHC program.
- FCC-ee: \sim mGy/hour at most — essentially negligible for crystal damage.

The CMS PbWO₄ calorimeter experience — transparency loss, radiation-induced color centers, continuous laser monitoring, complex correction procedures, and the resulting contribution to the constant term — is driven entirely by the LHC radiation environment. At FCC-ee, crystals would maintain their initial optical quality throughout the entire 15-year program. This removes what has been the dominant systematic limitation of crystal calorimeters in the current era.

Calibration and monitoring. Calibration of a crystal calorimeter is generally more challenging than for a noble liquid calorimeter, where the response is determined primarily by the stable and uniform ionization properties of the liquid. In a crystal calorimeter, the full response chain — crystal light yield, light transport, photodetector gain, and electronics response — must be monitored and calibrated across $\sim 80,000$ channels over the lifetime of the experiment. This is typically addressed through a layered calibration strategy, combining hardware monitoring systems (light pulsers, charge injection, temperature sensors) for short-timescale stability with physics-based methods for absolute scale and intercalibration.

FCC-ee provides abundant clean electromagnetic samples at all running points — electrons and photons from well-understood processes at known energies — for establishing and maintaining the absolute energy scale. Compared to the LHC, the calibration environment is qualitatively more favorable: the physics samples are larger and cleaner, and the low-radiation environment means the time-dependent corrections that drive much of the calibration complexity at hadron colliders are far smaller.

Other advantages

Beyond energy resolution, crystals offer:

- **Compactness.** PbWO₄ achieves $22 X_0$ in only ~ 20 cm depth ($X_0 = 8.9$ mm), compared to ~ 37 cm total for a LKr sampling calorimeter including its cryostat walls. This allows for a more compact solenoidal coil.
- **Small Molière radius.** PbWO₄ has $R_M = 22$ mm, providing good transverse shower separation. While larger than tungsten's 9 mm (used in Si-W calorimeters), it is significantly smaller than the ~ 35 mm effective Molière radius of a Pb/LKr sampling calorimeter.
- **No cryogenic infrastructure.** Crystals operate at or near room temperature, eliminating the cryostat, cryogenics plant, liquid purity monitoring, and associated services. This simplifies the detector significantly.

- **Cost.** PbWO_4 crystals at $\sim\$200\text{--}500$ each for $\sim 80,000$ crystals give a crystal cost of $\sim\$16\text{M--}40\text{M}$ — comparable to the krypton cost alone for a noble liquid calorimeter, before accounting for the cryostat and cryogenics infrastructure.

Longitudinal Segmentation

A known limitation of crystal calorimeters relative to noble liquid or Si-W designs is the lack of longitudinal segmentation — a crystal is typically read out as a single unit, providing total energy but no information about the shower development profile. The physicist raised this as a concern following the shift to crystals. In response, the AI proposed a design that addresses this limitation through physical segmentation and multiple SiPM readout points.

Two-segment design

The crystal is physically divided into two segments:

- **Front segment:** $\sim 4\text{--}6 X_0$ ($\sim 35\text{--}55$ mm of PbWO_4), read out by a SiPM on the particle entrance face.
- **Back segment:** $\sim 16\text{--}18 X_0$ ($\sim 140\text{--}160$ mm), read out by SiPM(s) on the exit face.

The front SiPM sits on the entrance face of the front segment, with its active surface facing into the crystal. It collects primarily scintillation light from the front segment, with little Čerenkov contamination because Čerenkov light is emitted predominantly in the forward direction (away from this SiPM, deeper into the crystal). The front SiPM and its readout substrate add a small amount of material ($\sim 0.1\text{--}0.2\%$ X_0) on the entrance face, which must be included in the upstream material budget.

The ratio of front to total energy provides a measure of the longitudinal shower profile, enabling:

- Photon/hadron discrimination (electromagnetic showers deposit a large fraction in the front segment; hadronic showers penetrate deeper).
- π^0/γ discrimination (overlapping photons from high-energy π^0 decay produce a broader longitudinal profile than a single photon).
- Longitudinal leakage correction (deeper showers have more energy in the back segment and are more likely to leak).

The front segment depth of $\sim 4\text{--}6 X_0$ is a compromise: deep enough that electromagnetic showers have begun developing significantly, but shallow enough that the back segment contains the majority of the energy and shower maximum ($\sim 7\text{--}9 X_0$) falls near the segment boundary, maximizing the sensitivity of the front/back ratio to shower depth.

The physical interface between segments introduces a small dead layer (optical isolation film or air gap, $\sim 50\text{--}200 \mu\text{m}$ ($\sim 50\text{--}200 \mu\text{m}$, corresponding to $\sim 0.05\text{--}0.2\%$ X_0)). This is near shower maximum for medium-energy photons, where energy deposition per X_0 is highest, and contributes to the stochastic term. The optimization of segment interface material is an important engineering detail.

Dual-readout in the ECAL: considered and not adopted

Hadrons interacting in the ECAL produce showers whose electromagnetic fraction f_{em} fluctuates event by event, degrading the energy resolution. Dual-readout calorimetry — simultaneous measurement of Čerenkov and scintillation light — can correct for these fluctuations, since Čerenkov light is produced almost exclusively by the electromagnetic shower component. This technique has been studied and developed over some three decades^{22;23}, and represents a well-researched if not frequently adopted approach to improving hadronic energy resolution.

With a depth of ~ 20 cm, corresponding to approximately one nuclear interaction length ($\lambda_I \approx 20$ cm for PbWO_4), a significant fraction of hadron interactions are initiated in the ECAL, making dual-readout correction potentially valuable.

In the context of the segmented PbWO_4 design discussed above, dual readout could be implemented by adding a third SiPM to the back face, equipped with an optical filter that preferentially transmits Čerenkov light (UV/blue) while attenuating scintillation light (peaking at ~ 440 nm for PbWO_4). The C/S ratio would be extracted from the two back-face SiPMs (filtered and unfiltered), enabling an event-by-event correction of the measured energy for fluctuations in f_{em} in the back segment. Combined with the front SiPM — which is optically separate and provides longitudinal profile information — the three-SiPM configuration would yield both a shower depth profile and an f_{em} -corrected energy measurement.

The physicist identified two problems with this approach in the FCC-ee context.

First, for purely electromagnetic showers — the ECAL’s primary mission — the dual-readout technique provides no additional information. In an electromagnetic shower, $f_{em} = 1$ by definition: there are no hadronic fluctuations to correct for. Both the Čerenkov and scintillation signals are proportional to the total deposited energy, with a fixed ratio that carries no event-by-event discriminating power. The Čerenkov measurement is therefore redundant with the scintillation measurement for electromagnetic showers — it measures the same quantity with fewer photons.

Meanwhile, implementing the filtered readout carries a direct cost: the optical filter attenuates scintillation photons, reducing the light available for the primary energy measurement. This cost is compounded by the poor spectral separation between Čerenkov light and PbWO_4 scintillation — they overlap significantly in the blue region, making clean filtering impractical without substantial loss of scintillation signal.

Second, while the dual-readout correction would genuinely help for hadrons interacting in the ECAL, the benefit is limited: the ECAL sees only the beginning of hadronic showers, with the bulk of the hadronic energy measured in the HCAL behind. Improving the ECAL’s hadronic measurement at the cost of degrading its electromagnetic measurement is trading performance on the primary mission for a partial gain on a secondary one.

A quantitative estimate of the cost: with the back face shared between two SiPMs (one filtered, one unfiltered), the total detected photoelectrons drop by roughly a third, degrading the photostatistical contribution to the energy resolution by $\sim 20\%$.

The dual-readout option in the ECAL is not adopted for this design. The recommended configuration is two SiPMs (front and back) without filtering, to provide longitudinal shower profile information and the best electromagnetic energy resolution. This does not preclude dual-readout techniques in the HCAL, where the cost-benefit trade-off is fundamentally different.

3.4.3 SiPM Readout and Dynamic Range

The discussion then turned to a practical challenge of crystal calorimetry with SiPM readout at FCC-ee energies: the dynamic range required to measure electromagnetic showers from ~ 100 MeV to ~ 150 GeV without saturation.

Maximum photon count

For PbWO_4 at room temperature (scintillation yield ~ 200 photons/MeV)⁵, the maximum energy deposit in a single crystal (~ 120 GeV, accounting for shower sharing between crystals) produces:

$$N_{\text{scint}} = 200 \times 120,000 = 24 \times 10^6 \text{ photons} \quad (3.4)$$

With $\sim 15\%$ light collection efficiency at the back face and $\sim 25\text{--}40\%$ SiPM photon detection efficiency, the detected photoelectrons of an idealized back SiPM are:

$$N_{\text{pe}} \approx 24 \times 10^6 \times 0.15 \times 0.3 \approx 10^6 \quad (3.5)$$

The scintillation light is emitted with three decay components: $\sim 39\%$ with $\tau \approx 5$ ns, $\sim 60\%$ with $\tau \approx 15$ ns, and $\sim 1\%$ with $\tau \approx 100$ ns. Of the $\sim 10^6$ total photoelectrons at maximum energy, the peak arrival rate is $\sim 10^5$ per nanosecond, with the majority delivered within ~ 30 ns.

Internal reflections within the high-refractive-index crystal ($n \approx 2.3$) cause extensive light mixing as photons bounce multiple times off the reflective wrapping before reaching the back face. As a result, the photon density at the SiPM surface is approximately uniform regardless of the transverse shower profile — there is no localized hot spot at the shower core. The saturation assessment can therefore use the average photon density across the SiPM face rather than the peak energy deposition density within the crystal.

SiPM saturation

An SiPM consists of an array of microcells operating in Geiger mode. Each cell fires once and recovers with a time constant $\tau_{\text{recovery}} \sim 10\text{--}50$ ns. When many photons arrive within the recovery time, some cells may not have recovered from an earlier arriving photon. This is a saturation effect that can be corrected on average; however, event-to-event fluctuations lead to poorer resolution. The average number of cells expected to fire is:

$$N_{\text{fired}} = N_{\text{cells}} \times \left(1 - \exp\left(-\frac{N_{\text{pe}}}{N_{\text{cells}}}\right) \right) \quad (3.6)$$

For 1% nonlinearity at maximum signal, one needs $N_{\text{cells}} > N_{\text{pe,fast}}/0.02 \approx 30 \times 10^6$ cells⁶. Current SiPM technology at $10 \mu\text{m}$ cell pitch provides $\sim 10,000$ cells/ mm^2 ; covering a

⁵Published values for PbWO_4 light yield range from ~ 100 to ~ 200 photons/MeV at room temperature, depending on crystal quality, doping, and the precise definition of “room temperature” (the yield has a steep temperature coefficient of $\sim -2\%/^\circ\text{C}$). We use 200 photons/MeV throughout as a representative value; qualitative conclusions are not sensitive to this choice.

⁶For small saturation, expanding Eq. 3.6 to second order gives $N_{\text{fired}} \approx N_{\text{pe}}(1 - N_{\text{pe}}/(2N_{\text{cells}}))$, where the second term $N_{\text{pe}}/(2N_{\text{cells}})$ is the fractional nonlinearity. Requiring this to be less than 1% gives $N_{\text{cells}} > N_{\text{pe}}/0.02$. With $N_{\text{pe,fast}} \approx 600,000$, this requires ~ 30 million cells.

$20 \times 20 \text{ mm}^2$ crystal face ($\sim 320 \text{ mm}^2$ active area) gives only ~ 3.2 million cells — roughly an order of magnitude too few.

Fill factor as sampling fraction

The physicist reframed the saturation problem in illuminating terms: pushing to smaller cell pitch to increase cell count necessarily reduces the fill factor, since each cell has a fixed-width border region ($\sim 2\text{--}3 \mu\text{m}$) for the quenching resistor and guard ring. At $5 \mu\text{m}$ pitch, the fill factor drops to $\sim 16\%$.

This is another form of “sampling fraction” — whether photons are lost in absorber plates (as in a conventional sampling calorimeter) or in dead area between SiPM cells, the physics impact is identical. The mean can be corrected, but the fluctuation in the number of detected photons is irreducibly larger. The stochastic resolution degrades as $1/\sqrt{\text{fill factor}}$.

Among common scintillating crystals, PbWO_4 is the only one for which the SiPM saturation challenge is even manageable. Higher-yield crystals such as LYSO ($\sim 33,000$ photons/MeV), BGO ($\sim 9,000$ photons/MeV), or CsI(Tl) ($\sim 54,000$ photons/MeV) would produce $100\text{--}500\times$ more light, making SiPM saturation catastrophic at any energy above ~ 1 GeV regardless of cell pitch or fill factor. The low light yield of PbWO_4 , usually considered a disadvantage, is in this context essential.

Nonlinearity as a separate effect

Even with 100% fill factor, the Geiger-mode saturation compresses the response. The correction $N_{\text{pe}} = -N_{\text{cells}} \ln(1 - N_{\text{fired}}/N_{\text{cells}})$ amplifies the statistical variance:

$$\sigma_{\text{corrected}}^2 = \sigma_{\text{raw}}^2 \times \left(\frac{N_{\text{cells}}}{N_{\text{cells}} - N_{\text{fired}}} \right)^2 \quad (3.7)$$

At 20% saturation ($N_{\text{fired}}/N_{\text{cells}} = 0.2$), the variance amplification is $(1/0.8)^2 = 1.56$, degrading the effective resolution by $\sim 25\%$. At 50% saturation, the amplification is $4\times$, doubling the resolution. These are separate from and in addition to fill factor effects.

These estimates treat the scintillation light as arriving instantaneously. In practice, the light is spread over the scintillation decay profile (with components at $\sim 5, 15,$ and 100 ns for PbWO_4), and cells that fire early in the pulse may recover in time to detect later-arriving photons. This partial recovery effectively increases the dynamic range beyond the instantaneous estimate. However, the recovery process is stochastic: which cells recover and re-fire fluctuates event by event, introducing an additional variance that cannot be removed by correcting the mean response. The estimates above are therefore indicative of the scale of the saturation challenge rather than precise predictions; quantifying the net effect of partial recovery and its associated fluctuations would require detailed simulation of the interplay between the scintillation time profile and cell recovery characteristics.

Digital SiPM

A digital SiPMs (dSiPMs) is defined by the integration of per-cell digital electronics directly on the same substrate as the photo-sensing cells. This electronics usually integrates active

quenching and recharge circuitry into each cell, reducing the recovery time from $\sim 10\text{--}50$ ns (passive) to $\sim 1\text{--}5$ ns. Cells can therefore fire multiple times during the scintillation pulse, increasing the effective dynamic range. The electronics can have additional logic to process individual micro-cell signals to produce a custom output signal.

The benefit is real but bounded. The electromagnetic shower deposits all its energy within ~ 1 ns, and the scintillation photon rate is highest immediately afterward — precisely when cells have not yet had time to recover. During the first recharge cycle, the detector response is identical to that of an analog SiPM. The improvement from active recharge grows as the scintillation pulse decays and the photon arrival rate drops below the cell recovery rate. Active recharge therefore mitigates saturation — substantially for the later portion of the scintillation pulse, but not for the initial burst⁷.

The power implications depend critically on what functionality is implemented per cell. If the on-sensor circuitry is limited to active quenching, recharge, masking of noisy cells, and counting of cell firings within a time window, the additional power dissipation is negligible. If per-cell timing information is desired, the power requirements increase substantially and depend on implementation details that are not yet settled: the timing resolution, the number of cells sharing a timing circuit, the occupancy, and the CMOS technology node. Subject matter experts consulted during this study were unable to provide even order-of-magnitude power estimates without a specific circuit design.

For the baseline calorimetric measurement (total energy from photon counting), per-cell timing is not required. A counting-only dSiPM with active recharge offers lower system power than an analog SiPM (which requires a front-end amplifier and ADC per channel), while providing meaningful improvement in dynamic range through cell recovery during the scintillation pulse.

Preferred approach: digital SiPM in counting mode

The key R&D items are the development and test beam validation of a counting-mode dSiPM matched to PbWO_4 scintillation properties: cell pitch, recharge time, counter depth, and integration window must be optimized for the FCC-ee energy range. This work should be performed before committing to the readout technology.

Fallback: analog SiPM with saturation correction

If counting-mode dSiPM proves impractical or insufficiently mature on the FCC-ee timescale, the fallback is a conventional analog SiPM. The analog sensor draws essentially no quiescent power, though the per-channel front-end electronics (amplifier and digitizer) located behind the crystal add significant power — more than the counting-mode dSiPM alternative.

The saturation response of an analog SiPM is a known function of $N_{\text{pe}}/N_{\text{cells}}$ (Eq. 3.6), and can be corrected using the measured signal and a calibration of the saturation curve. This corrects the mean response; the residual resolution degradation from variance amplification (Section 3.4.3) remains, but is a calculable and bounded effect.

⁷While scintillation light is governed by the decay time constants of the fluor, which can range from few nsec to few 100s of nsec, Čerenkov light is prompt and does not benefit from active recharge

It has been suggested that digitizing the scintillation waveform and exploiting its time structure could improve the saturation correction beyond the simple calibration approach. However, with $\sim 10^5$ photoelectrons per nanosecond at the highest energies, the practical benefit of waveform-based correction over simple calibration curve correction remains to be demonstrated.

A test beam validation analogous to that described for dSiPM — measuring energy resolution across the FCC-ee energy range with saturation correction applied — would establish the achievable performance of the analog approach.

Operating temperature

PbWO₄ scintillation yield increases significantly at lower temperatures: roughly $\times 1.5$ at 0°C and $\times 2.5$ at -25°C , relative to room temperature. CMS operates at 18°C as a compromise.

The physicist noted an ironic trade-off: lower temperature increases the light yield (improving photostatistics and the stochastic term) but also increases the number of photons arriving at the SiPM, *worsening* the saturation problem. Additionally, the temperature coefficient of PbWO₄ light yield is steep ($\sim -2\%/^\circ\text{C}$ near room temperature), requiring tight thermal control ($\sim 0.05^\circ\text{C}$ for 0.1% energy stability).

The optimal operating temperature balances photostatistics against saturation and thermal stability demands. A moderate temperature of $\sim 10\text{--}15^\circ\text{C}$ may be optimal, but this requires dedicated study with the actual SiPM readout configuration.

3.4.4 Crystal ECAL and Particle Flow Compatibility

A concern with the crystal ECAL choice is its compatibility with particle flow reconstruction, which has been the dominant paradigm for e^+e^- Higgs factory detectors. The AI initially expressed skepticism about this compatibility, but the subsequent discussion substantially revised this assessment.

The initial concern

The worry was that crystal granularity ($20\times 20\text{ mm}^2$ crystal face) is much coarser than the Si-W pads ($5\times 5\text{ mm}^2$) for which particle flow algorithms were optimized. With only ~ 1 crystal across a Molière radius (22 mm), compared to ~ 2 pads across the tungsten Molière radius (9 mm), the ability to resolve nearby showers from different particles appeared significantly compromised.

Furthermore, the crystal ECAL provides only two longitudinal segments (front and back), compared to the ~ 30 longitudinal layers available in a Si-W ECAL. The 3D shower imaging capability seemed fundamentally different.

The reassessment

Closer examination revealed that the concern, while not unfounded, was overstated in some respects and genuine in others.

What matters in the PFA context. Particle flow jet energy reconstruction uses tracker momentum for charged particles, ECAL energy for photons, and HCAL energy for

remaining neutral hadrons. The ECAL’s role is to provide the best possible measurement of the photon component, which constitutes $\sim 25\%$ of jet energy. Any ECAL deep enough to contain electromagnetic showers fulfills this role; the crystal and Si-W options are equivalent in this regard. The relevant question is how the crystal’s superior photon energy resolution trades off against Si-W’s finer granularity and longitudinal segmentation for resolving nearby clusters and for identifying charged particle deposits.

Granularity relative to shower width. The relevant comparison is not raw cell size but cell size relative to shower width. Si-W has ~ 1.8 cells per Molière radius; the crystal has ~ 1.1 . The difference is real but less dramatic than the raw 5 mm vs. 20 mm ratio suggests, because the shower widths scale differently in the two materials.

Position resolution through energy sharing. In a crystal calorimeter, the position of an electromagnetic shower is reconstructed from the energy sharing among neighboring crystals. The position resolution is approximately:

$$\sigma_{\text{pos}} \sim \frac{R_M}{\sqrt{E/\text{GeV}}} \sim \frac{22}{\sqrt{10}} \approx 7 \text{ mm for a 10 GeV photon} \quad (3.8)$$

This is comparable to the Si-W pad size, showing that the crystal ECAL achieves good single-shower position resolution through energy sharing even though its cells are large. However, position resolution for a single isolated shower is distinct from the ability to resolve two nearby overlapping showers, which is the more relevant capability for particle flow. For two-shower separation, the cell size relative to the shower width is the more directly relevant quantity, where Si-W retains an advantage.

Close pairs are rare. At Z-pole jet energies (~ 45 GeV), the typical particle separation at the ECAL face is ~ 200 mm — roughly 9 Molière radii, easily resolved in any calorimeter. Only a few percent of photon-hadron pairs are close enough for granularity to matter, and the magnetic field bends charged particles away from neutrals, further reducing the overlap.

Photon energy resolution directly improves jets. Photons constitute $\sim 25\%$ of jet energy. The crystal’s substantially better photon energy resolution directly improves this component. For a 10 GeV photon, the crystal gives $\sigma_E \sim 95$ MeV vs. ~ 350 MeV for Si-W — a significant improvement that partially compensates any loss from coarser granularity.

Longitudinal segmentation: an honest limitation. The two-segment crystal design provides far less longitudinal information than the ~ 30 layers of a Si-W ECAL. This is a genuine limitation for particle flow reconstruction. In PFA, the ECAL measures not only photons but also receives energy deposits from all charged particles — electrons, muons, and charged hadrons — whose contributions must be identified and subtracted so that the remaining energy accurately represents the neutral (photon) component. Fine longitudinal and transverse segmentation aids this subtraction by providing geometric discrimination between a tracked particle’s deposit and any overlapping neutral energy. For example, a muon traversing a crystal deposits MIP energy that cannot easily be disentangled from photon energy in the same crystal; in Si-W, the muon’s narrow trail across ~ 30 small pads is geometrically distinct from a photon shower. This is a genuine advantage of Si-W that the crystal option cannot match with only two longitudinal segments.

The role of the magnetic field

The particle flow jet energy resolution numbers commonly quoted in the literature (e.g., $\sim 3\text{--}4\%$ at 45 GeV from ILD studies) assumed a 3.5 T magnetic field and Si-W ECAL. These numbers cannot be directly applied to a detector with 2 T field and crystal ECAL.

The magnetic field strength — which determines how effectively charged particles are separated from neutrals at the calorimeter face — is a significant driver of PFA performance. At the 2 T field adopted for this design, the charged-neutral separation is reduced compared to the 3.5 T assumed in ILD studies, and this affects PFA performance regardless of the ECAL technology choice. The ECAL technology and the magnetic field strength both contribute to PFA performance, and the two effects should not be conflated when comparing detector concepts.

Revised assessment

The crystal ECAL’s compatibility with particle flow reconstruction is a mixed picture:

- **Advantages:** substantially better photon energy resolution, improving the $\sim 25\%$ photon component of jet energy; adequate single-shower position resolution through energy sharing; sufficient granularity for the majority of particle separations at Z-pole jet energies.
- **Limitations:** coarser transverse granularity reduces two-shower separation capability for the small fraction of close pairs; far less longitudinal segmentation limits the ability to geometrically identify and subtract charged particle deposits from overlapping neutral energy.

The crystal ECAL is not optimal for particle flow in the same way that Si-W was specifically designed for it. The longitudinal segmentation limitation, in particular, is genuine and cannot be fully mitigated by the two-segment design. However, the crystal’s advantages in photon energy resolution, absence of cryostat dead material, and operational simplicity are significant, and the granularity concern is less severe than the raw cell size comparison suggests. A definitive comparison would require full simulation of jet reconstruction with both ECAL options in the same detector geometry and magnetic field — a study that has not yet been performed and that this report recommends.

3.4.5 Summary of ECAL Evolution

The electromagnetic calorimeter choice evolved through several stages of physicist-AI discussion:

- i) **LAr** \rightarrow **LKr**: Liquid krypton preferred over liquid argon on physics grounds (higher sampling fraction, better resolution, smaller Molière radius), with cost as the main counterargument.
- ii) **Noble liquid** \rightarrow **crystal**: The cryostat dead material ($\sim 10\text{--}15\% X_0$) degrades the noble liquid calorimeter performance through multiple mechanisms: non-Gaussian tails from photon conversions ($\sim 8\text{--}11\%$ conversion probability), constant term contributions

from cryostat non-uniformities, and position resolution degradation from pair spreading in the magnetic field. Crystals achieve $\sim 3\%/\sqrt{E}$ with negligible dead material upstream. The benign radiation environment at FCC-ee removes the historical weakness of crystals, and the abundant physics samples at all running points provide powerful calibration capability.

- iii) **Longitudinal segmentation:** A two-segment crystal design (front $\sim 4\text{--}6 X_0$, back $\sim 16\text{--}18 X_0$) with front and back SiPM readout providing longitudinal shower profile information to partially address a known limitation of crystal calorimeters.
- iv) **Dual readout in ECAL not adopted:** While the technique would genuinely help for hadrons interacting in the ECAL ($\sim 1 \lambda_I$ depth), for electromagnetic showers the separate Čerenkov measurement is redundant ($f_{em} = 1$ always) and the optical filter degrades the scintillation light collection. The cost to the primary EM measurement outweighs the secondary hadronic benefit.
- v) **Readout approach:** Counting-mode digital SiPM with active quenching and recharge preferred over analog SiPM, offering lower system power and improved dynamic range through cell recovery during the scintillation pulse. Analog SiPM with saturation curve correction is maintained as a fallback. Both options require test beam validation.
- vi) **PFA compatibility:** The crystal ECAL is not optimal for particle flow in the way SiW was designed for it — the coarser granularity and limited longitudinal segmentation are genuine limitations for identifying and subtracting charged particle energy deposits. However, the substantially better photon energy resolution partially compensates, and the granularity concern is less severe than the raw cell size comparison suggests. A full simulation comparison is recommended.

This sequence illustrates a recurring theme of this study: practical considerations (cryostat dead material, radiation environment, power management) can decisively shift the technology choice away from what appears optimal in the abstract.

3.5 Solenoid

The solenoid underwent two significant changes from CL1a, both emerging from the physicist’s questions about cost, accelerator coupling, and the magnetic flux return path. First, the field strength evolved from a fixed 2 T to a variable 1.5–3 T range matched to the beam energy at each operating point. Second, the placement moved from outside the HCAL to between the ECAL and HCAL, with significant consequences for the overall detector layout. The field strength is discussed in this subsection; the placement is discussed in Section 3.5.2.

3.5.1 Field Strength and Accelerator Coupling

The beam-solenoid interaction

The solenoid field at the interaction point couples to the circulating beams, and this coupling must be compensated by anti-solenoid coils or corrector magnets in the interaction region.

The compensation becomes more demanding at lower beam energies. FCC-ee accelerator studies indicate that solenoid fields above ~ 2 T become increasingly difficult to compensate at Z-pole energies ($E_{\text{beam}} = 45.6$ GeV), while fields up to 3 T are manageable at the $t\bar{t}$ threshold ($E_{\text{beam}} = 175$ GeV).

Variable field strategy

This accelerator constraint aligns naturally with the physics requirements: lower-energy running (Z pole) involves softer jets where particle flow works well even at moderate field, while higher-energy running ($t\bar{t}$) produces more collimated jets that benefit most from strong magnetic separation. The proposed operating scheme is:

Table 3.11: Variable solenoid field strategy across the FCC-ee energy points.

Energy point	E_{beam} (GeV)	B (T)	Rationale
Z pole	45.6	1.5–2.0	Accelerator compatibility most demanding
WW threshold	80	2.0–2.5	Relaxed accelerator constraint
ZH	120	2.5–3.0	Best momentum resolution for Higgs recoil
$t\bar{t}$	175	3.0	Maximum field; highest-energy jets

The solenoid is designed for the maximum field of 3 T but operated at reduced current for lower-energy running. This is technically straightforward — a superconducting solenoid designed for 3 T operates safely at any lower field. The design choice to support 3 T rather than a fixed 2 T carries costs: a thicker coil (more conductor and structural material for the higher magnetic pressure, which scales as B^2) increases both the construction cost and the material budget before the HCAL. These are meaningful but justified by the physics benefit of matching the field to the beam energy across the full FCC-ee program.

The implications for other subsystems are manageable:

- Track reconstruction, particle flow clustering, and calibrations must be validated across the 1.5–3 T range.
- The drift chamber is the most sensitive subsystem to field variations: the Lorentz angle affects drift paths over the \sim cm-scale drift distances, curving trajectories that are straight in the absence of a magnetic field. Cell geometry can be designed to optimize drift paths for a given field strength and gas mixture, but this optimization is valid for only one operating point. Operating over a 1.5–3 T range requires a cell design and gas choice that perform adequately across the full range, accepting some compromise at each individual field setting. This is a known and understood challenge with established mitigation strategies.
- The track momentum resolution scales as $1/B$, so Z-pole running at 2 T has 50% worse momentum resolution than 3 T operation. This is acceptable because the Z pole physics does not require the extreme momentum resolution needed for the Higgs recoil measurement at 240 GeV.

3.5.2 Solenoid Placement: Inside the HCAL

CL1a placed the solenoid outside the HCAL to avoid introducing dead material between the ECAL and HCAL. The physicist challenged this with a series of arguments about cost, magnetic flux return, and the interplay with other subsystems.

Cost scaling

The cost of a superconducting solenoid scales steeply with bore radius. The key quantities — conductor volume, stored energy, and return yoke mass — all scale as R^2L or steeper. For the two placement options:

Table 3.12: Solenoid parameters for the two placement options, assuming 3 T design field.

Parameter	Inside HCAL ($R = 2.5$ m)	Outside HCAL ($R = 4$ m)
Bore radius (m)	2.5	4.0
Length (m)	5–6	7–9
Flux Φ (Wb)	59	151
Stored energy ratio	1	~ 3.7
Yoke mass ratio	1	~ 3.7
Approximate cost (MCHF)	25–35	80–120

The larger solenoid costs roughly $\sim 4\times$ **more**, following the $(R_{\text{out}}/R_{\text{in}})^3 \approx (4/2.5)^3 \approx 4$ scaling identified by the physicist. The cost difference of ~ 50 – 90 M CHF is a substantial fraction of the total detector budget.

The HCAL as flux return

The physicist made a further observation that strengthens the case for the inside placement: if the HCAL uses steel absorber plates (as in the scintillator-steel tile design), this steel can carry a substantial fraction of the magnetic return flux.

For a barrel HCAL with ~ 40 layers of 20 mm steel plates spanning from $R \approx 2.5$ m to $R \approx 4.2$ m, the total steel cross-sectional area available for flux return is of order 15–20 m². At an average field near saturation ($B_{\text{sat}} \approx 1.6$ T), the HCAL steel can carry a substantial fraction of the total 59 Wb return flux.

The remainder requires an additional return yoke outside the HCAL, but this is significantly thinner than would be needed without the HCAL contribution. Compare this to the solenoid-outside case, where the full 151 Wb requires a massive dedicated return yoke at $R \approx 4.5$ – 6 m, adding several thousand tonnes of iron.

The physicist summarized the argument concisely: with the solenoid inside, every tonne of steel serves multiple purposes — calorimeter absorber, flux return, and muon filter. With the solenoid outside, a massive dedicated flux return is needed whose thickness is driven by magnetic requirements that may over- or under-shoot the muon physics needs.

The cost of coil dead material

The price paid for the inside placement is dead material between the ECAL and HCAL. The solenoid coil — superconducting cable plus aluminum stabilizer and structural support — contributes:

Table 3.13: Solenoid coil material budget for different design aggressiveness levels, at 3 T design field and $R = 2.5$ m.

Design approach	Thickness (mm)	x/λ_I
Conventional (CMS-like)	250	0.64
Aggressive	150	0.38
Very aggressive (HTS)	100	0.26

The target is $\lesssim 150$ mm, giving $\sim 0.4 \lambda_I$ of dead material. The structural feasibility at 3 T requires careful engineering: the magnetic pressure is ~ 3.6 MPa, giving hoop stress of ~ 60 MPa in a 150 mm wall at $R = 2.5$ m. This is within the capability of high-strength aluminum alloy but leaves modest safety margins. At 2 T (Z-pole operation), the stress drops to ~ 27 MPa, well within comfortable limits.

Impact on hadronic energy measurement

The coil dead material of $\sim 0.4 \lambda_I$ means that $\sim 33\%$ of hadrons entering the HCAL interact in the coil first, with the resulting energy deposit unmeasured. This degrades the hadronic energy resolution, primarily for neutral hadrons whose energy depends entirely on the calorimetric measurement.

However, in the particle flow framework, charged hadron energies are measured by the tracker and photon energies by the ECAL. The neutral hadron component — which is what the coil dead material primarily affects — constitutes only $\sim 10\text{--}15\%$ of jet energy. Furthermore, the particle flow confusion term dominates jet energy resolution over the HCAL intrinsic resolution at all FCC-ee energies (Section 3.6).

The coil dead material degrades the neutral hadron energy resolution, contributing modestly to the jet energy resolution in quadrature — a small effect compared to the $\sim 2\text{--}3\%$ confusion term that dominates.

Interplay with the HCAL absorber material

If the HCAL steel serves as flux return, the absorber **must be ferromagnetic** — low-carbon steel or iron. This rules out non-magnetic absorber materials such as brass (used in the CMS HCAL) or copper. Standard low-carbon structural steel (e.g., S235) serves both purposes well, with saturation magnetization of $\sim 1.6\text{--}1.8$ T and adequate mechanical properties for calorimeter construction.

The steel is magnetized at ~ 1.6 T in operation. Charged shower particles traversing a 20 mm steel plate experience both multiple Coulomb scattering (RMS lateral displacement ~ 1 mm for a typical 200 MeV shower particle, scaling as $1/p$) and magnetic bending (~ 0.5 mm at the same momentum). Multiple scattering is the larger effect by roughly a factor of two,

and both are small compared to the characteristic transverse scale of hadronic showers (~ 10 – 20 cm). Neither materially affects the calorimeter energy response.

3.5.3 Field Uniformity

The placement of ferromagnetic steel (the HCAL) immediately outside the solenoid coil changes the magnetic boundary conditions and creates some field non-uniformity in the tracking volume.

The physicist noted that this is not a practical concern. The tracking volume extends to $R \approx 2000$ mm, while the solenoid coil is at $R \approx 2500$ mm, with the crystal ECAL (non-magnetic PbWO_4) providing ~ 500 mm of separation. Field perturbations from the magnetized HCAL steel fall off with distance and are expected to be small at the outer tracker radius. However, even substantially larger perturbations would not be problematic: every major collider detector maps its magnetic field to $\sim 10^{-4}$ precision before operation, and track reconstruction integrates the equations of motion through the measured 3D field map rather than assuming a uniform field. What matters is not uniformity but *knowledge* of the field at every point. A 2 T field with 1% non-uniformity mapped to 10^{-4} is far more useful for tracking than a perfectly uniform field known only to 1%.

Furthermore, at FCC-ee, abundant $Z \rightarrow \mu^+\mu^-$ events provide continuous in-situ field calibration through the known Z mass constraint.

Field non-uniformity is therefore not a factor in the solenoid placement decision.

3.5.4 Summary of Solenoid Evolution

The solenoid design evolved in two important ways from CL1a:

- i) **Fixed 2 T \rightarrow variable 1.5–3 T.** The field strength is matched to the beam energy at each operating point, naturally aligning the physics needs (higher field benefits higher-energy jets) with the accelerator constraints (higher beam energy tolerates more solenoid field). The solenoid is designed for 3 T maximum but operated at reduced current for lower-energy running.
- ii) **Outside HCAL \rightarrow inside HCAL.** The inside placement reduces the solenoid cost by $\sim 4\times$, enables the HCAL steel to serve double duty as flux return (substantially reducing the dedicated return yoke mass and cost), and allows the muon absorber to be optimized for physics rather than dictated by magnetic requirements. The cost is $\sim 0.4 \lambda_I$ of dead material between ECAL and HCAL, which has a modest impact on jet energy resolution: in the particle flow framework, the coil material primarily affects the neutral hadron component (~ 10 – 15% of jet energy), and the confusion term dominates the jet energy resolution at all FCC-ee energies.

The solenoid discussion illustrates how cost and engineering considerations can shift a design choice that initially appears to be driven by physics alone. The “obvious” choice of placing the solenoid outside the HCAL for uninterrupted calorimetry does not survive scrutiny of the full cost-performance trade-off.

3.6 Hadron Calorimeter

3.6.1 The Problem and the Particle Flow Solution

The standalone problem

Hadronic energy resolution is fundamentally limited by event-by-event fluctuations in the electromagnetic fraction f_{em} of hadronic showers. In each nuclear interaction within the shower, a fraction of the energy goes into π^0 production, while the remainder goes into charged hadron cascades, nuclear breakup, and binding energy losses. The ratio of electromagnetic to hadronic response (e/h) is typically 1.2–1.5 for non-compensating calorimeters, so fluctuations in f_{em} translate directly into energy resolution degradation and non-Gaussian response tails.

The particle flow approach to jet energy

The physicist pointed out that for jet energy measurement, the particle flow algorithm (PFA) largely avoids this problem by using the best-suited detector component for each particle type:

- Charged particles ($\sim 65\%$ of jet energy) are measured by the tracker with excellent resolution ($\sigma/E \sim 10^{-3}$).
- Photons and π^0 s ($\sim 25\%$) are measured by the ECAL.
- Only neutral hadrons ($\sim 10\%$) genuinely rely on the HCAL.

Since only $\sim 10\%$ of jet energy depends on the HCAL measurement, even moderate intrinsic HCAL resolution has limited impact on overall jet energy resolution. On the other hand, the HCAL in a particle flow detector has the additional role to **identify and locate** neutral hadron showers separately from charged hadron showers, enabling correct energy assignment.

A known limitation of the PFA approach is that performance degrades at higher jet energies, as showers become more collimated and the confusion between charged and neutral deposits increases. Published studies show jet resolution degrading from $\sim 3\%$ at 45 GeV to $\sim 5\text{--}6\%$ at 175 GeV, though these specific numbers assume a 3.5 T field and Si-W ECAL and are not directly applicable to CL2a.

This framing applies to any detector with a deep ECAL that contains electromagnetic showers. The hadronic showers within the HCAL still contain significant electromagnetic content from π^0 production in the cascade; the PFA simplification is that *incoming* photons have already been measured by the ECAL.

Two approaches to the HCAL

The two HCAL technologies under consideration address the remaining task through fundamentally different strategies: the scintillator-steel tile calorimeter emphasizes high granularity for pattern recognition and shower separation, while the dual-readout fiber calorimeter attacks the f_{em} fluctuation problem directly to achieve superior standalone hadron resolution.

3.6.2 Scintillator-Steel Tile Calorimeter

Design

The particle flow approach drives the tile HCAL design toward high granularity for pattern recognition and shower separation:

- Steel absorber plates (~ 20 mm) interleaved with scintillator tiles (~ 3 mm thick, $\sim 30 \times 30$ mm² area).
- Each tile read out by an individual SiPM.
- ~ 50 layers for $\sim 6 \lambda_I$ depth.
- Total channel count: ~ 8 million for a full 4π HCAL.

Strengths

- **Proven particle flow performance.** Extensively simulated for ILC (ILD, SiD) and FCC-ee (CLD), with jet energy resolution of ~ 3 – 4% demonstrated at Z-pole jet energies in full simulation with PandoraPFA reconstruction.
- **3D shower imaging.** The fine granularity (30×30 mm² tiles in ~ 50 longitudinal layers) provides detailed shower topology. This is valuable beyond jet energy measurement: τ reconstruction, missing energy vetoes, muon identification through minimum-ionizing signatures, and software compensation using shower shape information.
- **Mature technology.** The CALICE collaboration has built and tested large prototypes in beam tests²⁴. SiPM mass production is established. Tile production and assembly have been industrialized.
- **Straightforward calibration.** Each tile/SiPM combination is calibrated with minimum ionizing particles (muons traversing the HCAL). The MIP calibration is robust, well-understood, and transfers reliably from test beam to in-situ operation.
- **Compatibility with magnetized steel.** With the solenoid inside the HCAL (Section 3.5.2), the steel absorber carries return flux and is magnetized at ~ 1.5 – 1.6 T. This is fully compatible with scintillator tile readout: SiPMs are insensitive to magnetic field, and the magnetized steel has negligible effect on hadronic shower development.

Limitations

- **Non-compensating.** The intrinsic resolution for neutral hadrons is $\sigma(E)/E \approx 55$ – $60\%/\sqrt{E}$, limited by the fundamental $e/h \neq 1$ of a steel-scintillator sampling calorimeter. The particle flow approach bypasses rather than solves this problem. In kinematic regions where charged-neutral separation is less effective, the jet energy measurement depends more heavily on this raw non-compensating response.
- **Large channel count.** ~ 8 million SiPM channels require massive quality control, and calibration effort. SiPM gain drift and dark count evolution over 15 years demand continuous monitoring.

3.6.3 Dual-Readout Fiber Calorimeter

Design

The dual-readout approach attacks the f_{em} fluctuation problem directly. Two types of fibers are interleaved in a copper or brass absorber matrix:

- **Scintillating fibers (S):** respond to all ionizing energy deposition, giving a signal proportional to total deposited energy with $e/h \neq 1$.
- **Clear (Čerenkov) fibers (C):** respond only to relativistic charged particles ($\beta > 1/n$), predominantly the e^+e^- from the electromagnetic shower component, giving a signal approximately proportional to f_{em} .

From the two signals, f_{em} can be extracted event by event and the energy corrected:

$$E_{\text{corrected}} = \frac{S - \chi C}{1 - \chi} \quad (3.9)$$

where χ is a calibration constant determined by the e/h ratios for the two signal types.

RD52 test beam results²⁵ have demonstrated hadronic energy resolution of $\sigma(E)/E \approx 30\text{--}35\%/\sqrt{E}$ after dual-readout correction, with more Gaussian response than conventional non-compensating calorimeters.

Strengths

- **Addresses the fundamental physics problem.** The f_{em} correction removes the dominant source of hadronic resolution degradation, achieving effective compensation event by event.
- **Superior standalone hadron resolution.** $\sim 30\text{--}35\%/\sqrt{E}$ after correction, compared to $\sim 55\text{--}60\%/\sqrt{E}$ for the tile calorimeter.
- **More Gaussian response.** The correction removes the non-Gaussian tails caused by f_{em} fluctuations, which is important for avoiding systematic biases in mass reconstruction and jet energy measurements.
- **Robust in challenging kinematic regions.** In conditions where particle flow performance is degraded, the dual-readout calorimeter provides a good standalone energy measurement — a safety net that the tile approach lacks.
- **Fewer channels.** With readout segmented into towers of $\sim 20\text{--}30$ mm laterally and two channels per tower (S and C), the total channel count is $\sim 80,000$ — two orders of magnitude fewer than the tile approach.

Limitations

- **Limited granularity.** The effective transverse granularity is set by the tower size ($\sim 20\text{--}30$ mm), and the standard design has **no longitudinal segmentation** — fibers run the full depth with readout only at the back. This limits 3D shower imaging capability and makes it harder to separate overlapping showers, identify shower start points, and track muons through the calorimeter.

- **Čerenkov light yield is low.** Clear fibers collect only Čerenkov photons, which are much less abundant than scintillation photons. The Čerenkov channel has worse photostatistics, limiting the precision of the f_{em} measurement. This is particularly important at low hadron energies (few GeV) where the Čerenkov signal may be too small for a reliable correction, and the dual-readout technique provides diminishing benefit.
- **Technology maturity.** While RD52 has demonstrated the principle convincingly in test beams, significant engineering challenges remain for a full collider detector. The most serious is fiber routing: in test beam configurations, scintillating and clear fibers extend ~ 1 m beyond the absorber to be grouped onto separate photodetectors. Scaling this approach to a full 4π detector with realistic space constraints is an unsolved problem. Assembly of the fiber/absorber matrix at the required scale and the long-term mechanical integrity of fibers under operational stresses are additional concerns.
- **ECAL-HCAL shower splitting.** With a crystal ECAL in front, hadrons that begin showering in the ECAL have their energy split between two very different detector technologies. The dual-readout correction in the HCAL applies only to the HCAL portion of the shower, not the total. For neutral hadrons, the nuclear interaction length of PbWO_4 is ~ 22 cm — comparable to the crystal depth of ~ 20 cm — so $\sim 60\%$ of neutral hadrons interact in the ECAL, creating split showers for which the dual-readout correction is incomplete.

3.6.4 Combining High Granularity and Dual Readout

The tile and fiber approaches each have distinct strengths — high granularity for pattern recognition, and dual readout for standalone hadron resolution. It is natural to ask whether these can be combined in a single detector.

Adding dual-readout capability to scintillator-steel tiles

Each scintillator tile in the HCAL is replaced by a pair of optically separate tiles: a front scintillator tile (producing the S signal from all ionizing energy deposition) and a back clear tile (producing only Čerenkov light, predominantly from the electromagnetic shower component). This achieves the dual-readout S/C measurement within the existing high-granularity tile geometry.

There are challenges:

- **Doubled channel count.** The number of readout channels increases from ~ 8 million to ~ 16 million, with corresponding increases in SiPM procurement, quality control, and calibration effort.
- **Čerenkov light yield.** The photostatistics from a single clear tile of ~ 3 mm thickness are low. However, since the Čerenkov light is detected by a separate photosensor from the scintillation light, that sensor can be independently optimized for this low-light regime (e.g., larger area, higher gain, or cooled operation).

Increasing granularity in the dual-readout fiber calorimeter

Greater physical segmentation — both transverse (smaller towers) and longitudinal (multiple readout depths) — could in principle bring the fiber calorimeter’s pattern recognition closer to that of the tile approach. The challenges are primarily practical:

- **Higher channel count.** Achieving granularity comparable to the tile calorimeter implies a similar total channel count, eliminating one of the fiber approach’s principal advantages.
- **Increased complexity.** The already-unsolved fiber routing problem becomes substantially harder with longitudinal segmentation, as fibers must be extracted and grouped at multiple depths rather than only at the back.

An alternative is virtual longitudinal segmentation (and without improving transverse segmentation) through precision timing of photon arrival at the photosensor: photons produced at different depths travel different distances along the fiber and arrive at slightly different times. However, this approach faces fundamental limitations.

For scintillation light, whose emission time constants (\sim few ns or longer) are comparable to or larger than the photon transit time along the entire fiber, the measured arrival times reflect primarily the scintillator decay characteristics rather than the emission depth. Virtual segmentation cannot be applied to the scintillation channel. This is a significant drawback because scintillation signal dominates over Čerenkov signal.

For the Čerenkov channel, light emission is prompt, but the time measured at the photosensor carries no direct information on shower depth without additional assumptions. The measured time is:

$$t_{\text{meas}} = t_{\text{emit}} + \frac{L}{v} \tag{3.10}$$

where t_{emit} is the time at which the charged particle produced Čerenkov light at a point inside the calorimeter, L is the distance from that point to the photosensor, and v is the speed of light propagation in the fiber. The depth information is contained in L , but extracting it requires knowledge of t_{emit} — and this is a single equation with two unknowns. Additional constraints must be applied: assumptions about when the initiating particle entered the calorimeter, how quickly the shower propagates in depth, and at what depth the Čerenkov emission occurred. For an isolated single hadron entering at a known time, these assumptions may be tractable. For overlapping showers or secondary particles produced deep in the cascade, they are not. It is essential to understand the influence of such assumptions on the extracted depth information and its associated uncertainty.

Assessment

The benefits of combining high granularity with dual readout are attractive, and simulation studies should be carried out to quantify the potential gains. Of the approaches considered:

- **Adding dual readout to scintillator-steel tiles** appears most promising: the channel count increase (factor of 2) is bounded and technically manageable, the high-granularity pattern recognition is preserved, and the dual-readout correction addresses the standalone resolution limitation directly.

- **Physical segmentation of the fiber calorimeter** is technically more challenging (fiber routing at multiple depths) and undermines the approach’s inherent simplicity advantage. Approaching the granularity achievable with scintillator-steel is challenging.
- **Virtual depth segmentation through timing** in the fiber calorimeter is limited by the fundamental mismatch between scintillator decay times and fiber transit times. It could provide depth information for the Čerenkov channel only, which gives the longitudinal profile of the electromagnetic shower component but not the hadronic component — precisely the part where depth information would be most valuable for pattern recognition.

3.6.5 Quantitative Impact on Jet Energy Resolution

Particle flow performance with crystal ECAL

The commonly quoted PFA jet energy resolution numbers ($\sim 3\text{--}4\%$ at 45 GeV) originate from ILD studies that assumed a 3.5 T magnetic field and a Si-W ECAL with $5\times 5\text{ mm}^2$ pads and ~ 30 longitudinal layers. These assumptions differ significantly from the CL2a concept (2–3 T field, crystal ECAL with $20\times 20\text{ mm}^2$ granularity and 2 longitudinal segments).

The PFA jet energy resolution can be approximately decomposed as (treating each component as independent, which is illustrative rather than rigorous):

$$\left(\frac{\sigma_E}{E}\right)_{\text{jet}}^2 \approx \left(\frac{0.65 \cdot \sigma_p/p}{\text{tracker}}\right)^2 + \left(\frac{0.25 \cdot \sigma_E^\gamma/E^\gamma}{\text{ECAL}}\right)^2 + \left(\frac{0.10 \cdot \sigma_E^{nh}/E^{nh}}{\text{HCAL}}\right)^2 + \sigma_{\text{confusion}}^2 \quad (3.11)$$

For a 45 GeV jet (average photon energy ~ 5 GeV, average neutral hadron energy ~ 4.5 GeV):

Table 3.14: Estimated contributions to jet energy resolution at 45 GeV, comparing the tile and dual-readout HCAL options with a crystal ECAL. The confusion term is extrapolated from published ILD studies at 3.5 T and has not been simulated for the CL2a configuration. The tracker term is negligible in both cases.

Component	Tile HCAL (%)	Dual-readout HCAL (%)
Photon term (crystal ECAL)	0.34	0.34
Neutral hadron term	2.6	1.4
Confusion term (estimated)	2–3	2–3
Total (quadrature)	~ 3.6	~ 2.9

The dual-readout HCAL improves the neutral hadron contribution from $\sim 2.6\%$ to $\sim 1.4\%$, yielding a total jet resolution improvement of ~ 0.7 percentage points. This is meaningful but not dominant — the **confusion term controls the overall jet resolution** regardless of HCAL technology.

The magnetic field as a significant driver

The confusion term is driven significantly by the magnetic field strength, which determines how effectively charged particles are separated from neutrals at the calorimeter face. The

variable field strategy (Section 3.5.1) — running at higher field for higher-energy physics — addresses the confusion term directly, independent of the HCAL technology choice.

3.6.6 The HCAL as Flux Return

With the solenoid placed inside the HCAL (Section 3.5.2), the HCAL steel absorber serves as partial magnetic flux return, carrying a substantial fraction of the return flux. This has specific implications for the HCAL technology choice:

- The absorber **must be ferromagnetic** (steel/iron), ruling out non-magnetic materials such as brass or copper. Standard low-carbon structural steel works well for both calorimetry and magnetics.
- The steel is magnetized at $\sim 1.5\text{--}1.6$ T, which is fully compatible with scintillator tile readout (SiPMs are field-insensitive) and has negligible impact on shower physics.
- For the dual-readout fiber option, the absorber is typically copper or brass in the RD52 design. Using magnetized steel would require redesigning the fiber/absorber geometry. While not impossible in principle, this has not been studied and represents an additional engineering challenge.

The flux return consideration provides a mild preference for the tile approach, which naturally uses steel absorber, over the dual-readout approach, which would need to adapt its absorber material.

3.6.7 Technology Assessment

The choice between scintillator-steel tiles and dual-readout fibers is the most difficult technology decision in the entire detector design. Neither option is clearly superior; each has genuine strengths that the other lacks.

The arguments favoring **scintillator-steel tiles** for the CL2a baseline are:

- i) The FCC-ee physics program is dominated by jet measurements at 91–240 GeV where particle flow works well and the confusion term, rather than HCAL intrinsic resolution, limits performance.
- ii) The presence of a separate deep ECAL, which measures all incoming photons before they reach the HCAL, reduces the cluster multiplicity and simplifies the pattern recognition task in the HCAL. This benefits the tile approach in particular, though it also reduces the demands placed on it.
- iii) The 3D shower imaging from 50 longitudinal layers of 30×30 mm² tiles is valuable for many analyses beyond jet energy: τ reconstruction, missing energy, muon identification, and software compensation.
- iv) The technology is mature, with extensive prototyping and beam test validation by the CALICE collaboration.

- v) Steel absorber naturally serves as magnetic flux return, integrating cleanly with the inside-HCAL solenoid placement.
- vi) MIP-based calibration is robust and well-understood.

The arguments favoring **dual-readout fibers** are also compelling:

- i) Superior standalone hadron resolution ($\sim 30\%/\sqrt{E}$ vs. $\sim 55\%/\sqrt{E}$) with more Gaussian response.
- ii) Robust performance in kinematic regions where particle flow is degraded — a safety net at the highest jet energies and in forward regions.
- iii) Far fewer readout channels ($\sim 80,000$ vs. ~ 8 million), with corresponding savings in QC and calibration effort.
- iv) Addresses the fundamental f_{em} fluctuation problem rather than bypassing it.

For CL2a, the **scintillator-steel tile HCAL is adopted** as the baseline, on the grounds that the particle flow approach is well-matched to the dominant Z-pole and ZH physics programs, the technology is mature, and the steel absorber integrates naturally with the solenoid flux return.

However, the dual-readout fiber calorimeter is **strongly recommended for the complementary detector CL2b**. This provides:

- Independent systematic checks on all jet energy measurements, with fundamentally different calorimetric approaches.
- A direct experimental comparison of particle flow vs. dual-readout at a Higgs factory — data that would be invaluable for the design of future collider detectors.
- Coverage of the high-energy regime ($t\bar{t}$ threshold) where dual-readout may outperform particle flow.
- Risk mitigation: if either approach has unforeseen limitations in operation, the other provides a fallback.

This is perhaps the strongest case for the two-detector complementarity strategy advocated throughout this report. The tile vs. dual-readout question may ultimately be answerable only with collider data, and having both technologies deployed simultaneously would settle it definitively.

3.6.8 Summary of HCAL Discussion

The HCAL technology choice did not change from CL1a to CL2a — scintillator-steel tiles remain the baseline. However, the *reasoning* evolved substantially through the discussion:

- i) The presence of a separate deep ECAL was recognized as simplifying the HCAL’s pattern recognition task by measuring incoming photons before they reach the HCAL, reducing both the demands on the HCAL and the performance difference between the two technologies.

- ii) The confusion term was identified as the dominant limitation on jet energy resolution, making the HCAL intrinsic resolution (and hence the tile vs. dual-readout difference) a second-order effect.
- iii) The magnetic field strength was recognized as a significant driver of jet resolution through its effect on the confusion term, reinforcing the variable field strategy.
- iv) The solenoid placement inside the HCAL created a mild preference for steel absorber (compatible with flux return), favoring the tile approach.
- v) The case for two-detector complementarity was strengthened — this is the subsystem where having both technologies deployed simultaneously offers the greatest scientific return.

The PFA performance numbers frequently cited in the literature (from ILD studies at 3.5 T with Si-W ECAL) were found to be **not directly applicable** to the CL2a geometry. A proper evaluation of jet energy resolution for the CL2a concept — crystal ECAL, 2–3 T variable field, scintillator-steel HCAL — requires dedicated full simulation, which is identified as a priority R&D activity.

3.7 Muon System

The muon system underwent a complete technology change from CL1a to CL2a — from micro-Resistive WELL (μ -RWELL) gaseous detectors to scintillator bars with wavelength-shifting fiber and SiPM readout. This change, prompted by the physicist’s challenge, illustrates a broader lesson about matching technology to actual requirements rather than selecting the most technically impressive available option.

3.7.1 Requirements at FCC-ee

The starting point is a clear definition of what the muon system must actually do. At FCC-ee, the muon system is an **identifier**, not a **measurer**: its job is to confirm that a particle penetrating the full calorimeter and solenoid coil is a muon, not to independently measure the muon momentum (which the tracker does far better).

The identification relies on the penetrating nature of muons: multiple detector stations are interleaved with absorber (iron) layers, and a particle reaching the outer stations through ~ 7 – 8 nuclear interaction lengths of material is almost certainly a muon. Multi-station coincidence provides further rejection of hadronic punch-through. The requirements on each station are therefore:

- High detection efficiency ($>95\%$) for minimum ionizing particles.
- Sufficient position resolution (~ 1 cm) for track matching.
- Timing resolution better than ~ 10 ns for bunch crossing identification.
- Coverage of ~ 1000 – 1400 m² total area across 3–4 stations.
- Reliable operation over 15 years with minimal maintenance.

Position resolution

The position resolution required for track matching is set by the uncertainty in extrapolating a track from the tracker through the calorimeter and coil to the muon stations. This extrapolation uncertainty is dominated by multiple scattering, giving approximately ~ 20 mm for a 10 GeV muon and scaling as $1/p$.

A muon detector with position resolution of ~ 1 cm provides a matching window of a few cm^2 . Whether this is adequate depends on the background hit rate in the muon stations — primarily from machine-related sources rather than physics. For the background levels expected at FCC-ee, this is likely sufficient, though the exact requirement depends on detailed background simulations that have not yet been performed for this configuration. The size (and hence resolution) can be adjusted as a straightforward design optimization once background levels are better characterized.

What is clear is that the ~ 100 μm resolution of μ -RWELL provides no benefit: even in the most demanding background scenario, a matching window of ~ 1 mm^2 at the muon stations is far smaller than any conceivable need.

Rate capability and radiation hardness

At FCC-ee, the muon stations at $R \approx 4\text{--}5$ m see hit rates of $\sim \text{Hz}/\text{cm}^2$ from physics events, with modest additional contributions from beam backgrounds. This is negligible compared to the CMS endcap environment where μ -RWELL is being deployed (MHz/cm^2). Similarly, the integrated radiation dose over 15 years of FCC-ee operation is negligible for any detector technology.

The mismatch

Table 3.15: Muon system requirements at FCC-ee compared to the capabilities of μ -RWELL, illustrating the mismatch between the initial technology choice and the actual needs.

Property	FCC-ee need	μ -RWELL	Matched?
Position resolution	~ 1 cm	~ 100 μm	Overkill
Rate capability	$\sim \text{Hz}/\text{cm}^2$	MHz/cm^2	Overkill
Radiation hardness	Negligible	Excellent	Overkill
Detection efficiency	$>95\%$	$>97\%$	Yes
Timing	<10 ns	~ 5 ns	Yes

The μ -RWELL meets the efficiency and timing requirements but massively exceeds what is needed in position resolution, rate capability, and radiation hardness. This excess capability comes at a cost in operational complexity (gas system, high voltage, environmental sensitivity) without providing any physics benefit.

3.7.2 Technology Choice: Scintillator Bars

The physicist proposed scintillator bars with embedded wavelength-shifting (WLS) fibers and dual-end SiPM readout as a technology that precisely matches these requirements. This is the approach being adopted by the Belle II experiment for its muon system upgrade²⁶ and is used in the Mu2e cosmic ray veto at Fermilab²⁷, among other applications.

Design

Each detector element is an extruded plastic scintillator bar:

- Typical dimensions: ~ 30 mm wide \times ~ 10 mm thick \times ~ 2 – 4 m long.
- Co-extruded TiO_2 reflective coating for light containment.
- Embedded wavelength-shifting fiber (~ 1 mm diameter, Y-11 or similar) running the length of the bar.
- SiPM readout on both ends of each bar.

Each muon station consists of two layers of bars in orthogonal orientations (X and Y views), providing two-coordinate position measurement.

Performance

Detection efficiency. A minimum-ionizing muon traversing ~ 10 mm of plastic scintillator produces ~ 20 – 40 photoelectrons at each SiPM (after WLS fiber collection and SiPM photon detection efficiency). This gives essentially 100% detection efficiency with any reasonable threshold. The double-ended readout provides coincidence-based noise rejection and redundancy — if one SiPM fails, the other end still detects the muon.

Position resolution. Transverse to the bar, the resolution is determined by the bar width: $\sigma_{\text{trans}} = 30/\sqrt{12} \approx 9$ mm. Along the bar, the position is obtained from the time difference between the two SiPM signals. With ~ 200 – 300 ps timing per SiPM (achievable with modern devices) and signal propagation speed of ~ 17 cm/ns in the WLS fiber:

$$\sigma_{\text{along}} = \frac{v \times \sigma_{\Delta t}}{\sqrt{2}} \approx \frac{170 \times 0.3}{\sqrt{2}} \approx 36 \text{ mm} \quad (3.12)$$

Both resolutions are well within the ~ 1 – 5 cm required by the track extrapolation uncertainty.

Timing. The coincidence of two SiPM signals gives timing resolution $\sigma_t \approx \sigma_{t,\text{SiPM}}/\sqrt{2} \approx 0.7$ ns — far better than the ~ 10 ns needed for bunch crossing identification.

Operational advantages

The physicist emphasized operational simplicity as a decisive criterion for a subsystem covering >1000 m² that must operate reliably for 15 years:

The absence of a gas system is perhaps the single most important operational advantage. A gas system serving ~ 1000 – 1400 m² of gaseous detectors requires continuous gas mixing,

Table 3.16: Operational comparison of scintillator bars and gaseous detectors (μ -RWELL or similar) for the muon system.

Aspect	Scintillator bars	Gaseous detectors
Gas system	None	Required (mixing, distribution, monitoring)
High voltage	$\sim 30\text{--}50$ V (SiPM)	$\sim 3\text{--}4$ kV
Environmental sensitivity	Low (solid state)	Moderate (gain depends on T , P , humidity)
Aging	Minimal (scintillator stable for decades)	Gas aging possible over 15 years
Maintenance	Individual SiPM replacement	Gas system servicing, HV monitoring
Commissioning	Straightforward	Gas conditioning, HV training

distribution, purity monitoring, flow control, and potentially gas recovery (for expensive or greenhouse gases). This infrastructure must be maintained throughout the 15-year program, including during shutdown periods. A scintillator system has no equivalent requirement — once installed, it operates with minimal intervention.

Cost

For $\sim 1000\text{--}1400$ m² total instrumented area with bars of ~ 30 mm width:

- Bars per station (two orthogonal layers): $\sim 12,000$.
- Total for 3–4 stations: $\sim 36,000\text{--}48,000$ bars.
- Cost per bar (scintillator + fiber + 2 SiPMs): $\sim \$15\text{--}40$.
- Total bar cost: $\sim \$1\text{--}1.5$ M.
- Including electronics, cables, support structures: $\sim \$3\text{--}5$ M total.

This is a very modest cost for a major detector subsystem — comparable to or less than a gaseous detector system of similar area, and far less than the multi-million-channel SiPM systems required for the HCAL.

Precedents

The Belle II experiment is upgrading its muon system (replacing RPCs that suffered from aging and efficiency loss) with exactly this technology, in a radiation environment similar to FCC-ee. Their evaluation of multiple technology options and selection of scintillator bars validates the choice for similar conditions.

The Mu2e cosmic ray veto demonstrates the technology at large scale, with experience in industrial scintillator extrusion, mass production of bars with embedded fibers, SiPM quality control, and system integration directly applicable to FCC-ee.

3.7.3 Integration with Return Yoke

The muon detector stations are interleaved with iron absorber layers in the return yoke outside the HCAL. The total absorber depth before the outermost muon station determines the hadron punch-through rejection:

Table 3.17: Absorber depth and approximate hadron punch-through probability for the muon system.

Component	Depth (λ_I)	Cumulative (λ_I)
HCAL (steel + scintillator)	6.0	6.0
Solenoid coil	0.4	6.4
Return yoke layers	1–2	7.4–8.4
Punch-through probability at 8 λ_I :		$\sim 0.03\%$

With the HCAL providing 6 λ_I , the solenoid coil adding $\sim 0.4 \lambda_I$, and 1–2 λ_I of iron in the return yoke between muon stations, the total absorber depth is ~ 7.5 – $8.5 \lambda_I$. The hadron punch-through probability at this depth is $< 0.1\%$, ensuring clean muon identification.

As discussed in Section 3.5.2, with the solenoid inside the HCAL, the return yoke thickness is driven primarily by muon physics needs rather than magnetic flux requirements (the HCAL steel carries a substantial fraction of the return flux). The yoke iron layers are optimized for muon identification: thick enough for adequate hadron absorption, thin enough to keep the overall detector compact, with 3–4 gaps for muon detector stations at strategic depths.

A typical station arrangement might be:

- Station 1: immediately outside the HCAL/coil, after $\sim 6.4 \lambda_I$.
- Station 2: after ~ 10 cm additional iron ($\sim 0.6 \lambda_I$ additional).
- Station 3: after ~ 10 cm more iron ($\sim 1.2 \lambda_I$ cumulative additional).
- Station 4 (optional): after final iron layer ($\sim 1.8 \lambda_I$ cumulative additional).

The first station is primarily for muon identification (anything reaching it through $6.4 \lambda_I$ is very likely a muon). The outer stations provide redundancy, improved purity through multi-station coincidence, and a crude standalone momentum measurement from the deflection in the magnetized iron (useful as a cross-check, though the tracker measurement is far superior).

3.7.4 Summary of Muon System Evolution

The muon system change from μ -RWELL to scintillator bars is perhaps the clearest example in this study of a design choice driven by properly matching technology to requirements:

- i) The FCC-ee muon system needs are fundamentally different from LHC: identification rather than measurement, in a benign rate and radiation environment.
- ii) The μ -RWELL's impressive capabilities (100 μm resolution, MHz/cm² rate handling, radiation hardness) are entirely wasted at FCC-ee — the experiment does not need and cannot benefit from any of them.
- iii) Scintillator bars meet every actual requirement (efficiency, position resolution, timing) while offering decisive advantages in operational simplicity, reliability, and cost.
- iv) The Belle II and Mu2e precedents demonstrate the technology at the relevant scale and in comparable operating conditions.

The lesson extends beyond the muon system: in detector design, selecting the most advanced available technology is not always the best choice. The right technology is the one that meets the actual requirements with the greatest margin of reliability and operational simplicity, particularly for subsystems that must function unattended over a decade or more.

3.8 Luminosity Monitor

The luminosity monitor technology — a precision silicon-tungsten sampling calorimeter — did not change from CL1a to CL2a. However, the discussion substantially deepened the understanding of the requirements, revealing that the principal challenges are metrological and operational rather than detector-physical. The physicist's questions exposed a circular logic in one proposed monitoring approach and clarified the distinct requirements for absolute and relative luminosity determination.

3.8.1 The Measurement Method

Luminosity at FCC-ee is measured by counting small-angle Bhabha scattering ($e^+e^- \rightarrow e^+e^-$) events within a precisely defined angular acceptance:

$$\mathcal{L} = \frac{N_{\text{Bhabha}}}{\sigma_{\text{Bhabha}}(\theta_{\min}, \theta_{\max})} \quad (3.13)$$

The Bhabha cross-section at small angles is large, precisely calculable in QED (dominated by t -channel photon exchange), and falls steeply with angle: $d\sigma/d\theta \propto 1/\theta^3$.

This steep dependence means the accepted cross-section is dominated by events near the inner acceptance edge θ_{\min} , and a small error in θ_{\min} produces a large error in the luminosity:

$$\frac{\delta\sigma}{\sigma} \approx 2 \frac{\delta\theta_{\min}}{\theta_{\min}} \quad (3.14)$$

The precision requirements are:

- **Absolute luminosity:** 10^{-4} , needed for the Z-pole cross-section measurements, N_ν determination, and electroweak precision program.
- **Relative luminosity:** 10^{-5} , needed for the Z lineshape scan and W/top threshold scans, where the shape of the cross-section vs. energy encodes the particle mass and width.

3.8.2 Position and Stability Requirements

The physicist pressed for a detailed accounting of the geometric precision requirements, distinguishing between knowledge (how well you know where the detector is) and stability (how well it stays there).

Geometric parameters

For a luminometer at distance $z \approx 2500$ mm from the interaction point with inner acceptance at $\theta_{\min} \approx 60$ mrad ($r_{\min} \approx 150$ mm), the sensitivity of the luminosity to various geometric parameters differs significantly:

Table 3.18: Geometric precision requirements for the luminosity monitor, derived from the 10^{-4} absolute and 10^{-5} relative luminosity targets using Equation 3.14 and its analogs for other geometric parameters.

Parameter	For 10^{-4}	For 10^{-5}	Difficulty
Inner edge radius	7.5 μm	0.75 μm	Very demanding
z position	125 μm	12.5 μm	Moderate
Transverse offset	1.5 mm	0.5 mm	Relaxed
Tilt	0.6 mrad	0.2 mrad	Relaxed

The inner edge radius dominates — both its absolute knowledge (for 10^{-4}) and its stability over the duration of the lineshape scan (for 10^{-5}). The transverse offset and tilt enter only at second order (due to azimuthal symmetry cancellation) and are comparatively relaxed.

The z position requirement is also relatively relaxed because it enters through the ratio $\delta z/z$, which benefits from the large lever arm ($z \approx 2500$ mm).

Absolute position knowledge

The inner edge of the silicon sensors can be defined by photolithography to ~ 1 μm precision. The sensor position on its mounting structure can be surveyed to \sim few μm using coordinate measuring machines. The as-built inner radius can therefore be known to ~ 3 – 5 μm , meeting the 7.5 μm requirement.

However, the relevant quantity is the inner edge position relative to the **beam axis**, not to a mechanical reference. The beam position at the luminometer ($z = 2500$ mm from the IP) depends on both the beam position and angle at the interaction point:

$$x_{\text{beam}}(z_{\text{lumi}}) = x_{\text{beam}}(0) + x'_{\text{beam}} \times z_{\text{lumi}} \quad (3.15)$$

A beam angle uncertainty of 1 μrad gives a position uncertainty of 2.5 μm at the luminometer. The beam angle must therefore be known to ~ 3 μrad for the absolute measurement, requiring precise beam position monitors (BPMs) near the interaction point and careful cross-calibration between the BPM reference frame and the luminometer reference frame.

Stability for relative luminosity

The 10^{-5} relative requirement demands that the effective inner edge radius be stable to $\sim 0.75 \mu\text{m}$ over the duration of the lineshape scan, which may span months to years as different energy points are measured in separate running periods.

This is an extraordinary stability requirement. Its feasibility depends on the thermal environment, mechanical design, and operational strategy.

3.8.3 Thermal and Mechanical Stability

Thermal expansion

The physicist identified temperature variations as a potentially limiting factor. The coefficient of thermal expansion (CTE) determines how temperature changes translate to position shifts:

Table 3.19: Thermal expansion of the luminometer inner edge ($r_{\min} = 150 \text{ mm}$) for different support materials.

Support material	CTE ($\mu\text{m}/\text{m}/^\circ\text{C}$)	δr per $^\circ\text{C}$ (μm)
Aluminum	23	3.45
Steel	12	1.80
Invar	1.3	0.20
Carbon fiber (axial)	1–2	0.15–0.30

For an aluminum support structure, a temperature change of just $\sim 2^\circ\text{C}$ gives a $7 \mu\text{m}$ shift — consuming the full 10^{-4} tolerance. For the 10^{-5} relative requirement ($0.75 \mu\text{m}$), the tolerance tightens to $\sim 0.2^\circ\text{C}$ in aluminum.

With Invar or carbon fiber support ($\delta r \approx 0.2 \mu\text{m}/^\circ\text{C}$), a temperature variation of $\sim 4^\circ\text{C}$ is tolerable for 10^{-5} . This is achievable with reasonable environmental control.

The relevant thermal path includes not just the luminometer body but the **entire mechanical chain** from the beam pipe (which defines the beam axis reference) to the luminometer inner edge. Every element in this chain contributes thermal expansion. This argues strongly for:

- Low-CTE materials (Invar, carbon fiber) for all positioning-critical elements.
- Monolithic construction where possible, minimizing joints that can exhibit creep or relaxation.
- Active temperature monitoring with precision sensors ($\sim 10 \text{ mK}$ resolution) for offline correction of residual thermal expansion.

Vibration

The machine-detector interface region contains several vibration sources: cryogenic compressors and cold heads, cooling water flow, vacuum pumps (during commissioning), and ground motion.

For a symmetric vibration of amplitude A about the nominal position, the first-order effect on the acceptance cancels by symmetry, and the residual second-order effect is:

$$\frac{\delta\sigma}{\sigma} \sim \left(\frac{A}{r_{\min}} \right)^2 \quad (3.16)$$

Even for $A = 50 \mu\text{m}$ (a large vibration amplitude): $\delta\sigma/\sigma \sim (50/150,000)^2 \sim 10^{-7}$ — completely negligible.

The more serious concern is relative vibration between the luminometer and the beam axis, where the two vibrate independently. This is mitigated by mounting the luminometer as rigidly as possible to the beam pipe or to a common support structure with the BPMs, so that they move together. The machine-detector interface design should treat the beam pipe, BPMs, and luminometer support as a single mechanical system.

3.8.4 Monitoring the Acceptance

The AI initially proposed “continuous Bhabha monitoring to track the effective acceptance in real time.” The physicist identified a fundamental flaw in this reasoning.

The circular logic

The luminometer measures luminosity by counting Bhabha events within its acceptance. If the acceptance shifts and the Bhabha count changes, the luminometer cannot distinguish “luminosity changed” from “acceptance changed” — it measures only the product $\mathcal{L} \times A_{\text{eff}}$. Using the same Bhabha events to simultaneously determine the luminosity and monitor the acceptance is circular.

Certain observables within the luminometer data are sensitive to specific types of geometry changes independent of luminosity: the azimuthal distribution develops a $\cos\phi$ modulation if the beam shifts transversely, and an up-down asymmetry reveals vertical offsets. However, these observables detect transverse displacements and tilts — parameters for which the tolerance is already relaxed (Table 3.18). They are **insensitive to the critical parameter**: a pure radial shift of the inner acceptance edge, because the detector pads shift with the edge and the distribution measured in detector coordinates is unchanged.

What actually works

The acceptance must be monitored through means independent of the luminosity measurement itself:

Hardware position monitoring. Capacitive position sensors or laser interferometric systems can measure the luminometer position relative to the beam pipe (or a stable reference) with sub- μm precision, continuously. These directly track the quantity of interest — the geometric relationship between detector and beam axis — without relying on physics events.

Beam position monitoring. BPMs near the interaction point provide the beam orbit with $\sim\mu\text{m}$ precision and $\sim\mu\text{rad}$ angular knowledge. Combined with hardware position monitoring of the luminometer, this gives the effective beam-luminometer geometry.

Wide-angle Bhabha cross-check. Bhabha scattering at wide angles ($\theta > 200$ mrad), detected in the main electromagnetic calorimeter, provides a completely independent luminosity measurement with different systematic uncertainties. The angular acceptance is defined by the main tracker and ECAL rather than the forward luminometer, so systematic shifts in the luminometer acceptance do not affect it.

However, the statistical precision of wide-angle Bhabhas is limited. Using a Bhabha cross-section of 10–20 nb typical for wide-angle selections and the Z-pole luminosity of $\sim 2 \times 10^{36} \text{ cm}^{-2}\text{s}^{-1}$, the rate is $\sim 20\text{--}40$ Hz, giving $\sim 2\text{--}3$ million events per day. The statistical precision per month is:

$$\frac{1}{\sqrt{7 \times 10^7}} \approx 1.2 \times 10^{-4} \quad (3.17)$$

This is adequate as a cross-check at the 10^{-4} level but **insufficient for 10^{-5} monitoring** on practical timescales. Wide-angle Bhabhas serve as an independent validation, not a primary monitoring tool.

3.8.5 Operational Strategy for Relative Luminosity

Given that hardware monitoring at the 10^{-5} level is extremely demanding and physics-based monitoring is statistics-limited, the operational strategy becomes a critical component of achieving 10^{-5} relative precision.

Interleaved energy scans

The most powerful approach is to alternate between energy points on short timescales (hours) rather than running at one energy for weeks before switching. Any slow systematic drift (thermal expansion, mechanical creep, beam orbit evolution) is then common to all energy points within each short cycle and cancels in the cross-section ratios.

The residual systematic is the drift within a single cycle (hours), which is far easier to control than drift over months:

- Thermal drifts over hours are small and smooth, easily tracked by temperature sensors.
- Mechanical creep over hours is negligible for a properly designed structure.
- Beam orbit variations over hours are tracked by BPMs.

The interleaving strategy converts a long-term stability problem ($0.75 \mu\text{m}$ over months) into a short-term stability problem ($0.75 \mu\text{m}$ over hours), which is far more tractable.

Redundancy

Two identical luminometers on opposite sides of the interaction point provide independent measurements. Agreement between the two gives confidence in the result; disagreement reveals systematic problems. Since the two luminometers are at different z positions (and different ϕ orientations relative to the crossing plane), they have different sensitivities to beam geometry changes and different thermal/mechanical environments, making them genuinely complementary.

Integrated monitoring approach

The 10^{-5} relative luminosity is ultimately achieved through a combination of:

- i) **Intrinsically stable mechanical design** — low-CTE materials, monolithic construction, kinematic mounting.
- ii) **Continuous hardware monitoring** — capacitive sensors or interferometry tracking the luminometer-beam geometry at sub- μm precision.
- iii) **Interleaved energy scans** — converting long-term drifts to short-term variations that cancel in cross-section ratios.
- iv) **Independent cross-checks** — wide-angle Bhabhas in the main detector, redundant luminometers on both sides of the IP.

No single technique achieves 10^{-5} alone — the combination is essential.

3.8.6 Detector Design

The silicon-tungsten sampling calorimeter design is well-matched to the requirements:

- **~ 20 layers** of tungsten ($\sim 1 X_0 = 3.5$ mm each) interleaved with silicon pad sensors.
- **Total depth $\sim 20 X_0$** (~ 100 – 120 mm), adequate for full containment of Bhabha electrons up to the beam energy.
- **Fine radial segmentation** near the inner edge (~ 1 mm pad pitch), enabling precise measurement of the Bhabha radial distribution for acceptance studies.
- **Azimuthal segmentation** for monitoring beam-detector alignment through the ϕ distribution of Bhabha events.
- **Multiple radial rings** providing redundant acceptance definitions at different θ values.

The silicon sensor edges, defined by photolithography, provide the most precise available definition of the physical acceptance boundary. The tungsten absorber's short radiation length and small Molière radius (~ 9 mm) keep the calorimeter compact and the showers narrow, maximizing the position resolution for individual Bhabha electrons.

3.8.7 Integration with the Machine-Detector Interface

The luminometer design must be developed jointly with the accelerator team because:

- The beam pipe geometry and inner radius at $z = 2500$ mm constrain the luminometer inner acceptance.
- The ~ 30 mrad crossing angle affects the acceptance geometry and the Bhabha event topology.
- Final focus elements create synchrotron radiation backgrounds that must be shielded from the luminometer.

- The mechanical support path from beam pipe to luminometer determines the thermal and vibrational stability.
- Access for maintenance, alignment surveys, and hardware monitoring must be planned from the start within the congested MDI region.

The luminometer is among the most accelerator-coupled detector elements, and its design cannot be finalized independently of the interaction region layout.

3.8.8 Summary of Luminosity Monitor Discussion

The luminosity monitor technology choice did not change, but the discussion produced several important clarifications:

- i) The **position requirements were quantified**: $7.5 \mu\text{m}$ for absolute luminosity, $0.75 \mu\text{m}$ stability for relative luminosity. The inner edge radius is the critical parameter; transverse offsets and tilts are comparatively relaxed.
- ii) **Thermal stability** was identified as a potentially limiting factor, driving the choice of low-CTE support materials (Invar, carbon fiber) and active temperature monitoring.
- iii) The proposal for **continuous Bhabha-based acceptance monitoring was found to be circular** — the luminometer cannot monitor its own acceptance using the same events it uses to measure luminosity. Hardware monitoring (capacitive sensors, interferometry) is the correct approach.
- iv) The **operational strategy** (interleaved energy scans, redundant luminometers, independent wide-angle cross-checks) was recognized as equally important as the hardware design for achieving 10^{-5} relative precision.
- v) The design must be **co-developed with the accelerator MDI team**, as the luminometer is among the most accelerator-coupled detector elements.

The luminosity monitor discussion illustrates that for some subsystems, the detector technology is not the primary challenge — the metrology, environmental control, and operational strategy are equally or more important. A perfect detector with inadequate mounting stability or suboptimal scan strategy would fail to achieve the physics goals regardless of its intrinsic performance.

Chapter 4

The Revised Integrated Detector

This chapter presents the revised detector concepts CL2a and CL2b, incorporating all the changes that emerged from the subsystem examination of Chapter 3. The primary concept CL2a is described in detail, including a self-consistent geometric layout. The complementary concept CL2b is presented more briefly, emphasizing where it differs from CL2a.

4.1 CL2a: Detector Layout

The CL2a detector is built from the inside out, with each subsystem's dimensions following from the previous one. The self-consistent radial layout in the barrel region is summarized in Table 4.1 and shown schematically in Figure 4.1.

Several design choices in this layout deserve comment:

Gaps between subsystems

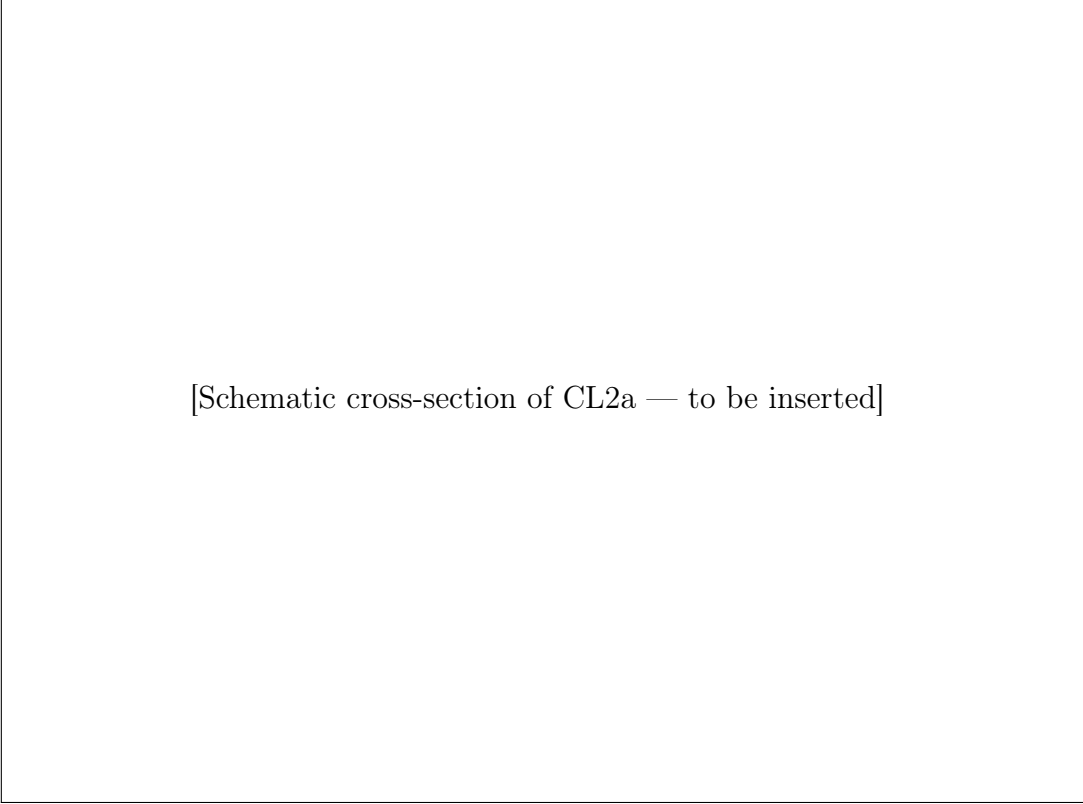
Small radial gaps are allowed between subsystems for mechanical clearance, cable routing, and thermal isolation:

- Between outer wrapper and ECAL (~ 45 mm): space for wrapper services, ECAL front-face support, and a small air gap.
- Between ECAL and solenoid (~ 50 mm): mechanical clearance and thermal isolation between the room-temperature ECAL and the cryogenic solenoid.
- Between solenoid and HCAL (~ 50 mm): clearance for coil cryostat and HCAL front-face support.

These gaps contribute dead material (cables, support structures) that is not included in the idealized material budgets above. In practice, the gaps should be minimized and any services routed along z (parallel to the beam) rather than radially where possible.

HCAL depth

The HCAL consists of ~ 50 layers, compared with ~ 50 layers in CL1a, of 20 mm steel absorber plates interleaved with 3 mm scintillator tiles, with ~ 2 mm gaps for tile wrapping and SiPM mounting. The total pitch per layer is ~ 25 mm, giving a total radial depth of ~ 1250 mm.



[Schematic cross-section of CL2a — to be inserted]

Figure 4.1: Schematic radial cross-section of the CL2a detector concept (not to scale). The dimensions correspond to Table 4.1.

Table 4.1: CL2a radial layout in the barrel region at $z = 0$. The R_{in} and R_{out} columns give the inner and outer radial extent of each subsystem. Material budgets are for a radial track at normal incidence.

Subsystem	Technology	R_{in} (mm)	R_{out} (mm)	Material
Beam pipe	Be, locally thinned	10	12	0.08% X_0
Vertex/inner Si	MAPS, 65 nm, 6 curved layers	12	300	<0.2% X_0 (total)
Inner wall	Carbon fiber	340	345	$\sim 0.1\%$ X_0
Main tracker	Drift chamber, He:iC ₄ H ₁₀ 90:10	345	2000	$\sim 0.2\%$ X_0 (gas + wires)
Outer wrapper	AC-LGAD, single layer	2000	2005	0.4–1.0% X_0
ECAL	PbWO ₄ crystal, 2 segments	2050	2250	22 X_0
Solenoid	SC, 3 T design, variable 1.5–3 T	2300	2450	$\sim 0.4 \lambda_I$
HCAL	Scint.-steel tiles, ~ 50 layers	2500	3750	$\sim 6 \lambda_I$
Return yoke + muon system	Steel + scint. bars, 3–4 stations	3750	4400	$\sim 1.5 \lambda_I$

The steel thickness totals ~ 1000 mm, providing $\sim 6 \lambda_I$ ($\lambda_I^{\text{steel}} \approx 167$ mm). Combined with the solenoid coil ($\sim 0.4 \lambda_I$) and the crystal ECAL ($\sim 1 \lambda_I$ nuclear), the total absorber before the muon system is $\sim 7.4 \lambda_I$.

The HCAL steel serves simultaneously as calorimeter absorber and magnetic flux return (Section 3.5), carrying a substantial fraction of the solenoid return flux.

Muon system depth

The return yoke outside the HCAL consists of 3–4 iron layers (~ 100 mm each) interleaved with scintillator bar muon stations. The total additional absorber depth is $\sim 1.5 \lambda_I$, bringing the cumulative depth before the outermost muon station to $\sim 8.9 \lambda_I$ and reducing the hadron punch-through probability to $< 0.05\%$.

Overall dimensions

The CL2a barrel detector has an outer radius of ~ 4.4 m. The barrel half-length is determined by the angular coverage requirement and the longest subsystem:

- Drift chamber active volume: $|z| < 2000$ mm.
- Drift chamber stay system: extends to $|z| \approx 2500\text{--}2800$ mm.
- ECAL barrel: $|z| \lesssim 2500$ mm.
- HCAL barrel: $|z| \lesssim 2800$ mm.
- Return yoke/muon: $|z| \lesssim 3200$ mm.

The total barrel half-length is $\sim 3.0\text{--}3.2$ m, giving an overall barrel length of $\sim 6.0\text{--}6.4$ m. Endcap systems (tracking disks, ECAL endcap, HCAL endcap, and muon endcap stations) extend the total detector length to $\sim 10\text{--}12$ m.

4.1.1 Longitudinal Layout

The longitudinal layout is constrained by the drift chamber stay system, which consumes $\sim 500\text{--}800$ mm per end between the active wire volume and the outer cylinder. This sets the minimum z extent of the barrel calorimetry and determines where endcap systems must begin:

The polar angle coverage of the barrel tracking system extends to:

$$\theta_{\min}^{\text{barrel}} \approx \arctan\left(\frac{R_{\text{inner}}^{\text{DC}}}{z_{\text{active}}^{\text{DC}}}\right) = \arctan\left(\frac{345}{2000}\right) \approx 9.8^\circ \quad (4.1)$$

corresponding to $|\cos\theta| \lesssim 0.985$ — excellent forward coverage.

4.2 CL2a: Technology Summary

Table 4.3 summarizes the CL2a technology choices alongside those of CL1a, highlighting what changed and what remained.

Table 4.2: CL2a longitudinal layout (half-lengths from IP).

Subsystem	$ z _{\max}$ (mm)	Notes
Vertex/inner Si	~ 150 – 200	per layer
DC active volume	2000	Wire length
DC stay system	2500 – 2800	Drives barrel length
ECAL barrel	~ 2500	Matches DC envelope
HCAL barrel	~ 2800	Outside stays
Muon barrel	~ 3200	Outermost
Luminometer	~ 2500	In MDI region

Table 4.3: Technology comparison between CL1a (initial) and CL2a (revised). Changes are indicated in bold.

Subsystem	CL1a	CL2a
Beam pipe	Be, thinned	Be, thinned (unchanged)
Vertex + inner Si	Separate vertex + inner Si	Unified MAPS, 6 layers
Main tracker	Drift chamber (He-based)	Drift chamber (unchanged)
Outer wrapper	Strips + LGAD (two layers)	Single AC-LGAD layer
ECAL	Noble liquid (LAr)	PbWO₄ crystal, 2 segments, dSiPM (counting mode)
Solenoid	2 T, outside HCAL	1.5–3 T variable, inside HCAL
HCAL	Scint.-steel tiles	Scint.-steel tiles (as flux return)
Muon	μ -RWELL	Scintillator bars, WLS fiber + SiPM
Luminometer	Si-W calorimeter	Si-W calorimeter (unchanged)

4.3 CL2a: Performance Targets

Table 4.4 summarizes the expected performance of the CL2a concept for key physics observables.

Table 4.4: CL2a expected performance for key observables. Values marked with * are estimates based on scaling arguments rather than full simulation.

Observable	Target	Driving subsystem
Impact parameter σ_{d_0}	$\sim 3 \mu\text{m} \oplus$ $\sim 10 \mu\text{m}/(p \sin^{3/2} \theta)$	Vertex detector + beam pipe
Momentum resolution	$\sigma(p_T)/p_T^2 \lesssim$ $2 \times 10^{-5} \text{ GeV}^{-1}$	Tracker + outer wrapper + B
EM energy resolution	$\sim 3\%/\sqrt{E}$ $\oplus \sim 0.3\%$	Crystal ECAL
Jet energy* (PFA)	$\sim 3.5\text{--}4.5\%$ at 45 GeV $\sim 5\text{--}6\%$ at 100 GeV	Tracker + ECAL + HCAL + B field
π/K separation	Up to ~ 3 GeV (TOF, at 3σ level) + higher (dE/dx)	Outer wrapper + main tracker
Muon ID efficiency	$>95\%$ for $p > 3$ GeV	Absorber depth + muon stations
Luminosity	10^{-4} (absolute) 10^{-5} (relative)	Luminometer + scan strategy

The jet energy resolution numbers are estimated from the decomposition of Equation 3.11 with the crystal ECAL and 2–3 T variable field, and carry significant uncertainty. A proper evaluation requires full simulation of the CL2a geometry with realistic material budget, particle flow reconstruction, and the specific magnetic field configuration at each energy point. This is identified as a priority R&D activity.

4.4 Interplay Between Subsystem Choices

One of the principal findings of this study is that subsystem choices are strongly coupled — a change in one subsystem propagates through the design and influences optimal choices elsewhere. Several of these couplings emerged through the discussion:

- i) **ECAL technology influences the HCAL strategy.** The separate deep crystal ECAL measures all incoming photons before they reach the HCAL, reducing cluster multiplicity and simplifying the pattern recognition task. This reduces the performance difference between tile and dual-readout HCAL options, and makes the HCAL intrinsic resolution less critical relative to the particle flow confusion term.

- ii) **ECAL crystal choice drives readout R&D.** PbWO_4 's low light yield is simultaneously what makes SiPM readout conceivable (avoiding the catastrophic saturation that higher-yield crystals would produce) and what limits the photostatistical contribution to energy resolution. The readout technology choice (counting-mode dSiPM vs. analog SiPM) is a direct consequence of the crystal selection.
- iii) **ECAL technology influences PFA performance assessment.** The commonly cited PFA jet resolution numbers assume Si-W ECAL granularity. With a crystal ECAL, the photon energy term improves while the confusion term changes. The net effect is roughly neutral at Z-pole energies but must be properly evaluated with full simulation.
- iv) **Solenoid placement drives cost, flux return, and muon system design.** Moving the solenoid inside the HCAL reduces cost by $\sim 4\times$, enables the HCAL steel to serve as flux return (substantially reducing the dedicated return yoke mass and cost), and allows the muon absorber to be optimized for physics rather than magnetics. The cost is $\sim 0.4 \lambda_I$ of dead material, whose impact is mitigated by the particle flow framework: the coil material primarily affects the neutral hadron component ($\sim 10\text{--}15\%$ of jet energy), and the confusion term dominates jet resolution at all FCC-ee energies.
- v) **Variable magnetic field couples to all tracking and PFA performance.** The field strength affects momentum resolution, Lorentz angle in the drift chamber, particle flow confusion term, and the accelerator beam optics. The variable field strategy (1.5–3 T matched to beam energy) optimizes all these simultaneously.
- vi) **Tracker gas choice couples to material budget and vertex performance.** The drift chamber's helium-based gas ($\sim 0.03\% X_0$) preserves the ultra-low material budget achieved by the MAPS vertex detector. An argon-based TPC gas ($\sim 1.5\% X_0$) would partially negate the vertex detector's material investment, particularly for low-momentum tracks at the Z pole.
- vii) **Outer wrapper material affects ECAL performance.** Every fraction of X_0 in the outer wrapper increases the photon conversion probability before the ECAL. The single-layer AC-LGAD design ($\sim 0.4\text{--}1.0\% X_0$) was chosen partly to minimize this impact; the two-layer design of CL1a would have roughly doubled it.

These couplings argue against optimizing each subsystem independently — a practice that can lead to locally optimal but globally suboptimal designs. The integrated approach pursued in this study, where subsystem discussions explicitly considered the impact on neighboring systems, proved essential for arriving at a coherent overall concept.

4.5 CL2b: The Revised Complementary Detector

The complementary detector CL2b is updated from CL1b to reflect the insights from the subsystem examination. The guiding principle remains maximal complementarity with CL2a: different technologies for the major subsystems, providing independent systematic checks on all major physics measurements.

Table 4.5: CL2a and CL2b compared. Shared elements are listed below the dividing line. Changes from the initial CL1a/CL1b pairing are indicated in italics.

Subsystem	CL2a	CL2b
Main tracker	Drift chamber (He)	<i>TPC (Ar-based)</i>
ECAL	PbWO ₄ crystal	<i>Si-W, high-granularity PFA</i>
HCAL	Scint.-steel tiles	Dual-readout fibers
<i>Shared elements:</i>		
Beam pipe	Be, locally thinned	
Vertex/inner Si	Unified MAPS, 6 layers	
Outer wrapper	AC-LGAD, single layer	
Solenoid	<i>Variable 1.5–3 T, inside HCAL</i>	
Muon system	<i>Scintillator bars</i>	
Luminometer	Si-W calorimeter	

The key complementary choices and their motivation:

- **TPC main tracker.** The TPC provides true 3D space points, superior z resolution, and unambiguous pattern recognition — a fundamentally different tracking approach from the drift chamber. The argon-based gas enables Ramsauer-Townsend diffusion suppression for competitive spatial resolution at the cost of higher material budget ($\sim 1.5\% X_0$ vs. $\sim 0.03\% X_0$). The CEPC TPC studies and ILD-FCCee concept provide a strong foundation.

The different systematic profiles — drift chamber calibration (time-to-distance, wire positions) vs. TPC calibration (drift velocity, space charge) — give genuinely independent cross-checks on tracking performance.

- **Si-W electromagnetic calorimeter.** With 5×5 mm² pads and ~ 30 longitudinal layers, the Si-W ECAL is specifically optimized for particle flow, providing fine 3D shower imaging that the crystal ECAL cannot match. This gives the best possible particle flow performance (at the cost of substantially worse intrinsic photon energy resolution than the crystal’s $\sim 3\%/\sqrt{E}$, as expected for any sampling calorimeter), complementing CL2a’s approach of superior energy resolution with adequate pattern recognition.

The comparison of jet energy resolution between CL2a (crystal ECAL + tiles) and CL2b (Si-W ECAL + dual-readout) across the full FCC-ee energy range would be scientifically valuable data for future collider detector design.

- **Dual-readout fiber HCAL.** The fundamentally different approach to hadronic energy measurement — event-by-event f_{em} correction vs. particle flow avoidance — provides independent systematic checks on all jet energy measurements. As argued in Section 3.6.7, this is perhaps the strongest case for two-detector complementarity.

The dual-readout HCAL integrates more naturally with the Si-W ECAL in CL2b than it would with the crystal ECAL in CL2a, because the Si-W ECAL provides the fine granularity needed for particle flow of the charged component while the dual-readout HCAL provides robust standalone hadronic measurement for the neutral component.

The shared elements were updated from CL1b to reflect the conclusions of Chapter 3:

- The vertex and inner silicon are unified (same as CL2a).
- The solenoid is inside the HCAL with variable field (same as CL2a).
- The muon system uses scintillator bars (same as CL2a).

These shared elements were identified as clearly optimal regardless of the overall detector philosophy, so there is no benefit to making them different between the two detectors. Complementarity is most valuable where the technology choice genuinely affects the systematic profile of the physics measurements — the tracker, ECAL, and HCAL.

Note that CL2b with a dual-readout fiber HCAL and solenoid inside would require the fiber calorimeter to use a ferromagnetic absorber (steel) rather than the copper or brass typically used in RD52 prototypes, so that the HCAL steel can serve as flux return. This has not been studied in detail and represents an R&D item specific to CL2b. If a non-magnetic absorber proves necessary for the dual-readout concept, the solenoid placement in CL2b might need to differ from CL2a — an acceptable departure from the shared baseline if required by the physics.

4.6 Summary of Changes from Initial to Revised Concepts

Table 4.6 provides a consolidated summary of all changes between the initial concepts (CL1a/CL1b) and the revised concepts (CL2a/CL2b), with the primary reason for each change.

4.7 Unresolved Questions and R&D Priorities

Several important questions remain open. These are identified as priorities for future R&D, simulation studies, or design optimization:

- i) **Main tracker technology.** The drift chamber vs. TPC choice is the least resolved major decision. A direct simulation comparison under FCC-ee conditions — including realistic material budgets (He vs. Ar gas), pattern recognition in complex Z-pole events, the impact of gas material on vertexing at low momenta, and z -resolution effects on acceptance determination — would be highly valuable.
- ii) **Cluster counting performance.** The practical resolution of dN/dx cluster counting, accounting for delta ray contamination, diffusion, left-right folding, and electronics

Table 4.6: Summary of all changes from CL1a to CL2a, with the primary reason for each. Changes are numbered for reference.

#	Subsystem	Change	Primary reason
1	Vertex + inner Si	Separate → unified	No physical basis for separation at FCC-ee
2	Outer wrapper	Two layers → single AC-LGAD	Material budget reduction
3	ECAL	Noble liquid → PbWO ₄ crystal	Cryostat dead material eliminates noble liquid resolution advantage
4	Solenoid field	2 T fixed → 1.5–3 T variable	Match field to beam energy; accelerator coupling at Z pole
5	Solenoid placement	Outside → inside HCAL	~4× cost reduction; HCAL as flux return
6	Muon system	μ -RWELL → scintillator bars	Match technology to actual (modest) requirements

bandwidth, needs quantitative determination through detailed simulation with a realistic cluster-finding algorithm. The gas optimization (potentially favoring lower primary ionization rate or lower drift velocity than conventionally assumed) deserves systematic study.

- iii) **SiPM readout for crystal ECAL.** The preferred counting-mode dSiPM approach requires development of a device matched to PbWO_4 scintillation properties (cell pitch, recharge time, counter depth, integration window) and test beam validation across the FCC-ee energy range. The analog SiPM fallback, with saturation curve correction, also requires test beam characterization to establish the achievable energy resolution.
- iv) **AC-LGAD multi-hit performance.** The outer wrapper’s ability to serve position, z , and timing functions with a single AC-LGAD layer depends on the multi-hit disentangling performance, which needs systematic beam test characterization under realistic conditions.
- v) **Crystal ECAL particle flow performance.** Full simulation of jet energy resolution with the CL2a geometry (crystal ECAL, variable magnetic field, scintillator-steel HCAL) is needed to validate or correct the estimates from scaling arguments used in this report.
- vi) **Solenoid coil thickness.** Achieving $\lesssim 150$ mm coil thickness at 3 T design field requires detailed engineering study, potentially including high-temperature superconductor (HTS) options.
- vii) **Dual-readout HCAL engineering for CL2b.** The dual-readout fiber concept has been demonstrated with copper/brass absorber. For CL2b (with the solenoid inside), steel absorber is required for flux return. While there is no fundamental physics obstacle — the dual-readout correction applies regardless of absorber material — the performance with steel has not been validated, and fiber routing at full 4π scale remains an unsolved engineering challenge regardless of absorber choice.
- viii) **Luminometer stability.** Demonstration of sub- μm position stability in a realistic MDI thermal and vibrational environment, using low-CTE materials and hardware position monitoring.
- ix) **Air cooling of MAPS vertex detector.** Validation of air cooling for the ultra-thin curved MAPS shells at representative power density, with measurement of vibration and thermal uniformity.
- x) **Sensor inside beam pipe.** Feasibility R&D for the upgrade option: UHV compatibility of thinned MAPS, beam background simulation, beam impedance studies.

Chapter 5

Reflections on Human-AI Collaboration

This chapter reflects on the process of using human-AI dialogue to explore detector design. It is jointly authored: the AI drafted the assessment of its own contributions and limitations, while observations about the human role draw on the physicist's perspective as communicated during the dialogue. Both contributors reviewed the final text.

5.1 What the AI Brought to the Discussion

The AI assistant contributed several capabilities that proved useful for the detector design exploration:

5.1.1 Rapid Survey of Technology Options

For each subsystem, the AI could quickly lay out the available technology options, their demonstrated performance parameters, and their relative advantages and disadvantages. This provided a starting framework for discussion that would otherwise require extensive literature review. Examples include the comparison of noble liquid vs. crystal vs. Si-W ECAL options (Section 3.4), the LGAD variant comparison for the outer wrapper (Section 3.3.2), and the drift chamber vs. TPC assessment (Section 3.2.6).

While these surveys are not a substitute for expert knowledge — the AI's information has a training cutoff and may miss the most recent developments — they provide a useful starting point that can be corrected and refined through dialogue.

5.1.2 Quantitative Estimates on Demand

Throughout the discussion, the AI provided back-of-envelope calculations for quantities such as:

- Wire sag in the drift chamber (Section 3.2.1).
- Spoke material budget and azimuthal filling fraction (Section 3.2.1).
- Primary ionization statistics and cluster counting resolution (Section 3.2.2).
- Cryostat material budget and its impact on effective energy resolution (Section 3.4.1).

- SiPM photoelectron counts and saturation levels (Section 3.4.3).
- Luminometer position requirements from the Bhabha angular sensitivity (Section 3.8.2).
- Solenoid cost scaling and flux return calculations (Section 3.5).

These estimates, while approximate, served to make the discussion quantitative rather than purely qualitative. They enabled rapid assessment of whether a proposed effect was negligible, important, or dominant — a critical capability for design trade-off discussions. Several estimates were corrected through the dialogue (e.g., the factor-of-two from left-right folding in cluster counting, Section 3.2.2), illustrating both the value and the limitations of rapid analytical estimates.

5.1.3 Systematic Comparison Frameworks

The AI organized comparisons into structured tables and systematic assessments, making it easier to see the trade-offs clearly. The technology comparison tables throughout Chapter 3 (e.g., Tables 3.4, 3.10, 3.15, 3.16) helped organize the discussion and identify the decisive factors for each choice.

5.1.4 Willingness to Revise Positions

When presented with compelling arguments, the AI revised its positions — sometimes substantially. The ECAL technology change (noble liquid to crystal), the solenoid placement change (outside to inside HCAL), and the muon system technology change (μ -RWELL to scintillator bars) all involved the AI acknowledging that its initial reasoning was flawed or incomplete and adopting the alternative.

This willingness to revise is essential for productive collaboration. An AI that defended its initial positions regardless of contrary evidence would be far less useful as a design exploration partner.

5.1.5 Documentation and Synthesis

The AI’s ability to maintain context over a long conversation had both technical and practical benefits. During the discussion, it enabled cross-referencing between subsystem decisions — for example, recognizing that the solenoid placement inside the HCAL has consequences for the muon system absorber design, or that the crystal ECAL choice affects the HCAL’s pattern recognition demands. This contributed directly to the system-level integration discussed in Section 4.4.

As a practical matter, the AI’s ability to produce structured written output from the dialogue — this report — is a significant contribution. The synthesis of Chapter 4 draws together conclusions from dozens of individual technical discussions into a coherent integrated concept, a task that benefits from the AI’s ability to organize large amounts of discussed material.¹

¹In practice, the conversation eventually exceeded the platform’s context limits and became inaccessible, necessitating a separate editing session. The context maintenance capability is real and valuable but bounded by platform constraints.

5.2 What Required Human Guidance

The physicist’s contributions were qualitatively different from the AI’s and proved essential for arriving at sound conclusions. Several categories of human contribution are identifiable:

5.2.1 Practical Experience and Engineering Judgment

The physicist brought knowledge that is not well-represented in published literature — the kind of understanding that comes from having built, operated, and debugged real detector systems. Examples include:

- The observation that amplitude-based discrimination of primary clusters from delta ray secondaries is undermined by avalanche fluctuations and space charge effects (Section 3.2.2) — effects that are known to experts but rarely discussed in papers promoting cluster counting.
- The recognition that μ -RWELL’s impressive specifications are entirely irrelevant for FCC-ee’s benign muon system environment (Section 3.7).
- The identification of temperature stability as a potentially limiting factor for the luminometer (Section 3.8.3).
- The practical assessment of digital SiPM power requirements, informed by consultation with subject matter experts outside this collaboration, distinguishing between counting-only mode (negligible power) and timing mode (uncertain, with experts unable to commit to estimates without specific circuit design) (Section 3.4.3).

5.2.2 Asking the Right Question

Several of the most consequential shifts in the design were triggered not by the AI’s analysis but by a single well-chosen question from the physicist:

- “Why did you separate the vertex detector and inner silicon tracker?” — leading to the unified MAPS subsystem (Section 3.1.3).
- “How thick is the cryostat?” — leading to the abandonment of noble liquid ECAL in favor of crystals (Section 3.4.1).
- “Why not liquid krypton instead of argon?” — exposing an unjustified inherited assumption (Section 3.4).
- “The solenoid cost scales as $(R_{\text{out}}/R_{\text{in}})^3$ — is it worth it?” — triggering the solenoid placement change (Section 3.5).
- “Can the HCAL serve as flux return?” — strengthening the case for inside placement (Section 3.6.6).
- “The crystal ECAL filters out the EM component — doesn’t that simplify the HCAL’s job?” — reframing the HCAL technology comparison (Section 3.6.7).

- “How does the luminometer monitor its own acceptance using the same events it measures?” — exposing a logical circularity (Section 3.8.4).

In each case, the question itself contained the key physical insight. The AI’s role was to work through the implications, but the direction came from the human.

5.2.3 Recognizing Inappropriate Technology Choices

A recurring pattern was the physicist identifying cases where the AI selected technology based on impressiveness rather than suitability:

- μ -RWELL for the muon system: excellent technology, wrong application.
- The tendency to favor the most advanced LGAD variant without fully accounting for maturity and practical complications.
- The initial preference for noble liquid ECAL based on its prominent role in the ATLAS detector, without critically examining whether the same arguments apply at FCC-ee.

This reflects a systematic tendency of the AI: when trained on literature that emphasizes novel and high-performing technologies, the AI naturally gravitates toward those technologies even when simpler, more mature alternatives are better matched to the actual requirements. The human’s role in correcting this tendency was essential.

5.2.4 System-Level Thinking

The physicist consistently thought about how choices in one subsystem affect others — the kind of system-level reasoning that experienced detector designers develop over careers:

- The separate deep ECAL simplifying the HCAL’s pattern recognition task.
- The solenoid placement driving flux return, cost, and muon system design simultaneously.
- The outer wrapper material affecting ECAL performance.
- The tracker gas choice affecting vertex detector performance at low momenta.

While the AI could follow and extend these connections once pointed out, in this study the initial identification of the coupling came from the physicist rather than the AI. Whether this reflects a fundamental limitation of current AI systems or a consequence of the challenge-and-response mode adopted here is not clear from a single study.

5.3 Observations on AI Reasoning Patterns

This section presents the physicist’s observations on patterns in AI reasoning that emerged during the collaboration.

5.3.1 Knowledge Without Connections

A striking pattern emerged early in the discussion. When examining the TPC option for the main tracker, the physicist asked the AI to explain the low diffusion achievable in argon-based TPCs. The AI identified magnetic field suppression of transverse diffusion but did not mention the Ramsauer-Townsend effect — the minimum in the electron-argon scattering cross-section near 0.5 eV that enables “cool” electron transport, which is a primary motivation for argon-based TPC gases.

When the physicist raised the Ramsauer-Townsend effect explicitly, the AI immediately responded with a correct and detailed explanation of the mechanism and its implications for TPC spatial resolution. The knowledge was present but the connection to TPC diffusion was not made until prompted.

This pattern — possessing correct individual facts without making the cross-domain connections that experienced physicists find intuitive — recurred throughout the collaboration. It suggests that while AI has broad factual coverage, the associative links between concepts that constitute physical intuition are weaker or latent, requiring external activation.

5.3.2 Exploration Bounded by the Questioner

The challenge-and-response mode that proved productive for this study also creates a systematic bias: the design space explored is limited to what the physicist thought to ask about. Issues the physicist did not raise went unexamined.

This is a methodological limitation rather than purely an AI limitation. However, it differs from what one might expect with a second human expert, who would bring different experience and different blind spots, and might independently raise concerns the first physicist had not considered. The AI, operating primarily in response mode, tends to share the questioner’s blind spots rather than compensating for them. When the physicist did not challenge an aspect of the design, the AI rarely volunteered concerns unprompted.

A more proactive AI — one that systematically questioned its own proposals in the way the physicist questioned them — would partially address this limitation. Whether current or near-future AI systems can be configured to operate in this more self-critical mode is an open question.

5.3.3 Tendency Toward Deference

When the physicist challenged AI positions on technical matters, the AI rarely maintained its original stance. While this produced efficient convergence, it may not always produce the best outcome. Many design questions do not have clear right or wrong answers — they involve trade-offs where reasonable people can disagree. In such cases, productive dialogue benefits from both parties articulating and defending their positions, forcing each to sharpen their reasoning. An experienced human collaborator would sometimes push back — “I hear your concern, but I still think this approach is better because...” — even when the question is not fully resolvable. This resistance, largely absent from the AI’s behavior in this study, would strengthen the final product regardless of which position ultimately prevails.

5.3.4 Recency and Visibility Bias

The AI appeared to weight technologies more heavily when they are frequently discussed in recent literature, independent of their actual suitability. The IDEA-style drift chamber, extensively discussed in the FCC-ee context, was presented as the starting point for the main tracker; conventional drift chamber designs with decades of successful operation received less initial attention. Similarly, μ -RWELL was presented as the muon system technology, possibly influenced by its prominence in recent CMS upgrade literature, despite being dramatically overqualified for FCC-ee’s benign environment. In both cases, less recently published but equally or more suitable alternatives required the physicist’s intervention to surface.

This bias likely reflects the structure of the training data: recent papers and conference talks dominate, and technologies that generate active publication streams receive disproportionate weight in the AI’s “prior.” Technologies that are mature, well-understood, and no longer subjects of active R&D publication may be underweighted despite being excellent solutions.

5.4 Limitations of the Approach

Several important limitations should be acknowledged:

5.4.1 Knowledge Cutoff

The AI’s training data has a cutoff date, and it does not have access to the most recent results from ongoing R&D programs, conference presentations, or preprints. During the discussion, the physicist mentioned recent CEPC workshop results that the AI could not access or verify. For a field that evolves rapidly, this is a significant limitation. The AI was transparent about this limitation when it arose, which is the appropriate response — fabricating knowledge of recent results would be far worse than acknowledging ignorance.

It should be noted that this limitation is partly a consequence of the interaction mode used in this study. Tool-augmented configurations, in which the AI can search the web or query databases during the conversation, would mitigate the knowledge cutoff problem by allowing the AI to access current information on demand. Such capabilities are available in some AI platforms and are developing rapidly. A future study of this kind would likely benefit from such tools, reducing the burden on the human contributor to supply current information and enabling more thorough literature coverage.

5.4.2 Approximate Quantitative Estimates

The calculations throughout this report are analytical estimates and scaling arguments, not results of detailed Monte Carlo simulation or finite element analysis. They are useful for establishing orders of magnitude and identifying dominant effects, but they cannot substitute for proper simulation. Several conclusions — particularly the jet energy resolution estimates with the crystal ECAL and the cluster counting performance assessment — require validation through full simulation before being used to guide actual detector construction decisions.

5.4.3 Technology Enthusiasm Bias

As noted in Section 5.2, and related to the recency bias discussed in Section 5.3, the AI showed a systematic tendency toward selecting the most technically impressive available technology. This likely reflects the training data: papers and conference talks naturally emphasize novel, high-performing technologies, creating a bias in the AI’s “prior” toward such technologies. The correction — matching technology to requirements rather than selecting the most advanced option — required human intervention in several instances.

It should be noted that this is not a uniquely AI limitation. Human physicists are susceptible to analogous biases: attraction to “shiny new things” on one hand, or over-reliance on familiar tools on the other. The difference is in the mechanism — the AI’s bias is shaped by literature frequency, while a human’s may be shaped by personal experience, institutional culture, or involvement in specific R&D programs — but the resulting design errors can be similar.

5.4.4 Limited Access to Unpublished Knowledge

Much of the practical knowledge that experienced detector physicists possess is never published: lessons learned from commissioning, failure modes discovered in operation, calibration difficulties, and engineering compromises that proved consequential. The AI has access only to what appears in the published literature (and whatever fraction of informal knowledge appears in talks and proceedings). This creates a systematic gap that cannot be closed by better training data alone — some knowledge exists only in the experience of practitioners.

Again, this limitation is not unique to AI. Newcomers to the field face a similar challenge: armed with published scaling laws and performance projections, they may push a design argument to its logical conclusion without recognizing that at some point a different consideration — mechanical, thermal, operational — supersedes the original scaling. The knowledge of where these boundaries lie is precisely what distinguishes experienced practitioners, and it is acquired through years of hands-on work rather than literature study. The AI, in this sense, resembles an unusually well-read but inexperienced newcomer.

5.4.5 No Independent Validation

The AI cannot independently verify its own reasoning or catch its own errors in the way that a second human expert might. The examples of the physicist correcting the AI’s mistakes — the factor-of-two in cluster counting, the circular logic in luminometer monitoring, the technology mismatches — suggest that unchecked AI analysis would contain significant errors. The value of the AI in this study was realized only in combination with expert human review.

5.5 Assessment

The human-AI collaboration proved productive for detector design exploration, with each contributor bringing distinct and complementary capabilities:

- The AI provided breadth: rapid survey of options, quantitative estimates, systematic organization, and the ability to follow chains of reasoning across many technical domains.
- The human provided depth: practical experience, physical intuition, system-level thinking, and the critical judgment to recognize when the AI’s reasoning was flawed or its technology choice was inappropriate.

The collaboration was most productive when operating in a challenge-and-response mode: the AI presented an analysis, the human identified weaknesses or asked penetrating questions, and the AI revised in response. This iterative process converged toward conclusions that neither contributor would likely have reached independently — the AI would not have questioned its own initial assumptions, and the human would have spent considerably more time assembling the quantitative framework for each comparison.

The subsequent editing of this report — itself a human-AI collaboration — revealed additional issues not caught during the original dialogue: inconsistent numbers, unsupported quantitative claims, and framing that did not survive closer scrutiny. This reinforces the point that AI-generated analysis benefits from multiple rounds of review, not just real-time correction during the conversation.

The approach has clear limitations: it cannot replace detailed simulation, engineering design, or the collective expertise of a large collaboration. But as a tool for structured exploration of design space, rapid evaluation of trade-offs, and documentation of the reasoning behind design choices, it has demonstrable value.

Whether the specific detector concepts developed here (CL2a and CL2b) prove to be close to the eventual FCC-ee detector design is less important than whether the *process* of systematic examination, challenge, and revision leads to well-reasoned and well-documented design choices. On that criterion, we believe this exploration has been a useful exercise.

Chapter 6

Summary

This report has presented an exploration of detector design for the FCC-ee e^+e^- collider, conducted through an extended dialogue between a physicist and an AI assistant. Starting from initial detector concepts (CL1a and CL1b), each subsystem was examined in detail, leading to revised concepts (CL2a and CL2b) that differ from the starting point in several significant ways.

The principal conclusions are:

- i) **Vertex and inner silicon tracker:** A unified MAPS subsystem in 65 nm CMOS, using curved self-supporting shells with air cooling, extending continuously from the beam pipe ($R \approx 12$ mm) to the main tracker entrance ($R \approx 300$ mm). Total material budget $<0.2\% X_0$ for six layers. The separation between “vertex detector” and “inner tracker” found in LHC-era designs has no physical basis at FCC-ee.
- ii) **Main tracker:** A drift chamber with He-based gas is retained for CL2a, primarily for its ultra-low material budget. Cluster counting (dN/dx) performance is likely more modest than projected, with practical effects (delta ray contamination, diffusion, electronics bandwidth) degrading the resolution significantly from the theoretical $1/\sqrt{N}$ floor. A TPC is recommended for the complementary detector CL2b.
- iii) **Electromagnetic calorimeter:** PbWO_4 crystals replace the initial noble liquid choice. The decisive factor is the cryostat dead material ($\sim 10\text{--}15\% X_0$), which degrades the noble liquid calorimeter performance through photon conversions, non-Gaussian tails, and constant term contributions, while crystals achieve $\sim 3\%/\sqrt{E}$ with negligible dead material. The absence of radiation damage at FCC-ee and the abundant clean calibration samples across all FCC-ee running points remove the historical weaknesses of crystal calorimetry. Dual-readout (Čerenkov filtering) in the ECAL was considered but not adopted, as it provides no benefit for electromagnetic showers while degrading the scintillation light collection.
- iv) **Solenoid:** Variable field (1.5–3 T, matched to beam energy) with inside-HCAL placement. The variable field naturally aligns physics needs with accelerator constraints. The inside placement reduces cost by $\sim 4\times$ and enables the HCAL steel to serve as magnetic flux return.

- v) **Hadronic calorimeter:** Scintillator-steel tiles for CL2a, with dual-readout fibers strongly recommended for CL2b. The separate deep ECAL simplifies the HCAL’s pattern recognition task, and the particle flow confusion term dominates jet resolution over the HCAL intrinsic resolution. The HCAL technology choice is identified as the strongest case for two-detector complementarity.
- vi) **Muon system:** Scintillator bars with WLS fiber and dual-end SiPM readout replace μ -RWELL. This matches the technology to the actual (modest) requirements of muon identification at FCC-ee, with decisive advantages in operational simplicity, reliability, and cost.
- vii) **Luminosity monitor:** Si-W calorimeter (unchanged), with the understanding that the dominant challenges are metrological (sub- μm position knowledge and stability) and operational (interleaved energy scans for 10^{-5} relative precision) rather than detector-physical.

Several cross-cutting themes emerged from the study:

- **Practical considerations matter.** The cryostat dead material, the solenoid cost scaling, the SiPM dynamic range challenge at FCC-ee energies, and the operational complexity of gaseous muon detectors all proved decisive for technology choices. Abstract performance comparisons that neglect these practicalities can lead to suboptimal designs.
- **Subsystem choices are coupled.** The ECAL technology choice influences the HCAL strategy; the solenoid placement affects cost, flux return, and the muon system; the tracker gas choice affects vertex performance. Optimizing subsystems independently can yield a globally suboptimal detector.
- **FCC-ee’s benign environment is an opportunity.** The absence of radiation damage enables technologies (crystals, MAPS at $20\ \mu\text{m}$ thickness, air cooling, scintillator-based muon system) that are impractical at hadron colliders. Designs inherited from LHC-era thinking do not necessarily transfer to FCC-ee.
- **The magnetic field is a key variable.** The variable field strategy (adapting field strength to beam energy) optimizes PFA performance, momentum resolution, and accelerator compatibility simultaneously. The field strength is a significant driver of jet energy resolution through its effect on the confusion term.
- **Two-detector complementarity is valuable.** The most difficult technology choices (drift chamber vs. TPC, crystal vs. Si-W ECAL, tiles vs. dual-readout HCAL) may not have clear winners — they involve genuine trade-offs between different performance characteristics. Having both approaches deployed simultaneously provides independent systematic checks, complementary performance, and risk mitigation.

The human-AI collaboration proved productive for this exploration. The AI contributed rapid technology surveys, quantitative estimates, and systematic organization. The human

contributed practical experience, system-level thinking, and the critical questions that redirected the analysis at key points. The most consequential design changes were triggered by human questions rather than AI analysis, but the AI's ability to rapidly work through the implications of each question made the iterative exploration efficient.

The detector concepts presented here — CL2a and CL2b — are not proposed as final designs. They are the output of a structured design exploration that has identified the key trade-offs, quantified the dominant effects, and documented the reasoning behind each choice. Several conclusions require validation through detailed simulation, and a number of R&D items have been identified. The value of this exercise lies in the systematic process of examination and revision, which we hope contributes usefully to the ongoing discussion within the FCC-ee detector community.

Declaration of Generative AI in the Research Process

This work was developed through an extended, structured dialogue between the author and Claude (Anthropic, `claude-opus-4`, accessed via the Anthropic web interface), a large language model AI assistant. The nature and extent of the AI’s contribution goes substantially beyond manuscript preparation and is integral to the research content:

- i) **Conceptual development.** The AI generated the initial detector concepts (CL1a and CL1b), including the rationale for each subsystem technology choice and the criteria for integrated detector design. These served as the starting point for the collaborative exploration.
- ii) **Technical analysis.** The AI performed quantitative estimates throughout the study, including material budget calculations, force balance analyses, ionization statistics, energy resolution projections, cost scaling arguments, and magnetic flux calculations. These estimates are analytical approximations, not results of dedicated simulation.
- iii) **Iterative design evolution.** Through iterative dialogue, the author posed questions and challenges based on practical experience and physics insight. The AI revised its analyses and design choices in response, leading to the substantially revised concepts (CL2a and CL2b). The key questions and insights that drove the major design changes originated with the human author, as documented in Chapter 5.
- iv) **Manuscript drafting.** The AI drafted the majority of the manuscript text, which the author reviewed, edited, and in some cases substantially revised.
- v) **Literature survey.** The AI provided surveys of available technologies and their published performance parameters. These surveys reflect the AI’s training data, which has a knowledge cutoff, and may not include the most recent results. The author verified key references and added references known to be missing.

The AI’s contributions were subject to the following limitations, discussed in detail in Chapter 5:

- Quantitative estimates are approximate, based on analytical scaling arguments rather than detailed simulation.
- The AI exhibited a systematic tendency toward selecting technically impressive technologies over simpler alternatives better matched to the actual requirements; this was corrected through human review.

- The AI's knowledge has a training cutoff and does not include the most recent conference results or unpublished developments.
- Several errors in the AI's reasoning were identified and corrected by the author during the dialogue (e.g., a factor-of-two error in cluster counting time-domain density, circular logic in luminometer acceptance monitoring).

All AI-assisted analysis and conclusions were critically reviewed by the author. The author takes full responsibility for the scientific content, conclusions, and any remaining errors in this publication.

Bibliography

- [1] FCC Collaboration. FCC-ee: The Lepton Collider: Future Circular Collider Conceptual Design Report Volume 2. *Eur. Phys. J. Spec. Top.*, 228:261–623, 2019. doi: 10.1140/epjst/e2019-900045-4.
- [2] G. Bernardi et al. The Future Circular Collider: a Summary for the US 2021 Snowmass Process. Technical report, 2022. arXiv:2203.06520 [hep-ex].
- [3] I. Agapov et al. Future Circular Lepton Collider FCC-ee: Overview and Status. *Eur. Phys. J. Spec. Top.*, 228:261, 2019. See also updates in subsequent FCC Week proceedings.
- [4] FCC PED Group. FCC-ee Detector Concepts: Expressions of Interest, 2025. Presentations at FCC Physics, Experiments and Detectors meetings, <https://indico.cern.ch/event/1439855/>.
- [5] The IDEA Study Group. The IDEA Detector Concept for FCC-ee, 2025. arXiv:2502.21223 [physics.ins-det].
- [6] N. Alipour Tehrani et al. CLICdet and CLD — Detector concepts for FCC-ee, 2019. Described in the FCC CDR and adapted for FCC-ee conditions.
- [7] ALLEGRO Collaboration. ALLEGRO: A Lepton coLlidEr detector with Granular Read-Out, 2024. Presented at FCC Week and ECFA detector workshops.
- [8] ILD-FCCee Group. ILD adapted for FCC-ee, 2025. Expression of Interest submitted to FCC PED.
- [9] T. Abe et al. The International Large Detector: Letter of Intent. Technical report, 2010. arXiv:1006.3396 [hep-ex].
- [10] CEPC Study Group. CEPC Conceptual Design Report: Volume II — Physics & Detector. Technical report, 2018. arXiv:1811.10545 [hep-ex].
- [11] CEPC Study Group. CEPC Technical Design Report — Reference Detector. Technical report, 2025. arXiv:2510.05260 [hep-ex].
- [12] Y. Wang et al. TPC studies for CEPC, 2024. Presented at CEPC Workshop and MPGD conferences. See also contributions to the LCTPC collaboration.
- [13] ALICE Collaboration. Letter of Intent for ALICE ITS3: A truly cylindrical inner tracker based on bent wafer-scale ultra-thin silicon sensors. Technical report, 2024. CERN-LHCC-2024-003.
- [14] Mogens Dam. Detector requirements, design, and technologies for the FCC-ee Higgs, electroweak, and top factory. *Nucl. Instrum. Meth. A*, 1080:170648, 2025. doi: 10.1016/j.nima.2025.170648.
- [15] G. F. Tassielli. Progress on the Drift Chamber R&D for the IDEA detector concept at FCC-ee, 2025. Presented at FTFCF Workshop, November 2025, <https://indico.pnp>.

- ustc.edu.cn/event/4580/.
- [16] The IDEA Study Group. The IDEA Detector Concept for FCC-ee, 2025. arXiv:2502.21223 [physics.ins-det].
 - [17] W. Elmetenawee et al. Advancing particle identification in helium-based drift chambers: A cluster counting technique study through beam tests. In *Proceedings of Science (PoS)*, page 1067, 2024. doi: 10.22323/1.476.1067.
 - [18] ALICE Collaboration. The ALICE TPC upgrade. *Nucl. Instrum. Meth. A*, 1058:168790, 2024. doi: 10.1016/j.nima.2023.168790.
 - [19] Janis Noah Jäger. Drift-field distortions in the ALICE TPC in LHC Run 3, 2026. Presented at the 7th DRD1 Collaboration Meeting, CERN, 23 February 2026, <https://indico.cern.ch/event/1632132/>.
 - [20] S. Ayyoub et al. A new generation of LGAD sensors with trench isolation. *Nucl. Instrum. Meth. A*, 1056:168492, 2023. doi: 10.1016/j.nima.2023.168492.
 - [21] Christian W. Fabjan and Fabiola Gianotti. Calorimetry for particle physics. *Reviews of Modern Physics*, 75(4):1243–1286, 2003. doi: 10.1103/RevModPhys.75.1243.
 - [22] N. Akchurin et al. Hadron and jet detection with a dual-readout calorimeter. *Nuclear Instruments and Methods in Physics Research Section A*, 537(3):537–561, 2005. doi: 10.1016/j.nima.2004.07.285.
 - [23] N. Akchurin et al. The electromagnetic performance of the RD52 fiber calorimeter. *Nuclear Instruments and Methods in Physics Research Section A*, 735:130–144, 2014. doi: 10.1016/j.nima.2013.09.033.
 - [24] F. Sefkow et al. Experimental tests of particle flow calorimetry. *Rev. Mod. Phys.*, 88:015003, 2016. doi: 10.1103/RevModPhys.88.015003.
 - [25] S. Lee et al. Hadron detection with a dual-readout fiber calorimeter. *Nucl. Instrum. Meth. A*, 866:76–90, 2017. doi: 10.1016/j.nima.2017.05.025.
 - [26] Belle II Collaboration. Belle II Technical Design Report. Technical report, 2010. arXiv:1011.0352 [physics.ins-det]. Muon system upgrade to scintillator bars described in subsequent Belle II upgrade documents.
 - [27] A. Artikov et al. The Mu2e Cosmic Ray Veto detector. *Nucl. Instrum. Meth. A*, 1042:167370, 2022. doi: 10.1016/j.nima.2022.167370.